



**POLITECNICO**  
MILANO 1863

SCUOLA DI INGEGNERIA INDUSTRIALE  
E DELL'INFORMAZIONE

# Advancing Tumor Perfusion Analysis: A Homogenization Approach for Microcirculatory Blood Flow Simulation

TESI DI LAUREA MAGISTRALE IN  
MATHEMATICAL ENGINEERING - INGEGNERIA MATEMATICA

Author: **Francesca Schweiger**

Student ID: 992127

Advisor: Prof. Paolo Zunino

Co-advisors: Dr. Nunzio Dimola, Dr. Piermario Vitullo

Academic Year: 2022-23



# Abstract

This thesis explores innovative methodologies for simulating blood flow within microvascular networks. This work aims to improve the ability to accurately model phenomena such as drug delivery within tumors or oxygen diffusion through microcirculation that can significantly impact the development of improved treatments for various diseases. An important challenge in this area is the intricate interaction between the microvasculature, a complex network, and its surrounding tissue, made more difficult by the computational demands of detailed 3D vascular meshing. To address this, the thesis focuses on the use of homogenization techniques to simplify the modeling process. In particular, in this work a 3D-1D coupled problem, where tissue is represented as a 3D porous medium and the vascular network as a 1D graph, is approximated with a homogenized 3D-3D coupled problem. This approach models both the tissue and the now homogenized vascular network as 3D porous mediums. We introduce both a primal-pressure and a mixed-pressure-velocity formulation, significantly reducing computational complexity. A pivotal aspect of the study is the strategic division of the domain into Representative Elementary Volumes (REVs) and the calculation of upscaled parameters that accurately reflect the microvascular network's characteristics at a macroscopic level. The algorithm for the segmentation of the domain into REVs and the subsequent calculation of these parameters are central to the thesis development. An efficient solver is then introduced for reconstructing the blood flow's pressure and velocity across various geometries. Initial tests on a synthetic vascular structure within a cubic tissue domain demonstrated the solver's capability to produce viable results in terms of parameter estimation and the reconstruction of blood flow characteristics. Further examination using a more complex vascular network from cancerous tissue in a mouse brain showcased the potential for future enhancements and applications of this approach in microcirculation modeling, leveraging mathematical homogenization, REV division, numerical discretization, and mixed formulation techniques, supporting advancements in medical treatment research.

**Keywords:** microcirculation modeling, mathematical homogenization, REV division, numerical discretization, primal pressure formulation, mixed formulation



# Abstract in Lingua Italiana

Questa tesi esplora metodologie innovative per simulare il flusso sanguigno all'interno di reti microvascolari. Questo lavoro mira a migliorare la capacità di modellare con precisione fenomeni come la distribuzione dei farmaci all'interno dei tumori o la diffusione dell'ossigeno attraverso la microcircolazione, che possono influenzare significativamente lo sviluppo di trattamenti migliorati. Una sfida in questo settore è l'interazione intricata tra la microvascolatura, una rete complessa, e il tessuto circostante, resa più difficile dalla necessità di una discretizzazione vascolare 3D computazionalmente costosa. Per affrontare questo problema, la tesi si concentra sull'uso di tecniche di omogeneizzazione per semplificare il processo di modellazione. In particolare, in questo lavoro un problema accoppiato 3D-1D, dove il tessuto è rappresentato come un mezzo poroso in 3D e la rete vascolare come un grafo 1D, viene approssimato con un problema omogeneizzato accoppiato 3D-3D. Questo approccio modella sia il tessuto che la rete vascolare ora omogeneizzata come mezzi porosi in 3D. Introduciamo sia una formulazione primale-pressione che una formulazione mista-pressione-velocità, riducendo la complessità computazionale. Un aspetto fondamentale dello studio è la divisione strategica del dominio in Volumi Elementari Rappresentativi (REVs) e il calcolo di parametri ampliati che riflettano le caratteristiche della rete microvascolare a livello macroscopico. L'algoritmo per la segmentazione del dominio in REVs e il calcolo successivo di questi parametri sono centrali per lo sviluppo della tesi. Viene poi introdotto un solver efficiente per ricostruire la pressione e la velocità del flusso sanguigno in varie geometrie. I test iniziali su una struttura vascolare sintetica all'interno di un dominio tessutale cubico hanno dimostrato la capacità del solver di produrre risultati validi in termini di stima dei parametri e ricostruzione delle caratteristiche del flusso sanguigno. Un ulteriore esame utilizzando una rete vascolare più complessa da tessuto canceroso nel cervello di un topo ha mostrato il potenziale per futuri miglioramenti e applicazioni di questo approccio nella modellazione della microcircolazione, sfruttando l'omogeneizzazione matematica, la divisione in REVs, la discretizzazione numerica e le tecniche di formulazione mista, supportando gli avanzamenti nella ricerca medica.

**Parole chiave:** microcircolazione, omogeneizzazione, divisione in REV, formulazione in pressione, formulazione mista



# Contents

<b>Abstract</b>	i
<b>Abstract in Lingua Italiana</b>	iii
<b>Contents</b>	v
<b>1 Introduction</b>	1
<b>2 Mathematical Background</b>	5
2.1 Problem Setting . . . . .	5
2.2 A 3D-1D Model for Microcirculation . . . . .	6
2.3 Theoretical Foundations of the Model . . . . .	7
2.4 A Review of Mathematical Homogenization . . . . .	8
<b>3 Homogenization of the 3D-1D Microcirculation Model</b>	13
3.1 Homogenized 3D-3D Model . . . . .	13
3.2 Calculation of the Effective Parameters . . . . .	15
3.2.1 Definition of the Upscaled Viscosity $\mu_{bl}^{up}$ . . . . .	15
3.2.2 Definition of the Upscaled Permeability Tensor $K_{up}$ . . . . .	16
3.2.3 Definition of the Source Term $q_t^{cap}$ . . . . .	18
3.3 Primal-Pressure Homogenized Model . . . . .	19
3.4 Mixed Homogenized Model . . . . .	19
<b>4 Numerical Discretization</b>	21
4.1 Primal Formulation of the Homogenized Model . . . . .	21
4.1.1 Variational Formulation . . . . .	21
4.1.2 FEM Discretization . . . . .	23
4.1.3 Existence and Uniqueness . . . . .	24
4.2 Mixed Formulation of the Homogenized Model . . . . .	25
4.2.1 Variational Formulation . . . . .	25

4.2.2	FEM Discretization . . . . .	28
4.2.3	Existence and Uniqueness and Error Estimates . . . . .	30
<b>5</b>	<b>Implementation</b>	<b>35</b>
5.1	Computation of the Homogenized Parameters . . . . .	35
5.1.1	REV Division Algorithm . . . . .	36
5.1.2	Upscaling Strategy . . . . .	41
5.2	Solver for the Homogenized Models . . . . .	43
5.2.1	Primal Pressure Model . . . . .	44
5.2.2	Mixed Model . . . . .	45
<b>6</b>	<b>Analysis of Perfusion in the Tumor Microvasculature</b>	<b>47</b>
6.1	Synthetic Vascular Network Analysis . . . . .	48
6.1.1	Generation of the Vascular Network . . . . .	48
6.1.2	REV Division . . . . .	50
6.1.3	Upscaled Parameters . . . . .	53
6.1.4	Primal Pressure Model . . . . .	56
6.1.5	Mixed Model . . . . .	59
6.2	Mouse Tumor Vasculature in a Cube . . . . .	60
6.2.1	Real-Case Cancer Geometry . . . . .	60
6.2.2	REV Division . . . . .	61
6.2.3	Upscaled Parameters . . . . .	63
6.2.4	Primal Pressure Model . . . . .	66
6.3	Entire Mouse Tumor Vasculature . . . . .	69
6.3.1	Real-Case Cancer Geometry: Boundary Points . . . . .	69
6.3.2	REV Division . . . . .	69
6.3.3	Upscaled Parameters . . . . .	71
6.3.4	Primal Pressure Model . . . . .	74
<b>7</b>	<b>Conclusions</b>	<b>79</b>
<b>Bibliography</b>		<b>83</b>
<b>List of Figures</b>		<b>87</b>
<b>List of Tables</b>		<b>89</b>

# 1 | Introduction

Over the past few decades, mathematical modeling of the fluid dynamics of blood in human vessels has been widely spread. In fact, having a deep understanding of the behavior of the vascular system of the body could be very helpful in understanding several diseases. Modeling blood flow in microvascular networks, addressing different aspects such as cellular-scale simulations, theoretical modeling, and numerical simulations to understand the complex dynamics of microcirculatory blood flow, has been a vivid subject of research [20, 21]. For example, many studies have focused on the analysis of blood flow in cerebral tissue [24], or on the investigation of drug delivery in tumors [5]. Furthermore, analysis of blood flow and oxygen diffusion in certain types of cancer can be extremely helpful in the search for treatments such as radiotherapy [19][26]. In general, these types of problems are characterized by a complex vascular system, mainly made up of microvasculature, which is difficult to model and analyze.

The well-known Navier-Stokes equations are a suitable and effective model used in Computational Fluid Dynamics (CFD) simulations for reconstructing the velocity and pressure of blood in medium and large vessels. Instead, in the context of microvessels, namely the collection of vessels with a diameter smaller than  $150 \mu\text{m}$  [3], and microcirculation, the analysis of blood flow requires more details to define a suitable mathematical model. In particular, at such small diameters, even the dimensions of the cells that compose the blood become significant [10]. Usually, state-of-the-art models treat tissue as a 3D porous medium, described by the Darcy equation, and simplify the capillary bed using a 1D network model. However, the interaction between microvessels and tissue at this level is very complex. The structure of the capillary bed is usually elaborate, with many vessels in a small portion of the tissue and multiple intersections between them. For these reasons, a direct CFD approach to each edge of the vascular network is not feasible and could lead to a high computational cost [19].

**State of the art.** In this context, several model reduction techniques, such as homogenization, have arisen. The multiscale homogenization of perfusion in solid tumors encapsulates a rich field of research focused on understanding and simulating the complex phenomena of blood flow within the microvascular network of tumors. This field has been advancing through the development and application of sophisticated mathematical models and computational methods designed to bridge the gap between microscale vascular structures and macroscale behavior of blood perfusion in tumor tissues. Central to this advancement is the recognition that traditional CFD models, while effective in capturing blood flow in larger vessels, fall short when applied to the microvasculature characteristic of solid tumors. The challenge of modeling tumor perfusion at the microscale lies not only in the complex architecture of the capillary network but also in the interaction between blood flow within these vessels and surrounding tumor tissue. To address these challenges, the field has moved toward the adoption of homogenization techniques, which offer a promising avenue for reducing the computational complexity of simulating blood flow in microvascular networks. Homogenization techniques, as discussed in various studies [3, 8, 13, 18, 28], treat the capillary bed as a homogenized porous medium, where the detailed structure of the microvascular network is averaged over a certain volume, known as the Representative Elementary Volume (REV). These approaches find applications across several fields, including the derivation of Darcy's law for flows in porous media, the development of porosity models, and the understanding of the long-term behavior of diffusion equations. Furthermore, the paper discusses numerical algorithms for homogenization, highlighting multiscale finite element methods (MsFEMs) [7] as a pivotal approach to solving partial differential equations in highly heterogeneous media. Moreover, homogenization simplifies the modeling process by approximating the microvascular bed with effective properties, such as permeability tensors, that capture the essence of the blood flow behavior through the network. The development and validation of these homogenized models have been a significant focus of recent research, with the aim of accurately representing the dynamics of perfusion within tumors. In [28] the authors present hybrid models that combine detailed 3D representations of larger blood vessels with homogenized descriptions of smaller capillary networks, offering a balance between computational efficiency and the need for detail in certain regions of interest. The article [8] extends the application of homogenization techniques to synthetic models of human cerebral microvascular networks, emphasizing the importance of accurately determining the permeability tensor to model perfusion in larger volumes of tissue. In [13] the authors focus on the validation and optimization of parameters within a hybrid embedded / homogenized model to simulate perfusion through solid tumors, highlighting the potential of the method in studying tumor perfusion and drug delivery efficacy. Together,

these studies underscore the current state of the art in multiscale homogenization of tumor perfusion, characterized by a continuous effort to refine mathematical models and computational methods. The ultimate goal is to achieve a deeper understanding of tumor biology and improve therapeutic strategies by accurately simulating microcirculation dynamics within solid tumors. This ongoing research not only advances our theoretical knowledge but also holds promise for practical applications in oncology, particularly in optimizing drug delivery and enhancing the effectiveness of treatments. In addition, it is important to pay attention to the study of algorithms capable of creating anatomically consistent capillary networks. To do so, several techniques have been developed to incorporate data from medical imaging to obtain realistic networks that are essential to test the mathematical models obtained. Various consistent results in this field, such as [15] and [11], have achieved the development of an algorithm that builds the cortical circulation of a whole mouse brain, starting from real input data. Additionally, the REANIMATE project [6], [27] obtained the digital vascular structure of a tumor mass grown on a mouse brain.

**Aim of the work.** The goal of this thesis is to refine and apply a homogenized approach applied to the 3D-1D coupling model to simulate and understand blood flow within microcirculatory networks. It focuses on creating and employing computational tools for deriving meaningful parameters that accurately capture the vascular network's characteristics, alongside a methodology to reconstruct blood pressure and flow across various scenarios. Special emphasis is placed on developing a REV division algorithm for effective domain segmentation, crucial for linking micro- and macro-scale phenomena within the homogenized capillary framework. This approach will be validated against three distinct geometries, including a real-world case study.

**Organization of this work.** In Chapter 2, we present an overview of the mathematical background of this thesis, presenting the state-of-the-art model used in microcirculation, also from a theoretical point of view and a review of the homogenization approach. In Chapter 3 the homogenized version of the model is reported in both primal-pressure and mixed formulations. Then, in Chapter 4, the aspects concerning the numerical discretization of the proposed models are detailed, including theoretical results regarding the feasibility of the solutions found. The details of the implementation of the code developed to simulate the problem are contained in Chapter 5, where a first part is dedicated to implementing algorithms to compute the upscaled parameters and the second to developing a solver to simulate the problem. Finally, Chapter 6 presents the results of applying this method to different test cases, from a simple and synthetic one to a real application

to a mouse brain tumor. In particular, we discuss the computed values of the upscaled parameters and the reconstruction of capillary and tissue pressure, and in some cases, the velocity, in different geometries.

# 2 | Mathematical Background

This chapter introduces a background of the mathematical models used to describe blood flow in the microvasculature surrounded by tissue. To have a realistic representation of the complex behavior of microcirculation in the surrounding tissue, a *mesoscale* approach is considered. This kind of approach has been presented from a theoretical point of view in the paper [14]. In this paper, several model reduction techniques have been applied to the general problem in order to obtain a simplified but coherent version. At first, the details concerning the framework of the problem are delineated. Then the state-of-the-art 3D-1D model is introduced, with additional details regarding the theoretical background of this formulation. Finally, a review regarding the strategy and mathematical details of the homogenization technique is reported.

## 2.1. Problem Setting

The computational domain in which our problem is defined has to represent a three-dimensional region of tissue described as a porous medium, in which there exists a relatively complex vascular network. In particular, we consider a cubic region described as follows:

$$\Omega = \{\mathbf{x} = (x, y, z) \in \mathbb{R}^3 \mid (x, y, z) \in (x_1, x_2) \times (y_1, y_2) \times (z_1, z_2)\}.$$

Concerning the vascular network, an approximation has been made. In order to reduce the computational cost, we consider a 1D representation of the network. This is justified by the fact that this kind of simplification avoids the step of creating a suitable 3D mesh of the vascular net, which is notoriously expensive [28]. In addition, the topology and main characteristics of the vascular bed are preserved, such as the bifurcations and the orientation of the capillaries in the three-dimensional domain. Therefore, the vascular system can be defined by a graph  $\Lambda$  that has as *nodes* the points that identify each bifurcation, also known as vertices, and as *edges* the straight line connecting two nodes. This set represents the connectivity of the network. In addition, each edge is assigned with a characteristic radius derived from the original 3D vascular network. This will be important in the following sections, in order to have a more precise computation of the

parameters related to the vascular net. Summarizing

$$\begin{aligned}\Lambda = (N, E, R), \text{ where } N &= \{0, \dots, N_{\max}\}, \\ E &= \{(i, j) \in \tilde{E} \subset N \times N\}, \\ R &= \{R_0, \dots, R_{E_{\max}}\},\end{aligned}$$

where  $N_{\max}$  is the number of points and  $E_{\max}$  is the number of edges in the net. In the end, our computational domain is composed of a cubic region representing the tissue and a vascular net completely embedded in it, modeled as a graph described above.

## 2.2. A 3D-1D Model for Microcirculation

In this section, we present the model that describes microcirculation in a porous medium. In this model, a first level of reduction has been applied. In fact, the vascular network has been reduced from 3D to 1D, while the tissue model is still represented as three-dimensional. The theoretical reasoning behind this simplification is reported in Section 2.3. Moreover, in order to model our problem, we consider the following assumptions:

- The non-Newtonian flow behavior of blood is modeled using an algebraic relation, to simplify the problem: this is reasonable considering that the diameter of the capillaries is comparable with the one of the blood cells, so it is feasible to consider a viscosity that varies with for each blood vessel;
- The density of blood is constant: we consider blood as incompressible;
- The influence of gravity, inertial effects, and pulsatility are neglected: these are motivated by the fact that both the Reynold and the Womersly numbers are way lower than 1.0.

Considering a general cube of tissue  $\Omega$ , with an embedded vascular network  $\Lambda$ , as described before in 2.1, we define the fully discrete 3D-1D model as follows:

$$\left\{ \begin{array}{ll} -\nabla \cdot (\rho_{\text{int}} \frac{K_t}{\mu_{\text{int}}} \nabla p^t) = L_{\text{cap}} \rho_{\text{int}} (p^V - \bar{p}^t - (\pi_p - \pi_{\text{int}})) \delta_{\Gamma_C} & \text{in } \Omega, \\ -\frac{d}{ds} (\rho_{\text{bl}} \pi R^2 \frac{K_V}{\mu_{\text{bl}}} \frac{dp^V}{ds}) = 2\pi R L_{\text{cap}} \rho_{\text{int}} (\bar{p}^t - p^V + (\pi_p - \pi_{\text{int}})) & \text{in } \Lambda, \\ \rho_{\text{int}} \frac{K_t}{\mu_{\text{int}}} \nabla p^t \cdot \mathbf{n} = \beta (p^t - p_0) & \text{on } \partial\Omega, \\ p^V = p_D^V & \text{on } \partial\Lambda. \end{array} \right. \quad \begin{array}{l} (2.1a) \\ (2.1b) \\ (2.1c) \\ (2.1d) \end{array}$$

The tissue is treated as a porous medium of domain  $\Omega$ : to reconstruct the pressure field, we used the Darcy equation (2.1a) with an isotropic scalar permeability parameter  $K_t$ . Instead, to model the 1D vascular network in the domain  $\Lambda$ , the Hagen-Poiseuille law with a mass balance equation (2.1b) is used. For both equations, the source term derives from Starling's filtration law and it is the one that couples the model. As explained in [17], the coupling between blood in vessels and tissue occurs through the membrane  $\Gamma_C$  and is proportional to the difference between hydrostatic and oncotic pressures. In particular, for the tissue, the Dirac measure is introduced on the membrane  $\Gamma_C$ , that is,  $\delta_{\Gamma_C}$ . In addition to that, the permeability of the vascular network  $K_V$  [ $\text{m}^2$ ] is defined for each segment  $\Lambda_k$  as:

$$K_V|_{\Lambda_k} = \frac{R_k^2}{8}. \quad (2.2)$$

For this model, suitable boundary conditions are defined. For the tissue, we chose Robin boundary conditions, as defined in 2.1c. This is feasible considering that some flux could exit from the tissue domain if the pressure is high. This is represented by the difference between the tissue pressure at the boundary and a reference pressure  $p_0$ , scaled by a parameter  $\beta$ . It should be noted that for pretty low values of  $\beta$ , we can recover the Neumann homogeneous condition.

Lastly, equation 2.1d defines Dirichlet boundary conditions for the vascular network. The values will be chosen correctly for the inlet and outlet facets and accordingly with the reference pressure value of the tissue.

### 2.3. Theoretical Foundations of the Model

In this section, we present some theoretical results collected in [14] with respect to micro-circulation modeling. The starting point of this work was a fully 3D second-order elliptic model coupled with interface conditions of Robin type. In this formulation, instead of a complete vascular net, it is considered a singular cylindrical vase  $\Sigma$ , embedded in a cubic domain  $\Omega$ . Therefore, we define  $\Omega_+ = \Omega \setminus \bar{\Sigma}$ . The cylinder boundary is divided into  $\Gamma$ , the lateral surface,  $\Gamma_{in}$  and  $\Gamma_{out}$ , the inlet and outlet surfaces, respectively.

$$\left\{ \begin{array}{ll} -\Delta u_+ = f & \text{in } \Omega_+, \\ -\Delta u_- = g & \text{in } \Sigma, \\ -\nabla u_+ \cdot \mathbf{n}_+ = k (u_+ - u_-) & \text{on } \Gamma, \\ -\nabla u_- \cdot \mathbf{n}_- = -k (u_+ - u_-) & \text{on } \Gamma, \\ -\nabla u_+ \cdot \mathbf{n}_+ = 0 & \text{on } \Gamma_{\text{in}} \cup \Gamma_{\text{out}}, \\ -\nabla u_- \cdot \mathbf{n}_- = 0 & \text{on } \Gamma_{\text{in}} \cup \Gamma_{\text{out}}, \\ u_+ = 0 & \text{on } \partial\Omega, \end{array} \right. \quad \begin{array}{l} (2.3a) \\ (2.3b) \\ (2.3c) \\ (2.3d) \\ (2.3e) \\ (2.3f) \\ (2.3g) \end{array}$$

where the coefficient  $k$  is uniform and has the role of a *permeability coefficient* and the interface  $\Sigma$  is considered permeable.

When dealing with the numerical approximation of this formulation, some problems may arise. In particular, the main difficulties are related to the complexity of the geometries and their interaction, especially considering the model's application in real-life scenarios. For this reason, in this work a topological model reduction technique is proposed, in order to simplify 2.3 and obtain a 3D-1D model, where the cylinder  $\Sigma$  is approximated with its centerline  $\Lambda$ . The result of this averaging operation is reported below:

$$-d_{ss}^2 U + \frac{|\partial D|}{D} k U = \frac{|\partial D|}{D} k u_+^- + \bar{g} \quad \text{on } \Gamma, \quad (2.4a)$$

where  $s$  represents the direction along the midline of the cylinder,  $U(s) = u_-(r, s, t)$ , so it is the solution in the new parametrization, and  $u_+$  and  $\bar{g}$  are the results of the averaging technique applied to the 3D variable in 2.3. Finally, we define as  $D(s)$  the cross-sectional area and as  $\partial D(s)$  its boundary. It should be noted that this approach can be extended to the case where  $\Lambda$  is a network, that is, the situation described in Section 2.1, applying 2.4. However, some attention has to be paid to the treatment of junctions, where cylinders of different radii meet, as explained in detail in [14].

## 2.4. A Review of Mathematical Homogenization

Here, we present some results on homogenization, collected from [2] and [12], with particular attention to the application to a generic diffusion problem. In the model reduction field, extensive interest is given to homogenization. This is a mathematical method used to average differential equations, with a rigorous theory that supports its validity. In fact, this approach provides both upscaling formulas and more theoretical results such as convergence theorems. At first, homogenization was developed for the periodic structure. Nevertheless, this tool has proved to be very efficient in modeling complex phenomena in

heterogeneous media and is frequently applied in many contexts. For example, the study of microvasculature in a porous medium does not highlight a strict periodicity. However, the presence of microscopic variations and heterogeneity in its structure, such as a sharp change of direction due to an intricate vascular net, can lead to localized fluctuations in pressure, similar to the variations observed in periodic media. Homogenization can help capture the effective behavior of the medium by averaging out these microscopic fluctuations.

The mathematical justification for homogenization involves techniques such as two-scale asymptotic expansions, where the solution to a problem is expressed as a series expansion in terms of a small parameter  $\epsilon$  representing the scale ratio, as explained in [1]. This method is complemented by the rigorous two-scale convergence theory and the oscillating test function method, offering a strong foundation for the validity of the homogenization theory. Furthermore, in non-periodic or random media, the concept of G-convergence (or H-convergence for non-symmetric cases) is introduced. This concept provides a framework for understanding how the properties of heterogeneous materials converge to those of an effective homogeneous medium without relying on specific geometric or statistical properties of the original media. In essence, the theory provides a rigorous foundation for approximating complex heterogeneous materials with simpler, effective properties that facilitate the analysis and simulation of multiscale phenomena.

**Mathematical Preliminaries and Main Results** Let us outline the central equations on homogenization, see [1, 12], which revolve around an examination of how complex microscopic structures within a heterogeneous medium can be effectively modeled on a macroscopic scale, employing a more simplified homogeneous representation.

We consider  $p$  as a real-valued function in a domain  $\Omega$  that describes a certain physical quantity with spatial oscillations, in our case the pressure of a fluid in a porous medium. The homogenization process introduces a whole family of functions  $p^\epsilon$ , with the spatial scale parameter  $\epsilon > 0$ . In fact, instead of considering a single heterogeneous medium with a fixed lengthscale, we introduce a sequence of similar lengthscale problems  $\epsilon$ . Then, we define the model for diffusion within a periodic medium. This is mathematically articulated as follows:

$$\begin{cases} -\nabla \cdot \left( A \left( \frac{x}{\epsilon} \right) \nabla p^\epsilon \right) = f & \text{in } \Omega, \\ p^\epsilon = p_D^\epsilon & \text{on } \partial\Omega. \end{cases} \quad (2.5a)$$

Here, the function  $A(y)$  denotes a matrix that periodically varies with respect to the variable  $y$ , encapsulating the heterogeneity of the medium at the microscale. The domain

$\Omega$  identifies the region under consideration in  $R^N$ .

After that, we exploit two-scale asymptotic expansions to represent the solution  $p_\epsilon(x)$ , namely:

$$p^\epsilon(x) = p_0\left(x, \frac{x}{\epsilon}\right) + \epsilon p_1\left(x, \frac{x}{\epsilon}\right) + \epsilon^2 p_2\left(x, \frac{x}{\epsilon}\right) + \dots, \quad (2.6)$$

highlighting the interaction between the different scales through functions  $p_0$ ,  $p_1$ ,  $p_2$ , etc., which depend on both the macroscopic variable  $x$  and the scaled microscopic variable  $x/\epsilon$ . Then the result of the upscaling procedure is the computation of the limit:

$$p = \lim_{\epsilon \rightarrow 0} p^\epsilon. \quad (2.7)$$

The next step in our exposition is the introduction of the homogenized operator, which consists in the formulation of the homogenized equation:

$$-\operatorname{div}(A^* \nabla p) = f \text{ in } \Omega, \quad (2.8)$$

where  $A^*$  identifies the effective or homogenized conductivity tensor. This tensor encapsulates the macroscopic behavior of the medium, starting from the complex microscale heterogeneities. The computation of  $A^*$  typically involves solving auxiliary problems known as cell problems, associated with the original heterogeneous medium.

Finally, the concept of G convergence (or H convergence for nonsymmetric cases) is used to understand the transition from the heterogeneous to the homogenized medium. G-convergence is defined in the context of sequences of conductivity tensors  $A_\epsilon$ , which converge to a homogenized limit  $A^*$ . Specifically, a sequence  $A_\epsilon$  G converges to  $A^*$  if, for any source term  $f \in L^2(\Omega)$ , the solutions  $p_\epsilon$  of the equation

$$-\operatorname{div}(A_\epsilon \nabla p^\epsilon) = f \text{ in } \Omega, \quad (2.9)$$

converge weakly in  $H_0^1(\Omega)$  to the solution  $p$  of the homogenized equation 2.8 associated with  $A^*$ . This convergence signifies the essence of homogenization, where detailed microscale information encoded in the sequence  $A_\epsilon$  is effectively captured and represented by the homogenized tensor  $A^*$ , thus simplifying the analysis and simulation of phenomena in heterogeneous media. We state this result in the following proposition.

**Proposition 2.1.** *The differential operator  $\nabla \cdot (A^* \nabla p(x))$  is the homogenization of the*

operator family  $\nabla \cdot (A(\frac{x}{\epsilon}) \nabla p^\epsilon(x))$ , i.e., the homogenization of problem 2.5 is given by

$$\begin{cases} -\nabla \cdot (A^* \nabla p) = f & \text{in } \Omega, \\ p = p_D & \text{on } \partial\Omega. \end{cases} \quad (2.10a)$$

Lastly, another important result is that in general the effective tensor  $A^*$  obtained is not diagonal, but is symmetric and positive definite. However, in Section 3.2, further approximation will be made to match our problem.



# 3 | Homogenization of the 3D-1D Micirculation Model

In this chapter, we present the homogenized version of the state-of-the-art 3D-1D problem for microcirculation in surrounding tissue. At first, a primal-pressure formulation is introduced. The unknowns of this model are the pressure in the homogenized capillary bed and the pressure in the tissue. In fact, we assume that our problem refers to the capillary bed with radii of the networks of the order of  $10 \mu\text{m}$ . This model was presented in [28], but the main difference is that we are not considering large vessels in our formulation. Then, the definition of the upscaled parameters that synthesize the microvasculature properties is introduced. Finally, a layer of difficulty is added as we present a mixed-pressure-velocity formulation of the homogenized problem, where the velocity of both the capillary and tissue domains is recovered by the Darcy equation. Further details about the different geometries used to test these models will be given in Chapter 6, with more specifics on each case test.

## 3.1. Homogenized 3D-3D Model

In this section, we present the homogenized version of the problem 2.1, achieved with the technique explained in 2.4. In this way, we obtain an even more simplified problem than the one presented in Section 2.2. This is justified by the fact that it is very difficult to understand and compute the behavior of a realistic capillary net with the canonical strategy; therefore, it is very common to homogenize the equation. In fact, the vascular net can be considered a 3D porous medium and described with the Darcy law. The challenge now is to define a suitable permeability tensor that can synthesize the main characteristic of the capillary net in a specific area. So the capillary model presented

### 3| Homogenization of the 3D-1D Microcirculation Model

above is modified and can be considered as follows:

$$\left\{ \begin{array}{ll} -\nabla \cdot \left( \rho_{bl} \frac{K_{up}}{\mu_{bl}^{up}} \nabla p^{cap} \right) = q_v^{cap} + q_t^{cap} & \text{in } \Omega, \\ p^{cap} = p_D^{cap} & \text{on } \Gamma. \end{array} \right. \quad \begin{array}{l} (3.1a) \\ (3.1b) \\ (3.1c) \end{array}$$

where  $\rho_{bl}$  is the density of the blood. Instead,  $\mu_{bl}^{up}$  and  $K_{up}$  are the averaged viscosity of blood and the permeability tensor, respectively, and they have to be suitably computed. In fact, they are the upscaled parameters obtained as a result of the homogenization process. Furthermore,  $p_D^{cap}$  is the Dirichlet boundary condition and  $q^{cap}$  is the source term. Regarding the last term, we make a final simplification: we neglect the interaction with the large vessels, so we can assume  $q_v^{cap} = 0$ . The equations for the tissue are the same as in the model 2.1:

$$\left\{ \begin{array}{ll} -\nabla \cdot \left( \rho_{int} \frac{K_t}{\mu_{int}} \nabla p^t \right) = -q_t^{cap} & \text{in } \Omega, \\ \rho_{int} \frac{K_t}{\mu_{int}} \nabla p^t \cdot \mathbf{n} = \beta(p^t - p_0) & \text{on } \partial\Omega. \end{array} \right. \quad \begin{array}{l} (3.2a) \\ (3.2b) \end{array}$$

where  $\rho_{int}$ ,  $K_t$  and  $\mu_{int}$  are given. Moreover, we assume isotropic permeability for the tissue and constant viscosity. Notice that for this model, we have Robin boundary conditions, and this is consistent with the original model 2.1.

In Table 3.1 is collected a detailed description of the parameters of the model.

Tissue permeability	$K_t$
Interstitial fluid viscosity	$\mu_{int}$
Plasma viscosity	$\mu_p$
Blood viscosity	$\rho_{bl}$
Interstitial fluid density	$\rho_{int}$
Plasma oncotic pressure	$\pi_p$
Interstitial oncotic pressure	$\pi_{int}$
Capillary wall hydraulic conductivity	$L_{cap}$
Capillary radius for edge k	$R_k$
Reference pressure	$p_0$
Neuman parameter	$\beta$
Dirichlet value	$p_D$

Table 3.1: Parameters of the Homogenized model

## 3.2. Calculation of the Effective Parameters

As a result of the homogenization process, we obtain a 3D-3D coupled problem. The vascular net is now considered a porous medium and can be described with the Darcy equation, similar to the tissue. Nevertheless, there is still a step to be taken. The core of the model is to compute the upscaled parameters, namely the *average viscosity*, the *permeability tensor*, and the *source term*, in a suitable way to represent the microscale property of the vascular net. In order to do so, the domain  $\Omega$  has been divided into cuboid subsections called *Representative Elementary Volume* (REV), such that:

$$\overline{\Omega} = \bigcup_{j=1}^{N_{REV}} \overline{REV_j}. \quad (3.3)$$

The size of the subsections has to be set in order to maintain certain scalability to the problem and will be discussed in Chapter 6. In this way, the effective parameters are computed on average for each REV of the domain. This is a suitable strategy to capture the heterogeneities of the vascular network and obtain parameters that summarize its behavior. In the following part, we report the mathematical formulation of these terms, accordingly to [28].

### 3.2.1. Definition of the Upscaled Viscosity $\mu_{bl}^{up}$

To compute the *average viscosity* we define  $I_C$  as the set of the capillaries. Then we set  $I_{C,j} = \{k \in I_C \text{ s.t. } \Lambda_k \cap REV_j \neq \emptyset\}$ ,  $I_{C,j} \subseteq I_C$ , that represents the capillaries that lay in the  $j$ -th REV. After that, we can compute the viscosity as the average of the blood viscosity, which is defined in the equation 3.4.

$$\mu_{bl}(D) = \mu_P \left( 1 + (\mu_{0.45} - 1) \frac{(1 - H)^C - 1}{(1 - 0.45)^C - 1} \cdot \left( \frac{D}{D - 1.1} \right)^2 \right) \cdot \left( \frac{D}{D - 1.1} \right)^2, \quad (3.4)$$

where

$$C = (0.8 + \exp -0.075 * D) \left( -1 + \frac{1}{1 - 10^{-11} D^{12}} \right) + \frac{1}{1 + 10^{-11} D^{12}}, \quad (3.5)$$

and

$$\mu_{0.45} = 6.0 \exp(-0.085 \cdot D) + 3.2 - 2.44 \exp(-0.06 \cdot D^{0.645}). \quad (3.6)$$

These two terms are respectively a coefficient that describes the influence of the discharge hematocrit ( $H$ ) on the in vivo viscosity and the apparent viscosity for  $H = 0.45$ . Note that the entry  $D$  is dimensionless and specific to each edge of the vascular net. Given

this, we can define the viscosity in each REV as follows.

$$\mu_{bl}^{up}(\mathbf{x}) = \mu_{bl,j}^{up}, \quad \mathbf{x} \in \text{REV}_j, \quad \mu_{bl,j}^{up} = \frac{1}{|I_{C,j}|} \sum_{k \in I_{C,j}} \mu_{bl} \left( 2 \cdot \frac{R_k}{\mu\text{m}} \right). \quad (3.7)$$

It should be noted that the formula for in vivo viscosity 3.4 was initially proven for human blood, as stated in [22]. In this work, we will consider both feasible synthetic vascular nets and ones reproducing real networks derived from images of mice brains. However, since an equivalent formula for the average viscosity of the blood of mice is not yet known, we can assume that 3.4 can also hold in these cases.

### 3.2.2. Definition of the Upscaled Permeability Tensor $K_{up}$

A fundamental step of the homogenization strategy is the computation of the permeability tensor. This is the parameter that summarizes the main characteristics of the permeability of the section considered in the vascular net. As stated in Section 2.4, the effective parameter that results from the homogenization process is not diagonal. However, in [8] they reported a study on computer-generated capillary networks, whose properties were comparable with a real-life case, where they computed the permeability tensors. As a result, they obtained off-diagonal terms that were significantly smaller than diagonal ones. Motivated by this, we can make the following assumptions:

- $K_{up}(\mathbf{x}) = K_{up}^{(j)}$ , if  $\mathbf{x} \in \text{REV}_j$ ;
- $K_{up}^{(j)} = \begin{pmatrix} k_x^{(j)} & 0 & 0 \\ 0 & k_y^{(j)} & 0 \\ 0 & 0 & k_z^{(j)}, \end{pmatrix}$  where  $k_x^{(j)}, k_y^{(j)}, k_z^{(j)} > 0$ .

So the tensor is constant on each REV and the off-diagonal entries are considered negligible. This is in accordance with the properties of an effective parameter obtained as a result of the homogenization process, since it is symmetric and positive definite.

Now, the challenge consists of computing the diagonal term of the tensor. In order to do this, an upscaling strategy is used to avoid demanding algorithms, as proposed in [28]. Considering the  $j$ -th REV, the computation is made for each of the three directions, so we obtain a value for each of the three diagonal components of the tensor. Choosing one direction, at the faces not aligned in that direction are assumed no-flow boundary conditions. Instead, for the inlet and outlet faces in the prescribed direction, a negative pressure drop is imposed in order to allow a volume flux (VF) between them. To compute VF, at first, we define as  $\Lambda_{C,j}$  the union of the midlines of the vessels included in  $I_{C,j}$ . Therefore, the volume flux through the outlet  $F_{out,t}^{(j)}$  in the  $t$ -th direction can be defined

as:

$$VF_{out,t}^{(j)} = \sum_{\mathbf{x}_k \in \Lambda_{C,j} \cap F_{out,t}^{(j)}} \frac{\pi R_k^2 K_v(s_k)}{\mu_{bl}} \cdot \frac{\partial p^V}{\partial s}(s_k), \quad (3.8)$$

where  $\mathbf{x}_k = \Lambda_k(s_k)$  for  $k \in I_{C,j}$ , for  $t = (x, y, z)$  and  $R_k$  represents the radius of the k-th edge. In addition to that, we have that  $K_v$  is the permeability of the vessels defined in 2.2, when restricted to the midline  $\Lambda_k$ . Finally, we can approximate the component of the permeability tensor with respect to the j-th REV in this way:

$$k_t^{(j)} \approx \frac{VF_{out,t}^{(j)} \cdot \mu_{bl,j}^{up} \cdot L_t^{(j)}}{(p_{in,t} - p_{out,t}) \cdot \prod_{i \in T - \{t\}} L_i^{(j)}}. \quad (3.9)$$

Where  $L_t^{(j)}$ , for  $t \in T = \{x, y, z\}$ , are the edge lengths of  $REV_j$  in the respective directions and  $p_{in,t} - p_{out,t}$ , is the pressure drop imposed between the inlet and the outlet faces aligned with direction  $t$ .

It is worth noticing that, in the formula 3.8 used to compute the volume flux, the computation of the pressure gradient is required. Therefore, for each REV (and for each direction) we have to approximate the pressure behavior. In order to do so, we exploit the method proposed by [24], where we consider the vessels as perfect cylinders and assume that the flow follows Hagen-Poiseuille law. Moreover, we suppose a linear dependence between the mass flow rate and the pressure difference, namely, for each edge:

$$F = G\Delta p = \frac{\rho A^2}{8\pi\mu L} \Delta p, \quad (3.10)$$

where  $G$  represents the conductance, and  $\Delta p$  is the pressure difference between the two vertices of the edge. Furthermore,  $A$  and  $L$ , represent the cross-sectional area and length of the vessel, respectively. Then, the continuity equation must hold to guarantee the balance of the fluxes at each bifurcation, with the exclusions of the sink and the source nodes. More rigorously, it holds:

$$\frac{\partial V_i}{\partial t} + \frac{1}{\rho} \sum_j G_{ij} (p_i - p_j) = \frac{q_i}{\rho}, \quad (3.11)$$

where the index  $i$  is referred to the i-th node of the vascular network. Moreover,  $\rho$  represents the density and  $q$  is the source term. Finally,  $V_i$  is the volume associated with the node  $i$ , and  $G_{ij} = G_{ji}$  is the conductance associated with the edge that connects the node  $i$  and the node  $j$ . The term  $\frac{\partial V_i}{\partial t}$  can be omitted, since we assume inelastic vessels.

Considering this approximation, the pressure values at each node can be computed by solving the following linear system, where we have defined as  $n$  the total number of nodes

of the vascular net:

$$M\mathbf{p} = \mathbf{q}, \quad (3.12)$$

where  $\mathbf{p} = [p_1, \dots, p_n], \mathbf{q} = [q_1, \dots, q_n]$  and

$$M = \begin{bmatrix} \sum_{j \neq 1} G_{1j} & -G_{12} & & \cdots & & -G_{1n} \\ -G_{21} & \sum_{j \neq 2} G_{2j} & -G_{23} & & \cdots & -G_{2n} \\ \vdots & \ddots & \ddots & \ddots & & \vdots \\ -G_{i1} & \cdots & -G_{ij-1} & \sum_{j \neq i} G_{ij} & -G_{ij+1} & \cdots & -G_{in} \\ \vdots & & & \ddots & \ddots & \ddots & \vdots \\ -G_{n-11} & \cdots & & -G_{n-1n-1} & \sum_{j \neq n-1} G_{n-1j} & -G_{n-1n} \\ -G_{n1} & \cdots & & -G_{nn-1} & -G_{nn-2} & \sum_{j \neq n} G_{nj} \end{bmatrix}$$

Suitable boundary conditions must be defined for this problem. We set as inlet and outlet the faces whose normal is parallel to the chosen direction of computation, and we impose a negative pressure drop between them. Therefore, we choose Dirichlet boundary conditions for those nodes that will be identified as boundary nodes. To do so, we will have to solve a reduced version of problem 3.12 to encounter these conditions, which will be detailed in Chapter 5.

### 3.2.3. Definition of the Source Term $q_t^{cap}$

For this term, it can be used Starling's filtration law. Firstly, the vessel surface area for the  $j$ -th REV can be computed as:

$$S_j = \sum_{k \in I_{C,j}} |\Lambda_{k,j}| 2R_k \pi, \quad (3.13)$$

Where  $\Lambda_{k,j} = \Lambda_k \cap REV_j$ . Then

$$q_t^{cap}(\mathbf{x}) = \frac{\rho_{int} \cdot S_j \cdot L_{cap}}{|REV_j|} (p^t(\mathbf{x}) - p^{cap}(\mathbf{x}) + (\pi_p - \pi_{int})), \quad \mathbf{x} \in REV_j. \quad (3.14)$$

### 3.3. Primal-Pressure Homogenized Model

Summarizing all the formulations defined in the previous sections, the proposed model is reported below:

$$\left\{ \begin{array}{ll} -\nabla \cdot (\rho_{bl} \frac{K_{up}}{\mu_{bl}^{up}} \nabla p^{cap}) = \gamma (p^t - p^{cap} + (\pi_p - \pi_{int})) & \text{in } \Omega, \\ -\nabla \cdot (\rho_{int} \frac{K_t}{\mu_{int}} \nabla p^t) = -\gamma (p^t - p^{cap} + (\pi_p - \pi_{int})) & \text{in } \Omega, \\ p^{cap} = p_D^{cap} & \text{on } \partial\Omega, \\ -\rho_{int} \frac{K_t}{\mu_{int}} \nabla p^t \cdot \mathbf{n} = \beta(p^t - p_0) & \text{on } \partial\Omega. \end{array} \right. \quad \begin{array}{l} (3.15a) \\ (3.15b) \\ (3.15c) \\ (3.15d) \end{array}$$

In this case, the boundary conditions are of Dirichlet type for the capillary bed; instead, we impose Robin for the tissue. This is consistent with the state-of-the-art 3D-1D case 2.1. Moreover, the right-hand side of the equations 3.15a and 3.15b has a parameter  $\gamma$  that has to be defined for each REV, as defined below.

$$\gamma|_{REV_j} = \frac{\rho_{int} \cdot S_j \cdot L_{cap}}{|REV_j|}. \quad (3.16)$$

where  $S_j$  has been defined above. It can be seen that the two models are coupled by the term  $q_t^{cap}$  that represents the interaction between the tissue and the homogenized capillary bed. Numerical discretization has to deal with this condition.

### 3.4. Mixed Homogenized Model

In this section, we proposed a modified version of the homogenized model 3.15, in which we recover the velocity of both the capillary bed and the tissue. This formulation was derived from [9].

$$\left\{ \begin{array}{ll} \frac{1}{\rho_{bl}} [K^{UP}]^{-1} \mathbf{u}^{cap} + \nabla p^{cap} = 0 & \text{in } \Omega, \\ \nabla \cdot \mathbf{u}^{cap} = \gamma (p^t - p^{cap} + (\pi_p - \pi_{int})) & \text{in } \Omega, \\ p^{cap} = p_D^{cap} & \text{on } \partial\Omega. \end{array} \right. \quad \begin{array}{l} (3.17a) \\ (3.17b) \\ (3.17c) \end{array}$$

where  $K^{UP}(\mathbf{x}) = \frac{K^{up}(\mathbf{x})}{\mu_{bl}^{up}(\mathbf{x})}$  for  $\mathbf{x} \in REV_j$ .

The first PDE 3.17a is Darcy's phenomenological law applied to the capillary bed that relates the pressure gradient  $\nabla p^{cap}$  to the velocity  $\mathbf{u}^{cap}$ . Instead, 3.17b is the mass conservation equation. Note that the formulation presented in 3.3 can be obtained from 3.18

by multiplying the first PDE by  $K_{up}$ , explicating  $\mathbf{u}$ , and substituting it into the mass conservation equation. For this problem, we consider Dirichlet boundary conditions as before.

Analogously, we can define a similar formulation for tissue.

$$\left\{ \begin{array}{ll} \frac{1}{K^T} \mathbf{u}^t + \nabla p^t = 0 & \text{in } \Omega, \\ \nabla \cdot \mathbf{u}^t = -\gamma (p^t - p^{\text{cap}} + (\pi_p - \pi_{\text{int}})) & \text{in } \Omega, \\ \mathbf{u}^t \cdot \mathbf{n} = \beta(p^t - p_0) & \text{on } \partial\Omega. \end{array} \right. \quad \begin{array}{l} (3.18a) \\ (3.18b) \\ (3.18c) \end{array}$$

where  $K^T = \rho_{\text{int}} \frac{K_t}{\mu_{\text{int}}}$ .

As for the capillary bed, this model is composed of a Darcy law and a mass conservation law defined for the tissue. In this case, we have a Robin boundary condition, obtained after a reformulation of the one used in 3.15.

# 4 | Numerical Discretization

In this chapter, we discuss the discretization of the homogenized models proposed in Section 3.3 and Section 3.4. First, we present the weak formulation of the pressure problem considering suitable spaces. Then we discretize the model using the Finite Element Method. After that, some results regarding the stability and convergence of this method are reported. Finally, we repeat the discretization process for the mixed model.

## 4.1. Primal Formulation of the Homogenized Model

### 4.1.1. Variational Formulation

To find the weak formulation of our problem, we need to introduce suitable function spaces. Here, we consider the simplified version of the homogenized problem, where the unknowns are the pressure in the capillary bed and the one in the tissue.

Let us define,

$$Q = \{p \in L^2(\Omega), \quad \Omega \subseteq \mathbb{R}^3 : p_{\partial\Omega} = 0\}, \quad (4.1)$$

that is a space appropriate for both the unknowns.

A weak formulation of the problem 3.15 can be obtained by proceeding formally, as follows. Let us multiply the first equation of the model, 3.15a, by a test function  $q^{cap}$  belonging to  $Q$  and integrate on  $\Omega$ . Then, after applying the Green formula to the first term, we obtain:

$$\begin{aligned} & \rho_{bl}(K^{UP} \nabla p^{cap}, \nabla q^{cap})_{\Omega} - \rho_{bl}(K^{UP} \nabla p^{cap} \cdot n, q^{cap})_{\partial\Omega} - \gamma(p^t, q^{cap})_{\Omega} + \\ & + \gamma(p^{cap}, q^{cap})_{\Omega} = \gamma(\pi_p - \pi_{int}, q^{cap})_{\Omega} \quad \forall q^{cap} \in Q, \end{aligned} \quad (4.2)$$

where  $K^{UP}$  and  $\gamma$  were specified before. Moreover, we define

$$(u, v)_{\Omega} = \int_{\Omega} uv \, dx, \quad (4.3a)$$

$$(u, v)_{\partial\Omega} = \int_{\partial\Omega} uv \, d\sigma. \quad (4.3b)$$

The term  $-\rho_{bl}(K^{UP}\nabla p^{cap} \cdot n, q^{cap})_{\partial\Omega}$  can be neglected since  $q^{cap}$  is a function null on  $\partial\Omega$ . The resulting weak form is:

$$\text{find } p^{cap} \in Q : \quad \forall q^{cap} \in Q$$

$$\rho_{bl}(K^{UP}\nabla p^{cap}, \nabla q^{cap})_{\Omega} - \gamma(p^t, q^{cap})_{\Omega} + \gamma(p^{cap}, q^{cap})_{\Omega} = \gamma(\pi_p - \pi_{int}, q^{cap})_{\Omega}. \quad (4.4)$$

Similarly, by multiplying the second equation, 3.15b by a test function  $q^t \in Q$ , then integrating on  $\Omega$  and applying Green formula as before, it follows:

$$\begin{aligned} K^T(\nabla p^t, \nabla q^t)_{\Omega} - K^T(\nabla p^t \cdot n, q^t)_{\partial\Omega} + \gamma(p^t, q^t)_{\Omega} + \\ - \gamma(p^{cap}, q^t)_{\Omega} = -\gamma(\pi_p - \pi_{int}, q^t)_{\Omega} \quad \forall q^t \in Q. \end{aligned} \quad (4.5)$$

In this case, since we have Robin boundary conditions for the tissue, we make the following substitution:

$$-K^T(\nabla p^t \cdot n, q^t)_{\partial\Omega} = \beta(p^t - p^0). \quad (4.6)$$

Then the final formulation is presented in 4.7.

$$\text{find } p^t \in Q : \quad \forall q^t \in Q$$

$$\begin{aligned} K^T(\nabla p^t, \nabla q^t)_{\Omega} + \beta(p^t, q^t)_{\partial\Omega} + \gamma(p^t, q^t)_{\Omega} - \gamma(p^{cap}, q^t)_{\Omega} \\ = -\gamma(\pi_p - \pi_{int}, q^t)_{\Omega} + \beta(p^0, q^t)_{\partial\Omega}, \end{aligned} \quad (4.7)$$

where  $K^T = \rho_{int} \frac{K_t}{\mu_{int}}$ .

In summary, the weak formulation of the problem 3.15 is therefore:

$$\text{find } p^{cap} \in Q, p^t \in Q :$$

$$\left\{ \begin{array}{l} a^{cap}(p^{cap}, q^{cap}) - c(p^t, q^{cap}) + c(p^{cap}, q^{cap}) = L^{cap}(q^{cap}) \quad \forall q^{cap} \in Q, \\ a^t(p^t, q^t) + c(p^t, q^t) - c(p^{cap}, q^t)_{\Omega} = L^t(q^t) \quad \forall q^t \in Q, \end{array} \right. \quad (4.8a)$$

$$(4.8b)$$

where we define the following bilinear form:

$$\begin{aligned} a^{cap}(p, q) &= \rho_{bl}(K^{UP}\nabla p, \nabla q)_{\Omega}, \\ a^t(p, q) &= K^T(\nabla p, \nabla q)_{\Omega} + \beta(p, q)_{\partial\Omega}, \\ c(p, q) &= \gamma(p, q)_{\Omega}, \end{aligned} \quad (4.9)$$

and the right-hand side terms:

$$\begin{aligned} L^{cap}(q) &= \gamma(\pi_p - \pi_{int}, q)_\Omega, \\ L^t(q) &= -\gamma(\pi_p - \pi_{int}, q^t)_\Omega + \beta(p^0, q^t)_{\partial\Omega}. \end{aligned} \quad (4.10)$$

### 4.1.2. FEM Discretization

The next step is the discretization of 4.8 using the Finite Element Method, as shown in deep details in [23]. Let  $Q_h$  be a family of spaces that depends on a positive parameter  $h$ , such that:

$$Q_h \subset Q, \quad \dim Q_h = N_h < \infty \quad \forall h > 0. \quad (4.11)$$

After that, we can define the approximation of problem 4.8 as follows:

find  $p_h^{cap} \in Q_h, p_h^t \in Q_h$ :

$$\left\{ \begin{array}{l} a^{cap}(p_h^{cap}, q_h^{cap}) - c(p_h^t, q_h^{cap}) + c(p_h^{cap}, q_h^{cap}) = L^{cap}(q_h^{cap}) \quad \forall q_h^{cap} \in Q_h, \\ a^t(p_h^t, q_h^t) + c(p_h^t, q_h^t) - c(p_h^{cap}, q_h^t)_\Omega = L^t(q_h^t) \quad \forall q_h^t \in Q_h. \end{array} \right. \quad (4.12a)$$

$$(4.12b)$$

In this case, since we want to approximate the pressure, we choose  $Q_h = \mathbb{P}^1$ , that is, the space of continuous piecewise linear elements. Denoting by  $\{\phi_j, j = 1, 2, \dots, N_h\}$  a base set of  $Q_h$ , we define the approximate variables  $p_h^{cap}$  and  $p_h^t$  as:

$$\begin{aligned} p_h^{cap}(\mathbf{x}) &= \sum_{j=1}^{N_h} p_j^{cap} \phi_j(\mathbf{x}), \\ p_h^t(\mathbf{x}) &= \sum_{j=1}^{N_h} p_j^t \phi_j(\mathbf{x}), \end{aligned} \quad (4.13)$$

where  $p_j^{cap}, p_j^t, j = 1, \dots, N_h$ , are unknown coefficients, respectively, for the capillary bed and the tissue. Since all the functions in the space  $Q_h$  are a linear combination of the basis functions and  $q_h^{cap}, q_h^t$  are selected arbitrarily, we can choose  $q_h^{cap} = q_h^t = \phi_i, i = 1, \dots, N_h$ . Therefore, after substituting the above results into 4.12, we identify the following matrices:

$$\begin{aligned} A_{ij}^{cap} &= a^{cap}(\phi_j, \phi_i), \\ A_{ij}^t &= a^t(\phi_j, \phi_i), \\ C_{ij} &= c(\phi_j, \phi_i), \end{aligned} \quad (4.14)$$

for  $i \in \{1, \dots, N_h\}$ , and  $i \in \{1, \dots, N_h\}$ .

Then, the right-hand side vectors:

$$\begin{aligned} L_i^{cap} &= L^{cap}(\phi_i), \\ L_i^t &= L^t(\phi_i), \end{aligned} \quad (4.15)$$

for  $i \in \{1, \dots, N_h\}$ .

Finally, we obtained the  $2 \times 2$  algebraic block system of 4.12:

$$A\mathbf{p} = \mathbf{L}, \quad (4.16)$$

where

$$\begin{aligned} A &= \begin{bmatrix} A^{cap} + C & -C \\ -C & A^t + C \end{bmatrix} \\ L &= \begin{bmatrix} \mathbf{L}^{cap} \\ \mathbf{L}^t \end{bmatrix} \end{aligned}$$

The unknown block vector can be written as

$$p = \begin{bmatrix} \mathbf{p}^{cap} \\ \mathbf{p}^t \end{bmatrix}$$

where  $\mathbf{p}^{cap} = \{p_j^{cap}\}_{j=1,\dots,N_h}$  and  $\mathbf{p}^t = \{p_j^t\}_{j=1,\dots,N_h}$ . Therefore,  $A$  is a matrix  $2N_h \times 2N_h$ ,  $\mathbf{p} \in \mathbb{R}^{2N_h}$  and  $\mathbf{L} \in \mathbb{R}^{2N_h}$ .

It is worth noticing that we obtain a system of block matrices. In this way, we were able to deal properly with the coupling of the problem. Details about the implementation of the method and the approaches used to compute the solution of 4.16, will be discussed in Chapter 5.

### 4.1.3. Existence and Uniqueness

In order to prove the existence and uniqueness of the solution for this problem 4.12 we recall the Lax-Milgram lemma, which is widely used for this type of problem [4],[23].

**Lemma 1.** *Let  $V$  be Hilbert space, and let  $a(\cdot, \cdot)$  be a bilinear continuous form on  $V$ . Assume that  $a$  is coercive, that is*

$$\exists \alpha > 0 \quad \text{such that } a(v, v) \geq \alpha \|v\|_V^2, \quad \forall v \in V. \quad (4.17)$$

*Then, for every  $f \in V'$ , the problem:*

find  $u \in V$  such that

$$a(u, v) = (f, v)_{V \times V'}, \quad (4.18)$$

has a unique solution.

Moreover, this theorem can be used for both continuous and discretized formulation.

In order to apply this result to our discretization, problem 4.12 has to be rewritten to be compatible with the formulation of the book. In particular, we define the following bilinear forms:

$$\mathcal{A}([p_1, p_2], [q_1, q_2]) = \begin{bmatrix} a^{cap}(p_1, q_1) \\ a^t(p_2, q_2) \end{bmatrix}$$

$$\mathcal{C}([p_1, p_2], [q_1, q_2]) = \begin{bmatrix} c(p_1 - p_2, q_1) \\ c(p_2 - p_1, q_2) \end{bmatrix} \quad (4.19)$$

$$\mathcal{L}([q_1, q_2]) = \begin{bmatrix} L^{cap}(q_1) \\ L^t(q_2) \end{bmatrix}$$

Therefore, the problem can be rewritten as follows:

find  $\mathbf{p}_h = [p_h^{cap}, p_h^t] \in \mathcal{Q}_h$ :

$$\mathcal{A}(\mathbf{p}_h, \mathbf{q}_h) + \mathcal{C}(\mathbf{p}_h, \mathbf{q}_h) = \mathcal{L}(\mathbf{q}_h), \quad \forall \mathbf{q}_h \in \mathcal{Q}_h, \quad (4.20a)$$

where  $\mathcal{Q} = Q \times Q$ .

Finally, we can state that, since the hypotheses of the Lax-Milgram lemma 1 are satisfied, it can be applied to 4.8.

## 4.2. Mixed Formulation of the Homogenized Model

### 4.2.1. Variational Formulation

In this Section, we derive the weak formulation and the discretization of the problem 3.17-3.18. In this case, we also have to deal with the variables of the capillary bed velocity and the tissue velocity.

Let us define,

$$\begin{aligned} Q &= \{p \in L^2(\Omega), \quad \Omega \subseteq \mathbb{R}^3 : p_{\partial\Omega} = 0\}, \\ V &= \{\mathbf{v} \in H_0^1(\Omega), \quad \Omega \subseteq \mathbb{R}^3 : (\mathbf{v} \cdot \mathbf{n})_{\partial\Omega} = 0\}. \end{aligned} \quad (4.21)$$

as the function space for the pressure and the velocity respectively. As before, the weak formulation of the problem can be obtained by multiplying the first equation of the model, 3.17, by a test function  $\mathbf{v}^{cap}$  belonging to  $V$  and integrating on  $\Omega$ . Instead, for the second equation, we consider it as a test function  $q^{cap}$  belonging to  $Q$ . The same formulation 4.3 is applied for the integrals.

$$\begin{cases} \frac{1}{\rho_{bl}}([K^{UP}]^{-1}\mathbf{u}^{cap}, \mathbf{v}^{cap})_\Omega + (\nabla p^{cap}, \mathbf{v}^{cap})_\Omega = 0 & \forall \mathbf{v}^{cap} \in V, \\ (\nabla \cdot \mathbf{u}^{cap}, q^{cap})_\Omega - \gamma(p^t, q^{cap})_\Omega + \gamma(p^{cap}, q^{cap})_\Omega \\ = \gamma(\pi_p - \pi_{int}, q^{cap})_\Omega & \forall q^{cap} \in Q. \end{cases} \quad (4.22a)$$

$$(4.22b)$$

Then we apply the Green formula to the gradient term in 4.22a obtaining

$$(\nabla p^{cap}, \mathbf{v}^{cap})_\Omega = (p^{cap}, \mathbf{v}^{cap} \cdot \mathbf{n})_{\partial\Omega} - (\nabla \cdot \mathbf{v}^{cap}, p^{cap})_\Omega = -(\nabla \cdot \mathbf{v}^{cap}, p^{cap})_\Omega. \quad (4.23)$$

For symmetry purposes, we can omit the first term since  $\mathbf{v}^{cap} \cdot \mathbf{n}$  is zero on the boundary, for the space choice that we made. However, the actual implementation of this problem will require this term to be present in the actual formulation. More details are discussed in Chapter 5. Moreover, we also have to multiply for -1 equation 4.22b, in order to have coherent results with 4.22a. The weak formulation for the capillary beds reads:

*find*  $[\mathbf{u}^{cap}, p^{cap}] \in V \times Q$  :

$$\begin{cases} \frac{1}{\rho_{bl}}([K^{UP}]^{-1}\mathbf{u}^{cap}, \mathbf{v}^{cap})_\Omega - (\nabla \cdot \mathbf{v}^{cap}, p^{cap})_\Omega = 0 & \forall \mathbf{v}^{cap} \in V, \end{cases} \quad (4.24a)$$

$$\begin{cases} -(\nabla \cdot \mathbf{u}^{cap}, q^{cap})_\Omega + \gamma(p^t, q^{cap})_\Omega - \gamma(p^{cap}, q^{cap})_\Omega \\ = -\gamma(\pi_p - \pi_{int}, q^{cap})_\Omega & \forall q^{cap} \in Q. \end{cases} \quad (4.24b)$$

Similarly, we find the weak formulation for the tissue mixed problem, using as test functions  $\mathbf{v}^t \in V$  for the Darcy law of the tissue, and  $\mathbf{q}^t \in Q$  for the mass conservation equation, as follows:

$$\begin{cases} \frac{1}{K^T}(\mathbf{u}^t, \mathbf{v}^t)_\Omega + (\nabla p^t, \mathbf{v}^t)_\Omega = 0 & \forall \mathbf{v}^t \in V, \end{cases} \quad (4.25a)$$

$$\begin{cases} (\nabla \cdot \mathbf{u}^t, q^t)_\Omega + \gamma(p^t, q^t)_\Omega - \gamma(p^{cap}, q^t)_\Omega = -\gamma(\pi_p - \pi_{int}, q^t)_\Omega & \forall q^t \in Q. \end{cases} \quad (4.25b)$$

Thanks to the Green formula we find the following expression regarding equation 4.25b.

$$(\nabla \cdot \mathbf{u}^t, q^t)_\Omega = (\mathbf{u}^t \cdot \mathbf{n}, q^t)_{\partial\Omega} - (\mathbf{u}^t, \nabla q^t)_\Omega = \beta(p^t - p^0, q^t)_{\partial\Omega} - (\mathbf{u}^t, \nabla q^t)_\Omega. \quad (4.26)$$

The last identity has been obtained after the application of the Robin boundary condition. Even in this case, we change the signs of equation 4.25b.

It is worth noticing that for the tissue we integrate by parts the mass conservation equation, which is different from what is done for the capillary case where the green formula was applied to the Darcy law. The reasoning behind this choice is that the two problems must answer different boundary conditions. In the end, we obtained a mixed dual formulation, where in the capillary the symmetry between the Darcy law and the mass conservation equation is expressed concerning the divergence operator, while in the tissue it is used as the gradient operator.

Therefore, the final weak formulation of the problem for the tissue reads:

*find*  $[\mathbf{u}^t, p^t] \in V \times Q$ :

$$\left\{ \begin{array}{l} \frac{1}{K^T}(\mathbf{u}^t, \mathbf{v}^t)_\Omega + (\nabla p^t, \mathbf{v}^t)_\Omega = 0 \quad \forall \mathbf{v}^t \in V, \\ (\mathbf{u}^t, \nabla q^t)_\Omega - \beta(p^t, q^t)_{\partial\Omega} - \gamma(p^t, q^t)_\Omega + \gamma(p^{cap}, q^t)_\Omega \end{array} \right. \quad (4.27a)$$

$$\left. \begin{array}{l} = \gamma(\pi_p - \pi_{int}, q^t)_\Omega - \beta(p^0, q^t)_{\partial\Omega} \quad \forall q^t \in Q. \end{array} \right. \quad (4.27b)$$

In the end, the weak formulation of problem 3.17-3.18 is summarized in 4.28.

*find*  $[\mathbf{u}^{cap}, p^{cap}] \in V \times Q$ ,  $[\mathbf{u}^t, p^t] \in V \times Q$ :

$$\left\{ \begin{array}{l} a^{cap}(\mathbf{u}^{cap}, \mathbf{v}^{cap}) + b^{cap}(\mathbf{v}^{cap}, p^{cap}) = 0 \quad \forall \mathbf{v}^{cap} \in V, \\ a^t(\mathbf{u}^t, \mathbf{v}^t) + b^t(\mathbf{v}^t, p^t) = 0 \quad \forall \mathbf{v}^t \in V, \end{array} \right. \quad (4.28a)$$

$$\left. \begin{array}{l} b^{cap}(\mathbf{u}^{cap}, q^{cap}) + c(p^t, q^{cap}) - c(p^{cap}, q^{cap}) = -L^{cap}(q^{cap}) \quad \forall q^{cap} \in Q, \\ b^t(\mathbf{u}^t, q^t) - c^t(p^t, q^t) + c(p^{cap}, q^t) = -L^t(q^t) \quad \forall q^t \in Q. \end{array} \right. \quad (4.28c)$$

$$\left. \begin{array}{l} b^{cap}(\mathbf{u}^{cap}, q^{cap}) + c(p^t, q^{cap}) - c(p^{cap}, q^{cap}) = -L^{cap}(q^{cap}) \quad \forall q^{cap} \in Q, \\ b^t(\mathbf{u}^t, q^t) - c^t(p^t, q^t) + c(p^{cap}, q^t) = -L^t(q^t) \quad \forall q^t \in Q. \end{array} \right. \quad (4.28d)$$

where we define the following bilinear forms:

$$\begin{aligned} a^{cap}(\mathbf{u}, \mathbf{v}) &= \frac{1}{\rho_{bl}}([K^{UP}]^{-1}\mathbf{u}, \mathbf{v})_\Omega, \\ a^t(\mathbf{u}, \mathbf{v}) &= \frac{1}{K^T}(\mathbf{u}, \mathbf{v})_\Omega, \\ b^{cap}(\mathbf{u}, q) &= -(q, \nabla \cdot \mathbf{u})_\Omega, \\ b^t(\mathbf{u}, q) &= (\nabla q, \mathbf{u})_\Omega \\ c(p, q) &= \gamma(p, q)_\Omega, \\ c^t(p, q) &= \gamma(p, q)_\Omega + \beta(p, q)_{\partial\Omega}, \end{aligned} \quad (4.29)$$

and the right-hand side terms:

$$\begin{aligned} L^{cap}(q) &= \gamma(\pi_p - \pi_{int}, q)_\Omega, \\ L^t(q) &= -\gamma(\pi_p - \pi_{int}, q^t)_\Omega + \beta(p^0, q^t)_{\partial\Omega}. \end{aligned} \quad (4.30)$$

### 4.2.2. FEM Discretization

As before, we proceed with the discretization of 4.28 using the Finite Element Method. Let  $V_h, Q_h$  be two families of spaces that depend on a positive parameter  $h$ , such that:

$$\begin{aligned} V_h &\subset V, \quad \dim V_h = N_h < \infty \quad \forall h > 0, \\ Q_h &\subset Q, \quad \dim Q_h = M_h < \infty \quad \forall h > 0. \end{aligned} \quad (4.31)$$

The approximation of the problem comes straightforwardly as:

$$\text{find } [\mathbf{u}_h^{cap}, p_h^{cap}] \in V_h \times Q_h, \quad [\mathbf{u}_h^t, p_h^t] \in V_h \times Q_h :$$

$$a^{cap}(\mathbf{u}_h^{cap}, \mathbf{v}_h^{cap}) + b^{cap}(\mathbf{v}_h^{cap}, p_h^{cap}) = 0 \quad \forall \mathbf{v}_h^{cap} \in V_h, \quad (4.32a)$$

$$a^t(\mathbf{u}_h^t, \mathbf{v}_h^t) + b^t(\mathbf{v}_h^t, p_h^t) = 0 \quad \forall \mathbf{v}_h^t \in V_h, \quad (4.32b)$$

$$b^{cap}(\mathbf{u}_h^{cap}, q_h^{cap}) + c(p_h^t, q_h^{cap}) - c(p_h^{cap}, q_h^{cap}) = -L^{cap}(q_h^{cap}) \quad \forall q_h^{cap} \in Q_h, \quad (4.32c)$$

$$b^t(\mathbf{u}_h^t, q_h^t) - c^t(p_h^t, q_h^t) + c(p_h^{cap}, q_h^t) = -L^t(q_h^t) \quad \forall q_h^t \in Q_h. \quad (4.32d)$$

To define suitable spaces for both the velocity and the pressure approximation, it was decided to use Taylor-Hood elements  $P_2 - P_1$ , which are the spaces of continuous polynomials with quadratic and linear degree, respectively, when restricted to an element. This is usually a very safe option since this couple guarantees stability. Therefore, let us define  $\{\psi_j, j = 1, 2, \dots, N_h\}$  as basis set for  $V_h$ , and  $\{\phi_l, l = 1, 2, \dots, M_h\}$  as one for  $Q_h$ . Then the approximated solutions can be written as a linear combination of the respective basis sets, namely:

$$\begin{aligned} \mathbf{u}_h^{cap}(\mathbf{x}) &= \sum_{j=1}^{N_h} u_j^{cap} \psi_j(\mathbf{x}), \\ \mathbf{u}_h^t(\mathbf{x}) &= \sum_{j=1}^{N_h} u_j^t \psi_j(\mathbf{x}), \\ p_h^{cap}(\mathbf{x}) &= \sum_{l=1}^{N_h} p_l^{cap} \phi_l(\mathbf{x}), \\ p_h^t(\mathbf{x}) &= \sum_{l=1}^{N_h} p_l^t \phi_l(\mathbf{x}), \end{aligned} \quad (4.33)$$

where  $u_j^{cap}, u_j^t, j = 1 \dots M_h$  are the unknown coefficients for the capillary bed and tissue velocities. Instead,  $p_l^{cap}, p_l^t, l = 1 \dots N_h$ , refers to the pressure coefficients of both models. Now it is sufficient that 4.28 is verified for all functions of the basis sets of the respective function space. Therefore, we choose  $\mathbf{v}_h^{cap} = \mathbf{v}_h^t = \psi_i$ , for  $i = 1, \dots, M_h$ , and  $q_h^{cap} = q_h^t = \phi_m$ , for  $m = 1, \dots, N_h$ . After that, we can identify the following submatrices of our system, obtained by substituting the previous results in 4.32:

$$\begin{aligned} A_{ij}^{cap} &= a^{cap}(\psi_j, \psi_i), \\ A_{ij}^t &= a^t(\psi_j, \psi_i), \\ B_{lj}^{cap} &= b^{cap}(\psi_j, \phi_l), \\ B_{lj}^t &= b^t(\psi_j, \phi_l), \\ \tilde{C}_{lm} &= c(\phi_m, \phi_l), \\ C_{lm}^t &= c^t(\phi_m, \phi_l), \end{aligned} \tag{4.34}$$

for  $i \in \{1, \dots, M_h\}, j \in \{1, \dots, M_h\}, l \in \{1, \dots, N_h\}, m \in \{1, \dots, N_h\}$ . Therefore, we propose a reorganization of the matrices above, obtaining the following block matrices:

$$A = \begin{bmatrix} A^{cap} & 0 \\ 0 & A^t \end{bmatrix}$$

$$B = \begin{bmatrix} B^{cap} & 0 \\ 0 & B^t \end{bmatrix}$$

$$C = \begin{bmatrix} \tilde{C} & -\tilde{C} \\ -\tilde{C} & C^t \end{bmatrix}$$

where the dimensions are:

- $A: 2M_h \times 2M_h$ ;
- $B: 2N_h \times 2M_h$ ;
- $C: 2N_h \times 2N_h$ .

Then the full algebraic problem of 4.32 can be written as:

$$T\mathbf{s} = \mathbf{L}, \tag{4.35}$$

where the  $4 \times 4$  block matrix  $\mathbf{T}$  and the  $4 \times 1$  right-hand side block vector  $\mathbf{L}$  can be defined as:

$$\mathbf{T} = \begin{bmatrix} A & B^T \\ B & -C \end{bmatrix}$$

$$\mathbf{L} = \begin{bmatrix} \mathbf{0} \\ \mathbf{0} \\ -\mathbf{L}^{cap} \\ -\mathbf{L}^t \end{bmatrix}$$

Lastly, we define the block vector of the solution

$$\mathbf{s} = \begin{bmatrix} \mathbf{u}^{cap} \\ \mathbf{u}^t \\ \mathbf{p}^{cap} \\ \mathbf{p}^t \end{bmatrix}$$

where the velocity coefficients are  $\mathbf{u}^{cap} = \{u_j^{cap}\}_{j=1,\dots,M_h}$  and  $\mathbf{u}^t = \{u_j^t\}_{j=1,\dots,M_h}$ , while the pressure's ones  $\mathbf{p}^{cap} = \{p_l^{cap}\}_{l=1,\dots,N_h}$  and  $\mathbf{p}^t = \{p_l^t\}_{l=1,\dots,N_h}$ . Therefore, the matrix  $\mathbf{T}$  has dimensions  $(2M_h + 2N_h) \times (2M_h + 2N_h)$ ,  $\mathbf{s} \in \mathbb{R}^{2M_h+2N_h}$  and  $\mathbf{L} \in \mathbb{R}^{2M_h+2N_h}$ .

Notice that, as happened for the discretization in Section 4.1.2, we obtained a block system that allows us to deal with the coupling of the equations. The details of the implementation are discussed in Chapter 5.

### 4.2.3. Existence and Uniqueness and Error Estimates

In this chapter, we discuss the existence and uniqueness of the solution of the discretized problem 4.32, exploring some results presented in [4]. In addition to that, we also report some error estimates found in the book.

Let us define at first the assumptions:

**Proposition 4.1.** *We are given two Hilbert spaces,  $V$  and  $Q$ , and three continuous bilinear forms:  $a(\cdot, \cdot)$  on  $V \times V$ ,  $b(\cdot, \cdot)$  on  $V \times Q$  and  $c(\cdot, \cdot)$  on  $Q \times Q$ . We denote by  $A$ ,  $B$ , and  $C$  the linear continuous operators associated with them. Moreover, we assume that  $ImB$  is closed, a that  $a(\cdot, \cdot)$  and  $c(\cdot, \cdot)$  are symmetric and positive semi-definite.*

then we consider the continuous weak formulation of a general mixed problem:

find  $\mathbf{u} \in V, p = \in Q :$

$$\begin{cases} a(\mathbf{u}, \mathbf{v}) + b(\mathbf{v}, p) = (f, v)_{V' \times V}, & \forall \mathbf{v} \in V, \\ b(\mathbf{u}, q) - c(p, q) = (g, q)_{Q' \times Q}, & \forall q \in Q. \end{cases} \quad (4.36a)$$

$$(4.36b)$$

Moreover, another proposition for the discretized case is necessary:

**Proposition 4.2.** *Together with Proposition 4.1, we assume that we are given two finite-dimensional subspaces  $V_h \subseteq V$  and  $Q_h \subseteq Q$ .*

The discretized version of 4.36

is the following, find  $\mathbf{u}_h \in V_h, p_h = \in Q_h :$

$$\begin{cases} a(\mathbf{u}_h, \mathbf{v}_h) + b(\mathbf{v}_h, p_h) = (f, v_h)_{V'_h \times V_h}, & \forall \mathbf{v}_h \in V_h, \\ b(\mathbf{u}_h, q_h) - c(p_h, q_h) = (g, q_h)_{Q'_h \times Q_h}, & \forall q_h \in Q_h. \end{cases} \quad (4.37a)$$

$$(4.37b)$$

Furthermore, requiring additional assumption on the bilinear form  $c(\cdot, \cdot)$ , that is:

$$c(\cdot, \cdot) = \lambda(p, q)_Q, \quad (4.38)$$

where  $\lambda$  is a positive real number, possibly tending to 0. Moreover, each  $v_h \in V_h$  might be split as  $v = v_0^h + \bar{v}_h$ , with  $v_0^h \in K_h$  and  $\bar{v}_h \in K_h^\perp$ . Finally, we can state the following results:

**Theorem 4.1.** *Together with Proposition 4.2, assume that  $a(\cdot, \cdot)$  is coercive on  $K_h$  and  $c(\cdot, \cdot)$  is given in 4.38. Let  $\alpha_0^h$ , and  $\beta_h$ , be defined as:*

$$\alpha_0^h \|v_0^h\|_V^2 \leq a(v_0^h, v_0^h), \quad \forall v_0^h \in K_h,$$

$$\inf_{q_h \in H_h^\perp} \sup_{v_h \in V_h} \frac{b(v_h, q_h)}{\|q_h\|_Q \|v_h\|_V} = \inf_{v_h \in K_h^\perp} \sup_{q_h \in Q_h} \frac{b(v_h, q_h)}{\|q_h\|_Q \|v_h\|_V} = \beta_h > 0.$$

*Then, for every  $f \in V'$  and  $g \in Q'$ , we find that the discretized problem 4.37 has a unique solution. Moreover, if  $(u, p)$  is a solution of the continuous problem 4.36, then for every  $u_I \in V_h$  and for every  $p_I \in Q_h$  we have the estimates*

$$\|u_h - u_I\|_V \leq \frac{\beta_h^2 + 4\lambda\|a\|}{\alpha_0^h \beta_h^2} \|\mathcal{F}^h\|_{V'} + \frac{2\|a\|^{1/2}}{\alpha_0^{h/2} \beta_h} \|\bar{\mathcal{G}}^h\|_{Q'}, \quad (4.39)$$

$$\|\bar{p}_h - \bar{p}_I\|_Q \leq \frac{2\|a\|^{1/2}}{\alpha_0^{h^{1/2}}\beta_h} \|\mathcal{F}^h\|_{V'} + \frac{4\|a\|}{\lambda\|a\| + 2\beta_h^2} \|\bar{\mathcal{G}}^h\|_{Q'}, \quad (4.40)$$

$$\|(p_h - p_I)_0\|_Q \leq \frac{1}{\lambda} \|\mathcal{G}_0^h\|_{Q'}. \quad (4.41)$$

To apply these results to our discretization, problem 4.32 has to be rewritten to be compatible with the formulation of the book. In particular, we define the following bilinear forms:

$$\begin{aligned} \mathcal{A}([\mathbf{u}_1, \mathbf{u}_2], [\mathbf{v}_1, \mathbf{v}_2]) &= \begin{bmatrix} a^{cap}(\mathbf{u}_1, \mathbf{v}_1) \\ a^t(\mathbf{u}_2, \mathbf{v}_2) \end{bmatrix} \\ \mathcal{B}([\mathbf{u}_1, \mathbf{u}_2], [q_1, q_2]) &= \begin{bmatrix} b^{cap}(\mathbf{u}_1, q_1) \\ b^t(\mathbf{u}_2, q_2) \end{bmatrix} \\ \mathcal{C}([p_1, p_2], [q_1, q_2]) &= \begin{bmatrix} c(p_1 - p_2, q_1) \\ -c(p_1 - p_2, q_2) \end{bmatrix} \\ \mathcal{C}_\Omega([p_1, p_2], [q_1, q_2]) &= \begin{bmatrix} 0 \\ \beta(p_2, q_2)_{\partial\Omega} \end{bmatrix} \\ \mathcal{L}([q_1, q_2]) &= \begin{bmatrix} -L^{cap}(q_1) \\ -L^t(q_2) \end{bmatrix} \end{aligned} \quad (4.42)$$

where the bilinear forms described in 4.29, have been unified in order to rewrite the continuous weak problem 4.28 in the following formulation:

*find*  $\mathbf{u} = [\mathbf{u}^{cap}, \mathbf{u}^t] \in \mathcal{V}$ ,  $\mathbf{p} = [p^{cap}, p^t] \in \mathcal{Q}$ :

$$\left\{ \begin{array}{l} \mathcal{A}(\mathbf{u}, \mathbf{v}) + \mathcal{B}(\mathbf{v}, \mathbf{p}) = \mathbf{0}, \quad \forall \mathbf{v} \in \mathcal{V}, \\ \mathcal{B}(\mathbf{u}, \mathbf{q}) - \mathcal{C}(\mathbf{p}, \mathbf{q}) - \mathcal{C}_\Omega(\mathbf{p}, \mathbf{q}) = \mathcal{L}(\mathbf{q}), \quad \forall \mathbf{q} \in \mathcal{Q}, \end{array} \right. \quad (4.43a)$$

$$\left\{ \begin{array}{l} \mathcal{B}(\mathbf{u}, \mathbf{q}) - \mathcal{C}(\mathbf{p}, \mathbf{q}) - \mathcal{C}_\Omega(\mathbf{p}, \mathbf{q}) = \mathcal{L}(\mathbf{q}), \quad \forall \mathbf{q} \in \mathcal{Q}, \end{array} \right. \quad (4.43b)$$

where  $\mathcal{V} = V \times V$ ,  $\mathcal{Q} = Q \times Q$ , and the test functions  $\mathbf{v}$  and  $\mathbf{q}$  has to be thought in this way respectively,  $\mathbf{v} = [\mathbf{v}^{cap}, \mathbf{v}^t]$ ,  $\mathbf{q} = [\mathbf{q}^{cap}, \mathbf{q}^t]$ .

After that, we present also the rewritten formulation of 4.32, considering the discretized spaces  $\mathcal{V}_h \subseteq V$  and  $\mathcal{Q}_h \subseteq Q$ .

$$\text{find } \mathbf{u}_h = [\mathbf{u}_h^{cap}, \mathbf{u}_h^t] \in \mathcal{V}_\zeta, \quad \mathbf{p}_h = [p_h^{cap}, p_h^t] \in \mathcal{Q}_\zeta :$$

$$\left\{ \begin{array}{l} \mathcal{A}(\mathbf{u}_h, \mathbf{v}_h) + \mathcal{B}(\mathbf{v}_h, \mathbf{p}_h) = \mathbf{0}, \quad \forall \mathbf{v}_h \in \mathcal{V}_h, \\ \mathcal{B}(\mathbf{u}_h, \mathbf{q}_h) - \mathcal{C}(\mathbf{p}_h, \mathbf{q}_h) - \mathcal{C}_\Omega(\mathbf{p}_h, \mathbf{q}_h) = \mathcal{L}(\mathbf{q}_h), \quad \forall \mathbf{q}_h \in \mathcal{Q}_h. \end{array} \right. \quad (4.44a)$$

$$(4.44b)$$

Finally, we can state that, since the continuous problem 4.43 and the discretized 4.44 are now respectively formulated as 4.36,4.37, considering  $f = 0$ . Therefore, Theorem 4.1 holds, since the assumptions are satisfied. The bilinear forms used are widely studied in literature and their properties have been proved several times. For further details, one can see [23]. Nevertheless, it is interesting to prove that  $\mathcal{C}$  and  $\mathcal{C}_\Omega$  are semi-definite positive, namely:

$$\mathcal{C}(p, p) \geq 0, \quad \forall p \in Q \quad \text{and} \quad \mathcal{C}_\Omega(p, p) \geq 0, \quad \forall p \in Q. \quad (4.45)$$

Therefore, starting from  $\mathcal{C}$ , it is sufficient to show, taking  $q_1 = p_1 - p_2 = p \in Q$ :

$$c(p, p) = C(p, p)_\Omega = C \int_\Omega p^2 dx = C \|p\|_{L^2(\Omega)}^2 \geq 0, \quad \forall p \in Q, \quad (4.46)$$

Similarly, we can prove the property for  $\mathcal{C}_\Omega$ , taking  $p = q$  :

$$\beta(p, p)_{\partial\Omega} = \beta \int_{\partial\Omega} p^2 dx = \beta \|p\|_{L^2(\partial\Omega)}^2 \geq 0, \quad \forall p \in Q, \quad (4.47)$$

since  $C \geq 0$  and  $\beta \geq 0$ , we can conclude that the bilinear forms  $\mathcal{C}$  and  $\mathcal{C}_\Omega$  are semi-definite positive. Therefore, all the hypotheses of the theorem 4.1 are satisfied.



# 5 | Implementation

In this chapter, we describe the details on the implementation of the method used to solve the problems presented in Chapter 3 and discretized in Chapter 4.

To solve homogenized problems, both primal pressure and mixed versions, the challenge consists in the computation of the effective parameters that have been defined in 3.2. In fact, after the computation, these will be used to solve homogenized models and obtain the averaged quantities for both the capillary bed and the tissue. The results collected with the methods described in this chapter will be presented and commented on in Chapter 6. This work has been divided into two parts. At first, it is necessary to create an algorithm to successfully compute the upscaled parameters. In particular, the most challenging part is the division of the vascular network into Representative Elementary Volumes (REVs). After that, the problems are solved using the Python libraries.

## 5.1. Computation of the Homogenized Parameters

As explained in Chapter 2, the baseline of the homogenization method is to simplify the problem of identifying some parameters that can describe a microscopic behavior to the macroscale level. To do so, we obtained the homogenized version of our starting problem, namely 3.15 in which we recognize the parameters that are the results of the upscaling procedure. In this specific case, the challenge is to compute three quantities defined in 3.2:

- $K^{up}$ : the *permeability tensor* of the vascular network;
- $\mu_{bl}^{up}$ : the *average blood viscosity*;
- $\gamma$ : that is the multiplication parameter of the Starling Filtration law, used as coupling term for the model.

These parameters summarize the whole behavior of the capillary network, in order to consider the capillary bed as a 3D-porous medium, that can be modeled by the Darcy equation.

The main aspect of this process is to divide the vascular net into Representative Elemen-

tary Volumes (REV). The setting of the problem we are dealing with is a 1D vascular net embedded in a cubic structure that represents the tissue, as we detailed in section 2.1. An example of a 1D vascular net can be seen in Figure 5.1. Each vascular net is identified with the vertices, edges, radii, and labels that represent the belonging of each point to the inlet, outlet, or internal region.

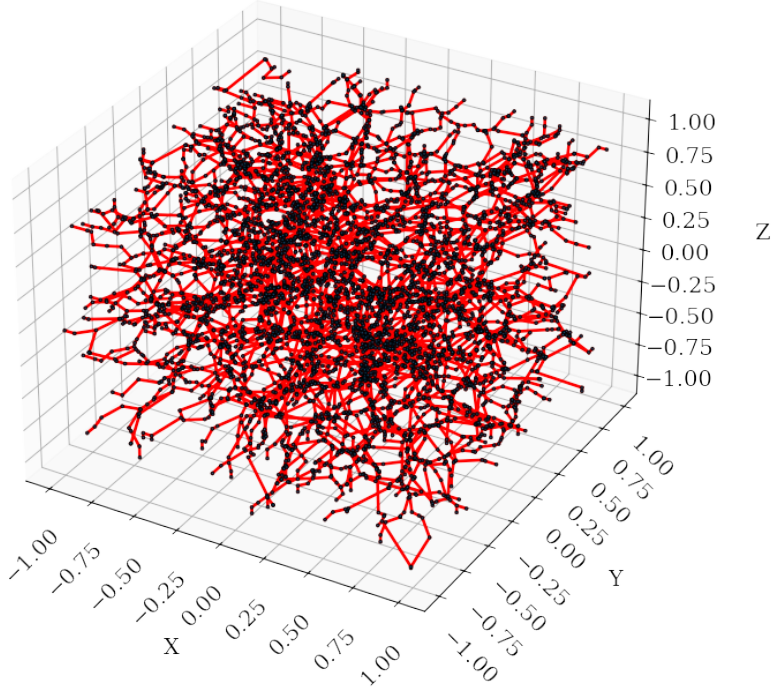


Figure 5.1: Example of a synthetic 1D vascular net.

Once obtained the structure of subnets of the original vascular domain, one can perform the computation of the parameters described above. The challenging part is the computation of the upscaled permeability tensor for which the simulation of the pressure of the blood flow on the nodes of each subnet is required.

### 5.1.1. REV Division Algorithm

The REV division process consists of dividing the vascular network into suitable subdomains to calculate for each the effective parameters. In this way, we gather microscale information about the vascular net depending on the positions, which can be used in the 3D homogenized model.

The subdivision of the domain is not straightforward since it has some important concerns. At first, the size of each REV has to be chosen in such a way as to maintain the properties of the vascular net. In fact, choosing a size that is too small could lead to

an unfeasible division of the network, with several cubic regions but with an unrealistic capillary bed inside each one of them. As a criterion for understanding the correct size, we hope to maintain a correct balance between the boundary points and the interior points for each REV, as we will detail later in Chapter 6. Another difficulty can arise after proper division of the vascular net. The segmentation process could lead to unfeasible branches that do not communicate with the rest of the REV's vascular network. A deep post-processing of the resulting networks has to be performed to obtain appropriate networks for the computation of the parameters.

As a first step, we decide to use a cubic region of  $2 \times 2 \times 2 \text{ mm}^3$ , where each edge is between  $[-1, 1]$ . For this reason, each vascular network used for the studies is scaled accordingly. We aim to create a general code that can provide the heterogeneous subdivisions of the networks given as input. Therefore, the algorithm takes as input the variables `n_div_x,n_div_y,n_div_z`, which allows the user to set the number of divisions for each one of the axes. In fact, each edge of the cube is divided equally to obtain the chosen number of divisions for each side. In this way, one can progressively decrease the REV size by increasing the number of divisions, looking for the minimum number of REVs that maintains the vascular properties. Here, we are just creating the geometric framework of the subdomains without actively partitioning the vascular network. All information about the segmented domain is stored in a `Python` dictionary, a very efficient and flexible container, using as key the REV number, from 1 to  $\text{n\_div\_x} * \text{n\_div\_y} * \text{n\_div\_z}$ , in order to recall all the necessary information for each REV.

The second step is the division of the vascular network. The easy part is the partitioning of the vertices. Looking at each vertex's coordinates, we can identify its belonging to a specific REV domain. Therefore, each vertex is assigned with a label representing the identification number of its REV. In addition to that, the indexes of the vertices in a specific region are stored in the dictionary under the suitable key. The pseudo-algorithm for the REV division can be seen in 5.1.

---

**Algorithm 5.1** REV division

---

```

1: Input: n_div_x, n_div_y, n_div_z
2: Initialize the dictionary REV_division, and the REV_label
3: Define the REV counter
4: for i in linspace(xmin, xmax, n_div_x+1) do
5:   for j in linspace(ymin, ymax, n_div_y+1) do
6:     for k in linspace(zmin, zmax, n_div_z+1) do
7:       Save the geometric information about the current REV
8:       Save the indexes of the vertices of the net that are in the current REV
9:       Assigning the REV labels for these indexes
10:      REV = REV + 1
11:    end for
12:  end for
13: end for

```

---

The toughest part about dividing a vascular net is dealing with the edges. As shown in Figure 5.1, an edge can be defined as the line that connects two vertices. In order to create the vascular subnet for each REV the edges have to be properly identified to the vertices they are connecting, in order to understand their geometrical position to assign them to the right REV. First, we identify all the edges connecting two vertices that belong to the same REV, by looking at the labels computed above. Then we have to deal with the edges that connect the vertices belonging to different subdivisions, as shown in Figure 5.2.

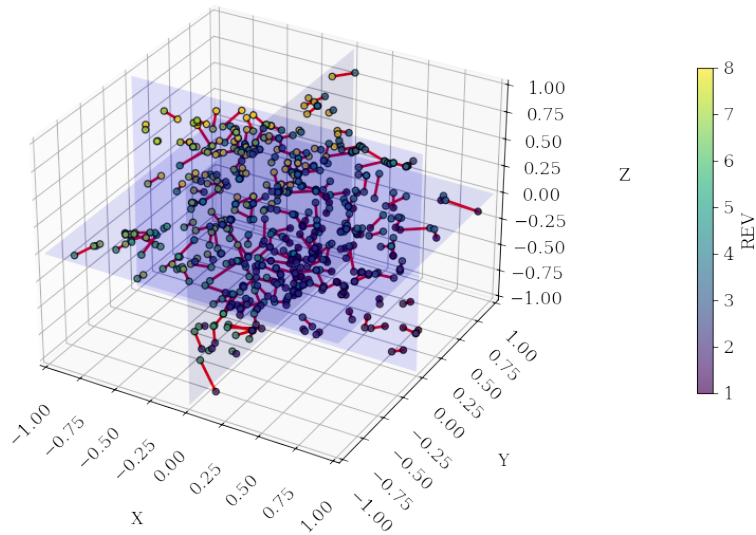
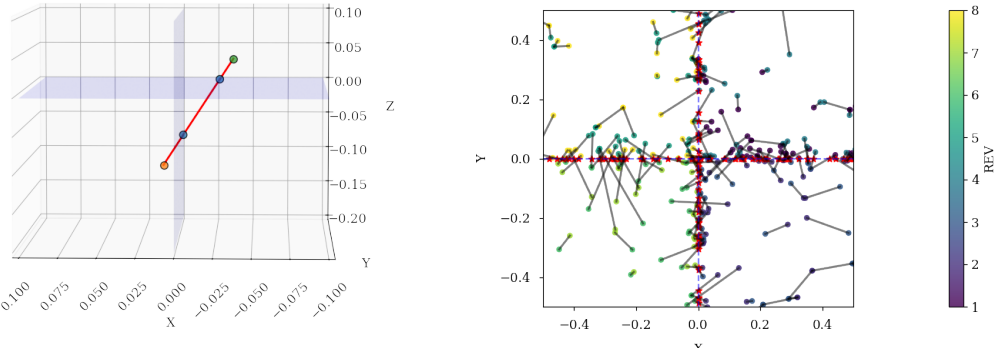


Figure 5.2: Edges that connect vertices belonging to different REVs.

To deal with this struggle we have two options. The first one is to just remove this type of edge, since we are considering an approximated approach to compute the parameters. This would be a valuable option, but it could cause some problems when dealing with boundary conditions. To assign them, we need to identify the vertices that exist within a specific distance from the boundary. Removing these edges could then lead to unphysical boundaries since the length of this kind of edge is not known a priori: we could both erase a small edge maintaining a close distance to the boundary facet, or a much longer one, deleting in this way a possible boundary point. This kind of approach could then cause significant changes in the structure of the vascular network.

A much safer option is to compute the intersections between each edge and the planes that identify the partition of the domain. In this way, we create a boundary node that belongs to the intersection facet and divide the edge into segments corresponding to the number of subregions it crosses. The previous lists that identify the nodes and edges of the vascular network are updated with these new points and the segmentation of the edges. Moreover, each intersection is labeled using the index "0", to discern this kind of point between the real vertices of the vascular network. Figure 5.3a shows an example of this computation where the orange point represents the origin of the edge, the green one the final, and the blue one the computed intersections. Furthermore, the results of an example of the iteration process on all selected edges can be seen in Figure 5.3b, where we present a 2D visualization over the plane  $XY$  for better visualization.



(a) 3D plot of the intersections calculated between a single edge and the subdivision planes.

(b) 2D snapshots result of the application of the process of finding the intersections with planes.

**Figure 5.3:** Examples of the results of the intersection algorithm.

After this step, we obtained a mask over the points that identify the belonging of each one of them to a specific REV, by using as markers the REV's numbering, or their nature as

intersections points, with marker "0". Moreover, the edges are of three types, depending on the kind of nodes they are connecting, namely:

- two vertices belonging to the same REV;
- a vertex of a REV and an intersection point;
- two intersection points.

For each REV we are going to select only the first two types since the connection between two intersection points can be considered as a spurious branch, not feasible for the approximation of the parameters. In the end, we create an algorithm to divide the domain into the chosen number of REV, partitioning the edges to obtain a clean segmentation of the vascular network.

The final step is to post-process the selected edges to omit all the unfeasible branches that could result after the segmentation. This is important because the final aim of this part is to obtain the appropriate vascular subnets of each REV that will be used to compute the effective parameters of our problem. So, the net has to represent a real vascular network, without spurious edges or unrealistic ones.

The postprocessing process also depends on the boundary conditions we will use. In fact, after the division process, we have to reassign the inlet and outlet labels to each subnet. For each of the three directions, we consider the two faces of the subdomain whose normal is aligned with the chosen direction. One of the facets will be considered as the inlet and the other as the outlet. Accordingly, the points that have the smallest geometric distance, up to a tolerance, from the inlet face are considered inlet points. The outlet points are found similarly, and we define a list of labels for the specific REV.

To guarantee a feasible network, we exploit the **Python** library **networkx**, which is a powerful tool for managing graphs. Through this, we are able to find all the connected components of the net and select the one of major dimensions in terms of vertices and edges. In this way, we ensure that the final subnet has feasible pathways for the flows from the inlet face to the outlet face, omitting all the minor independent sets of branches that can arise after the division process. In addition to that, other specific cases have to be considered. For example, the segmentation process generates some branches that start from one of the other faces that are neither the input nor the outlet. As explained in 3.2 these types of connection are not feasible since we are going to set boundary conditions of Dirichlet type for the outlet and inlet faces and no flow type for the other faces for the pressure simulation. For this reason, having branches with only the outlet fixed will raise an error in the calculation. Moreover, changing the direction of the computation results in a different distribution of the input and outlet faces. Therefore, this postprocessing step

has to be made for each one of the directions, with the result of three different submeshes referred to the same REV.

After completion of the post-processing step, the actual generation of meshes necessary for the simulation can be performed. We decided to use the tools from the `dolfin` package to create each REV mesh, starting from the selected points and processed edges. In addition to that, a list containing the radii of the edges and one creating the labels of each vertex is created. An example of a resulting REV submesh can be seen in Figure 5.4.

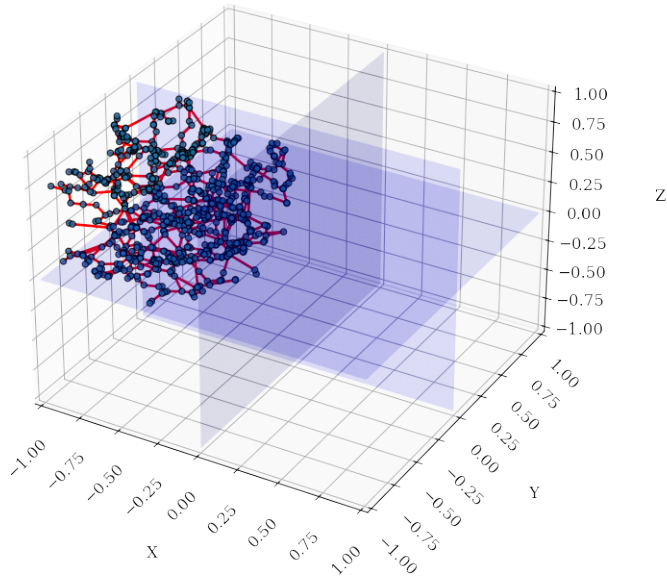


Figure 5.4: Example of a submesh of the original vascular network, obtained with the division process.

### 5.1.2. Upscaling Strategy

In the previous section, we detail the implementation of the algorithm that partitions the vascular network, obtaining the submeshes useful for the computation of the upscaled parameters.

As specified in Section 3.2, after gathering all the information about each REV, the computation of the parameters is pretty straightforward, as it is a matter of application of the given formulas. For what concerns the calculation of  $\mu_{bl}^{up}$ , it is necessary to have at disposal the list of edges and radii belonging to each REV and substitute them in Equation 3.7, while for the calculation of the term  $\gamma$  (Equation 3.16) for the right-hand side, the geometric information about the REV is sufficient. At the end of the computation, we

have a scalar value of the upscaled viscosity and the Starling filtration law term for each REV of the domain.

Instead, there are many aspects to consider when it comes to the permeability tensor  $K^{up}$ . As stated in Equation 3.9, the calculation of each component depends on the volume flux established between an input and an outlet face, imposing a negative pressure drop. To do this, blood flow is simulated in the REV vascular network, imposing Dirichlet boundary conditions on the inlet and outlet facets, and no-flow boundary conditions on the remaining ones. The goal is to approximate the behavior of the pressure in each direction for each REV. To this end, the linear system presented in 3.12 is implemented and solved. Since we are dealing with Dirichlet boundary conditions, the pressure is given at the inlet and outlet nodes. For this reason, the implemented matrix is a reduced version of the original, since the rows and columns referring to the boundary nodes are set to 0 and deleted from the system. Furthermore, the inlet and outlet pressure values are added in the source term of the equation to refer to the nodes that are connected to these boundary nodes. The system is solved using the Python package `linalg`, which provides a suitable solver depending on the characteristics of the matrix, and as a result, we obtained the pressure approximation in each node.

After that, the components of  $K^{up}$  can be computed. In fact, the pressure gradient in the outlet volume flux formula 3.8 can be approximated by discretizing using finite difference, namely for each direction:

$$\frac{\partial p^V}{\partial s} = \frac{p_{\text{prev}}^V - p_{\text{outlet}}^V}{|\mathbf{x}_{\text{prev}} - \mathbf{x}_{\text{outlet}}|} \quad (5.1)$$

where we compute the difference between the pressure for every outlet point and the one at the other vertices of the edge that connect with the outlet, scaled by the edge's length. Finally, all the computed variables can be substituted in 3.9 to compute the tensor component. A pseudo-code that summarizes the main steps from the REV division process to the computing of the upscaled variables can be seen in Algorithm 5.2.

---

**Algorithm 5.2** Computation of the Upscaled Parameters

---

```

1: Input: coordinates, edges, radii, labels, n_div_x, n_div_y, n_div_z
2:  $nREV = n\_div\_x * n\_div\_y * n\_div\_z$ 
3: REV_division( $n\_div\_x, n\_div\_y, n\_div\_z$ )
4: Find_intersection(coordinates, edges)
5: for direction in  $[x, y, z]$  do
6:   for REV in np.arange(nREV) do
7:     Identify coordinates and edges for REV
8:     Post-processing edges
9:     Find the major connected component
10:    Find inlet and outlet nodes
11:    Create labels
12:    Identify radii
13:    Create_mesh( $coord_{REV}, edges_{REV}, labels_{REV}, radii_{REV}$ )
14:    Compute_ $[\mu_{bl}^{up}]_{REV}$ 
15:    Compute_ $\gamma_{REV}$ 
16:    Compute_pressure
17:    Compute_ $VF_{direction,REV}$ 
18:    Compute_ $[K^{up}]_{direction,REV}$ 
19:  end for
20: end for
21: Return:  $K^{up}$ ,  $\mu_{bl}^{up}$ ,  $\gamma$ 

```

---

## 5.2. Solver for the Homogenized Models

In the previous section, we presented the implementation of the algorithm used to compute the effective parameters. In this way, we were able to summarize the features of the vascular network, obtaining some variables that are meaningful and feasible for this approximation. We started from a microscale level and obtained macroscale parameters that can be suitably used for solving the whole problem.

As shown in Chapter 4, the discretization of both the full-pressure model 3.15 and the mixed model, 3.17-3.18, is made by using the Finite Element Method (FEM). To solve the problem it is sufficient to assemble the block matrices and solve the linear system using proper methods. To do this, we exploit the Python libraries `fenics`, `cbc.block` and `PETSc`. In particular, `fenics` is a powerful Python library for solving partial differential equations (PDEs) numerically since it provides a high-level interface to define and solve

various types of problem. This library provides FEM methods and employs symbolic mathematics to automatically generate efficient finite element code. Moreover, the packages `cbc.block` and `PETSc` are very useful for both managing and implementing block matrices and solving linear systems. In the following, we detailed the implementation for both the primal and the mixed formulations.

### 5.2.1. Primal Pressure Model

In order to solve the homogenized model in the primal-pressure formulation, we first have to define a mesh suitable for the simulation, then accordingly implement the matrices reported in 4.16, and finally solve the system.

For what concerns the mesh creation, further details are given in Chapter 6, where we present the test cases with the different geometries. However, the reasoning behind the generation of meshes involves the fact that we have to approximate both the pressure in the capillary and the tissue. Furthermore, since the vascular network is homogenized, we do not need a mesh for the vascular domain. Instead, we consider both the capillary bed and the tissue as 3D porous mediums. For this reason, we consider the same mesh for both variables, supposing to have taken a vascular network completely embedded in a cubic tissue. Generally speaking, to create the triangulation we exploit some functions given from the `fenics` library, like `BoxMesh` that allows us to discretize a cubic geometry domain with a given size. Moreover, for more complex geometries, the Delaunay algorithm [25] can be used. This last algorithm is a computational geometry technique that creates a triangulation of a set of points in a plane by constructing triangles such that no point in the set is contained near any triangle formed by the points. This property ensures that the resulting triangulation is well-shaped and avoids skinny or degenerate triangles.

Both these techniques give as a result a `dolfin` mesh with specific labels depending on the boundary conditions.

The next step is the implementation of the block matrices necessary to solve the system. As specified in 4 we choose  $P^1$  elements to approximate both capillary and tissue pressure. After that, in Section 4.1.2 we present the matrices containing the basis function of the chosen spaces. The `fenics` environment instead requests as input a previous theoretical step. In fact, after the definition of suitable spaces, the block matrices of the linear system and the right-hand side term have to construct with the bilinear form of the variational formulation of the problem, namely:

$$A = \begin{bmatrix} \rho_{bl} \left( \frac{K^{up}}{\mu_{bl}^{up}} \nabla p^{cap}, \nabla q^{cap} \right)_{\Omega} & 0 \\ 0 & K^T (\nabla p^t, \nabla q^t)_{\Omega} + \beta(p^t, q^t)_{\partial\Omega} \end{bmatrix}$$

$$M = \begin{bmatrix} \gamma(p^{cap}, q^{cap})_{\Omega} & -\gamma(p^t, q^{cap})_{\Omega} \\ -\gamma(p^{cap}, q^t)_{\Omega} & \gamma(p^t, q^t)_{\Omega} \end{bmatrix}$$

$$L = \begin{bmatrix} \gamma(\pi_p - \pi_{int}, q^{cap})_{\Omega} \\ -\gamma(\pi_p - \pi_{int}, q^t)_{\Omega} + \beta(p^0, q^t)_{\partial\Omega} \end{bmatrix}$$

with all the trial and test functions defined accordingly with the chosen function space. Furthermore, the parameters  $K^{up}$ ,  $\gamma$ ,  $\mu_{bl}^{up}$  are those computed in the previous section. Since they assume different values depending on the geometrical position of the domain, we exploit the `fenics` tool `UserExpression` to create space-dependent functions that, during the computation, assign the correct value of the effective parameters to the nodes, depending on which REV they belong to. To assemble the bilinear forms as block matrices, we exploit the `block_assemble()` function of the `cbc.block` package.

Finally, the following system 5.2 can be solved.

$$T\mathbf{p} = \mathbf{L}, \quad (5.2)$$

where  $T = A + M$  and  $\mathbf{p} = [p^{cap}, p^t]$ . In particular, both obtained variables are block vectors, collecting the pressure approximation in the nodes of the mesh.

Regarding the boundary conditions, we strongly impose them using `block_bc` function. In particular, for the capillary pressure, Dirichlet boundary conditions for the inlet and outlet are defined.

To solve this problem, we exploit the `petsc4py` package that allows conversion from the matrix format that arises after the block assembly to a more suitable for numerical simulations. Moreover, it provides several solvers and preconditioners that can be used to increase convergence. In particular, we used Generalized Minimal Residual Method (GMRES), which is an iterative numerical method used to solve large systems of linear equations. Furthermore, we exploit the ILU preconditioner, which is a suitable choice for solving large sparse linear systems, such as those arising from the finite element method, and it is often coupled with the GMRES method.

### 5.2.2. Mixed Model

Regarding the implementation of the mixed formulation of the homogenized problem, the same process as before is followed. Indeed, the computational domain remains the same as the primal-pressure case, namely, a cubic domain in which we approximate the pressure and velocity for both the tissue and the capillary bed. The main difference from

the previous case is in the assembly of the block matrix. Here, we chose Taylor-Hood elements  $P_2 - P_1$ , which is a stable couple that is often used to approximate velocity and pressure. Moreover, in this formulation, we have the inverse of the upscaled parameter for the permeability tensor. Luckily, as we detailed in 3.2, this tensor is diagonal, so the computation of the inverse is straightforward, as we considered the tensor with the reciprocal components. To impose the correct value of these variables, we exploit a `UserExpression` function as before. In the following, we define the matrices used for the assembly of the problem.

$$T = \begin{bmatrix} \frac{1}{\rho_{bl}} \left( \left[ \frac{K^{up}}{\mu_{bl}^{up}} \right]^{-1} \mathbf{u}^{cap}, \mathbf{v}^{cap} \right)_{\Omega} & 0 & -(p^{cap}, \nabla \cdot \mathbf{v}^{cap})_{\Omega} + (p_{cap}, \mathbf{v}^{cap} \cdot \mathbf{n})_{\partial\Omega} & 0 \\ 0 & \frac{1}{K^T} (\mathbf{u}^t, \mathbf{v}^t)_{\Omega} & 0 & (\nabla p^t, \mathbf{v}^t)_{\Omega} \\ -(\nabla \cdot \mathbf{u}^{cap}, q^{cap})_{\Omega} & 0 & -\gamma(p^{cap}, q^{cap})_{\Omega} & \gamma(p^t, q^{cap})_{\Omega} \\ 0 & (\mathbf{u}^t, \nabla q^t)_{\Omega} & \gamma(p^{cap}, q^t)_{\Omega} & -\gamma(p^t, q^t)_{\Omega} - \beta(p^t, q^t)_{\partial\Omega} \end{bmatrix}$$

$$L = \begin{bmatrix} 0 \\ 0 \\ -\gamma(\pi_p - \pi_{int}, q^{cap})_{\Omega} \\ \gamma(\pi_p - \pi_{int}, q^t)_{\Omega} - \beta(p^0, q^t)_{\partial\Omega} \end{bmatrix}$$

As in the previous case, the test and trial functions have been defined accordingly for both the velocity and pressure spaces. In the end, the solution is obtained by solving  $T\mathbf{s} = \mathbf{L}$ , where  $\mathbf{s} = [u^{cap}, u^t, p^{cap}, p^t]$ . The variables obtained are block vectors, which collect the velocity and pressure approximation in the nodes of the mesh. It is worth noticing that, as mentioned in Chapter 4, in this case,  $T$  is no longer symmetric. In fact, to assemble the matrices using `fenics`, it is preferable to adjust the velocity on the boundary, rather than choosing a space that matches the one required by the theory. Even in this case, we used GMRES coupled with ILU, which is suitable also for non-symmetric systems, as the numerical method for solving the system. Boundary conditions of the Dirichlet type are imposed for the capillary pressure.

The following section presents the test cases used to study these models.

# 6 | Analysis of Perfusion in the Tumor Microvasculature

In this chapter, we report the results of applying the homogenization approach to a coupled problem, where the vascular network is completely embedded in the tissue, like, for example, a capillary bed. After homogenization, the vascular network can be considered a 3D porous medium and therefore modeled using the Darcy law. The homogenized problem requests the computation of the upscaled parameters that can relate the microscale structure of the vascular network to the macroscale structure of the porous medium. Then we solve the problem, approximating the capillary and tissue pressure, and for specific cases also the velocity.

Our approach was tested to three different cases, in increased order of complexity. At first, a benchmark case was considered, where we used a synthetic 1D vascular network. After applying the REV division process, we tested both the approximation of the full-pressure problem and the mixed one, recovering the pressure and velocity behavior for both the tissue and the capillaries.

Then, we test the primal pressure homogenized model using a real vascular structure mesh in a mouse's cancer brain, which was obtained by the REANIMATE project [6], [27]. This type of mesh has been used in several investigations, even with other homogenization approaches. The main difference is that our approach uses an anisotropic permeability tensor that gives us more detailed information about the perfusion in the vascular network. Moreover, in this case, the boundary condition had to be thought in a different way, in order to recover as much as possible a realistic behavior.

## 6.1. Synthetic Vascular Network Analysis

### 6.1.1. Generation of the Vascular Network

As a benchmark case, a synthetic vascular network generated in a  $2 \times 2 \times 2\text{mm}^3$  cube domain is used through an algorithm developed by Dr. Nunzio Dimola, which collaborates with the MOX department of Politecnico di Milano.

The core of this algorithm is the use of Voronoi 3D tessellations and the Dijkstra algorithm to obtain a 1D connected graph representing a feasible vascular network. The main steps of this algorithm can be summarized in the following:

- Partitioning of the domain in layers of varying size;
- Definition of cloud points of different density;
- Graph creation using Voronoi 3D and some post-processing;
- Definition of planes for inlet and outlet points and labelling process;
- Application of Dijkstra algorithm.

The first step is the partitioning of the domain. To create heterogeneous realistic complex nets, the cube is initially divided into three layers. In each one of them, a cloud of points with different given densities is generated. This gives flexibility in the generation of the vascular network, since the user can decide the better setting that resembles most of the features requested. After that, the entire point cloud is considered as the seed for the Voronoi tessellation algorithm. In Figure 6.1, an example is reported in which an increasing density of points was chosen from the first layer to the last.

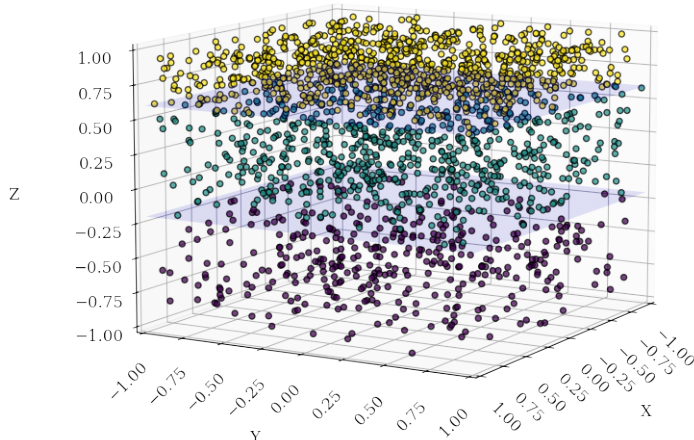
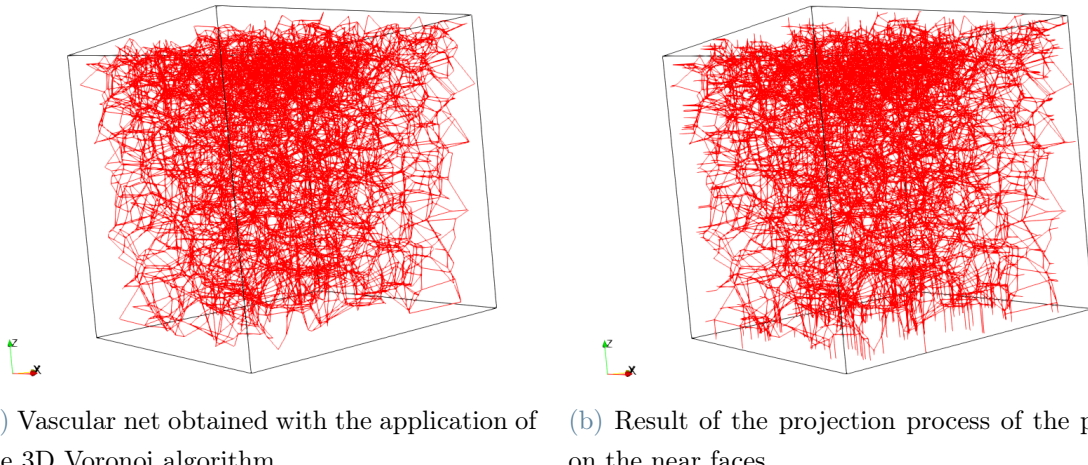


Figure 6.1: Example of a point cloud to give as input to the 3D Voronoi tessellations algorithm.

The following step is applying the 3D Voronoi algorithm starting from these points. After some post-processing, such as removing unfeasible branches, this process produces a network structure similar to the one in real-case scenarios. Consequently, the points on the obtained structure must be labeled to identify the inlet, outlet, and interior points. To do this, the domain is slightly enlarged by adding some planes at a chosen small distance from each face of the cube. Then the points that result geometrically near the planes were projected on them, and the segments obtained were added as straight edges to the mesh. In this way, it is easy to identify as inlet and outlet points the projected points on the planes. The results of this step are reported in Figure 6.2.



(a) Vascular net obtained with the application of the 3D Voronoi algorithm. (b) Result of the projection process of the points on the near faces.

Figure 6.2: Examples of the creation process of a synthetic vascular network.

Therefore the obtained points can be accordingly labeled, depending on the number of inlet and outlet faces that are chosen by the user. Finally, to recover a tree-like structure and to guarantee feasible paths between inlet and outlet faces, the Dijkstra algorithm is applied. Starting from a selected number of points chosen among the inlet set, the algorithm is called to find the shortest path from each of the points to one or multiple chosen outlet points. These paths are then progressively saved in a structure that gives the origin of the final vascular network. The last step is to save the mesh obtained in a format suitable for the simulation. The final result can be seen in Figure 6.3.

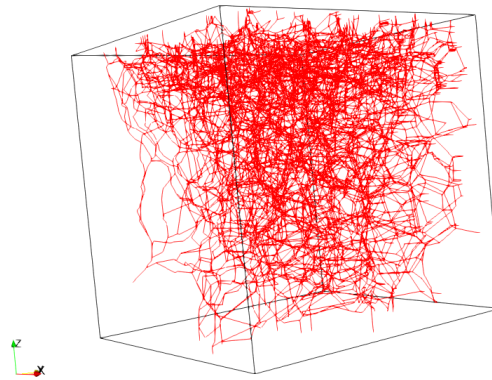


Figure 6.3: Final vascular net obtained after the application of Dijkstra algorithm.

### 6.1.2. REV Division

The vascular net that we used for the simulation was generated using the technique explained in 6.1.1. In particular, we recreate an intricate capillary bed embedded in a cube of tissue by setting a high density of points, and we selected 3 faces as the inlet ones and the other three as the outlet ones. Moreover, to reassemble the characteristics of a real vascular network, we assign each edge a radius, randomly choosing a value between  $5 \mu\text{m}$  and  $12\mu\text{m}$ , which are admissible values for capillaries. The final mesh can be visualized in Figure 6.4 and its features are listed in Table 6.1.

No. of nodes	5556
No. of edges	6254
No. of inlet points	165
No. of outlet points	165
No. of interior points	5226
Outlet points label	999
Inlet points label	111
Interior points label	555

Table 6.1: Mesh specifics of synthetic vascular net

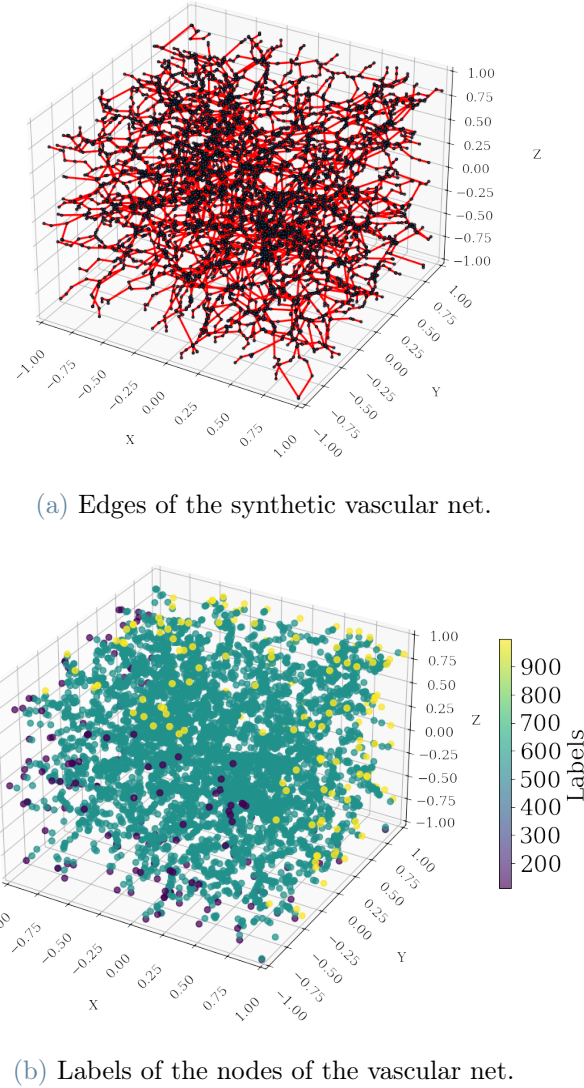


Figure 6.4: Visualization of the edges and labeled nodes of the synthetic vascular network.

In this section, we present the results of the application of the REV division algorithm presented in Section 5.1.1 applied to the vascular network described above. Through this process, we obtain the upscaled parameters that are used in the simulation of the homogenized model.

At first, we had to choose an appropriate number of REVs, therefore, selecting the REV's size. To do this, we conducted a sensitivity analysis on the number of points selected as input and output of each of the subregions. In particular, it was our interest to check that the ratio between the boundary points and the total number of the mesh was comparable to that of the initial mesh. In this way, we ensure that the sub-meshes obtained with the algorithm could still represent a feasible vascular network.

Therefore, we tested several decompositions of the domain, and for each direction and

each REV, we computed the average of the ratio between the REV's boundary points and the total ones, namely:

$$R_{avg} = \frac{\sum_{i \in [x,y,z]} \sum_{j \in [1, \dots, nREV]} \frac{(n_{i,j}^{in} + n_{i,j}^{out})}{n_{i,j}^{tot}}}{3nREV} \quad (6.1)$$

where  $n_{i,j}^{in}$ ,  $n_{i,j}^{out}$  and  $n_{i,j}^{tot}$  are respectively the number of inlet, outlet and total points for the j-th REV in the i-th direction and  $nREV$  is the total number of REV. In Table 6.2 we report the results of this analysis considering  $nREV = [1, 4, 8, 16, 27, 64]$ , where  $nREV = 1$  represents the whole vascular network.

$nREV$	$R_{avg}$
1	0.059
4	0.116
8	0.137
12	0.156
18	0.170
27	0.187

Table 6.2: Values of  $R_{avg}$  computed with different number of REVs

We can state that even for a small number of divisions, the ratio is still greater than that of the initial vascular network. This is a reasonable result considering that the boundary points of the segmented parts are the intersection computed between the faces, so, in proportion, the number is higher than the one of the original network. Nevertheless, we still have to choose the division that is feasible  $R_{avg}$ . After this analysis, we choose to divide the domain into 8 parts. The reasoning behind this choice is that, for a vascular network of this size, we preferred to maintain a  $R_{avg}$  as similar as possible to the original one, namely the one for  $nREV = 1$ . Furthermore, we preferred  $nREV = 8$  over  $nREV = 4$  since their  $R_{avg}$  were very similar, so it was worth having a deeper segmentation to obtain a better description of the vascular network. The division of the domain can be seen in Figure 6.5.

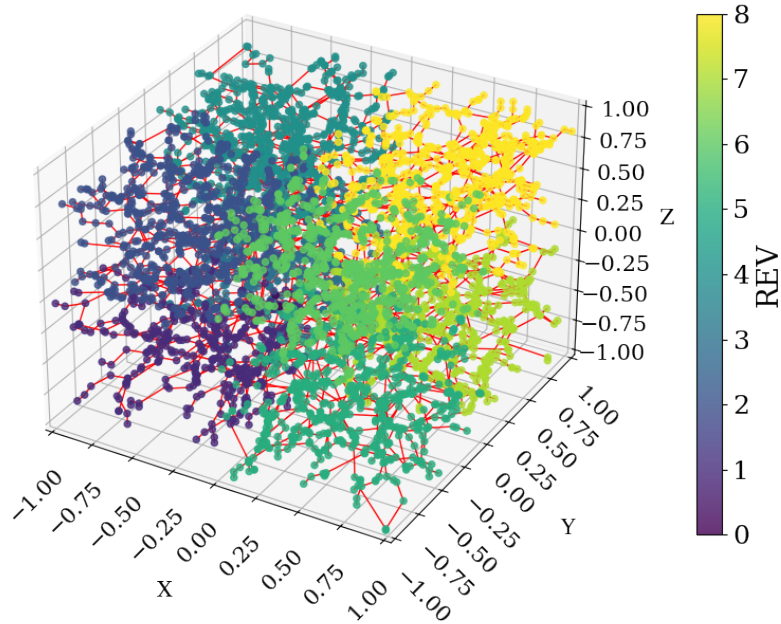
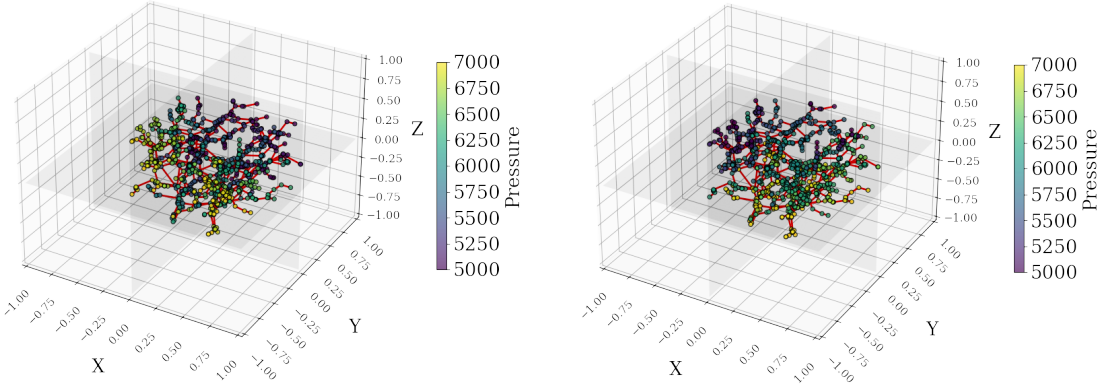
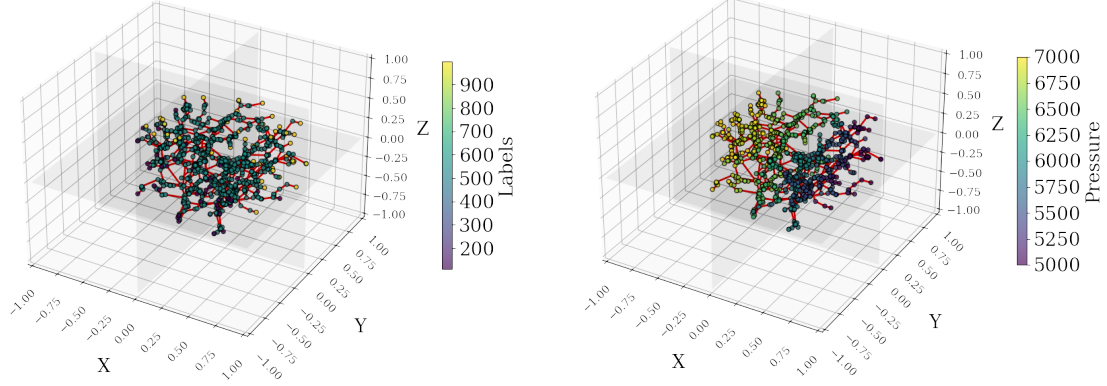


Figure 6.5: Segmentation of a cubic domain with an embedded synthetic vascular net in 8 REVs.

### 6.1.3. Upscaled Parameters

After the creation of the mesh for each REV, the next step is the computation of the upscaled parameters, namely  $K^{up}$ ,  $\mu_{bl}^{up}$  and  $\gamma$ , for each subdomain, as explained in 5.1.2. For the computation of the permeability tensor, simulation of the pressure behavior for each direction for each submesh is requested. This is necessary for the approximation of the volume flux and, consequently, is needed in the computation of the components of  $K^{up}$ . Here, we present the results regarding the behavior of the pressure's blood flow in each direction for just REV number 6 since very similar outputs were obtained for the other subdomains. For the simulation, we imposed a negative pressure drop, namely  $p_{inlet} = 7000Pa$  and  $p_{outlet} = 5000Pa$ . In Figure 6.6 the results are shown.



**Figure 6.6:** Submesh with labels and pressure approximation for directions  $[x, y, z]$ , of REV 6 of the cubic synthetic domain.

As we expected, since it is solved a diffusivity problem in one direction, the solution has a linear behavior.

Finally, in Figure 6.7 we present the results of the computed components of the permeability tensor  $K^{up}$  for each REV.

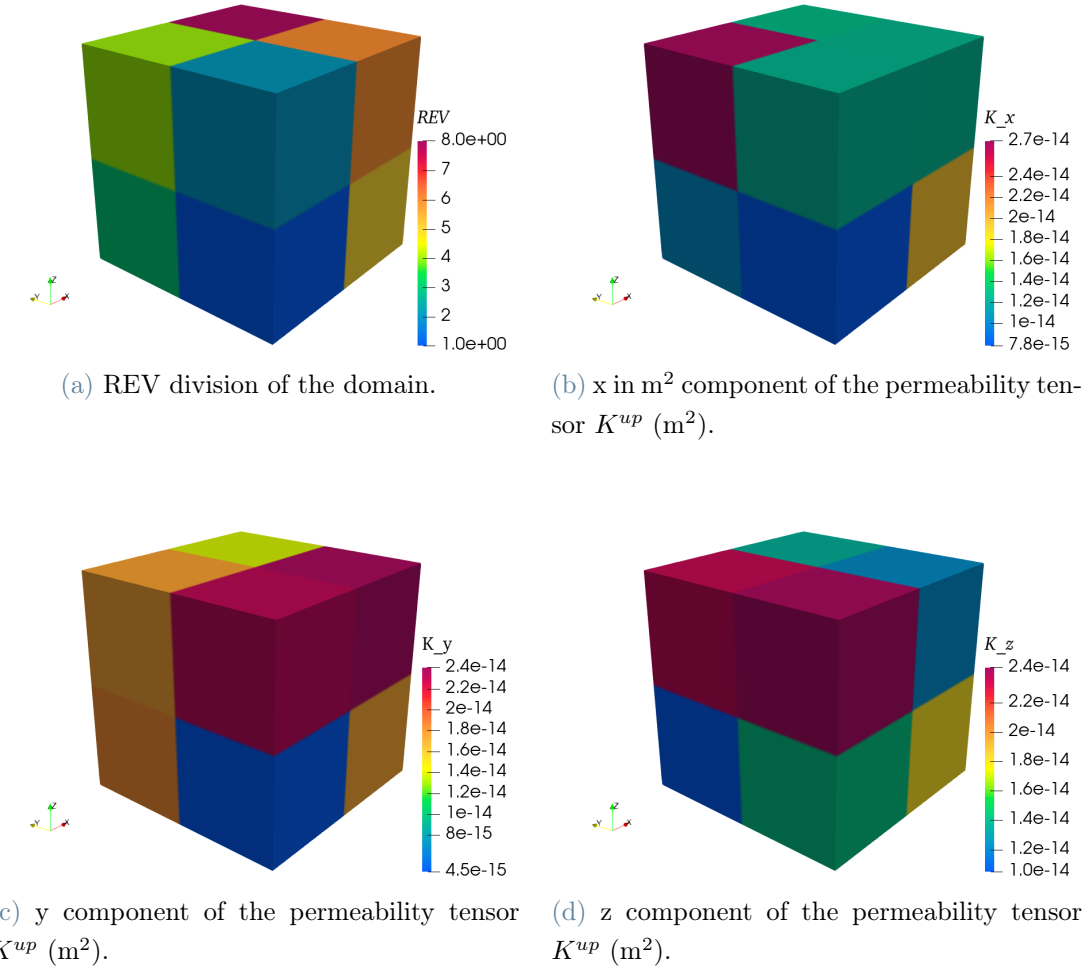


Figure 6.7: Components of the permeability tensor  $K^{up}$  for each REV of the cubic synthetic domain.

These results are coherent with [28] since the order of the tensors is  $\simeq 10^{-14}$ . Moreover, analyzing all the components the values are very similar. This is justified by the fact that the synthetic vascular network is equally complex in the whole space. Lastly, in Figure 6.8 are shown the results of the two scalar quantities, the averaged viscosity  $\mu_{bl}^{up}$  and the multiplying term of the Starling's filtration law, namely  $\gamma$ . As before, the values are coherent with the order of magnitude presented in the paper, namely  $\approx 10^{-3}$  for the viscosity and  $\approx 10^{-6}$  for the  $\gamma$ .

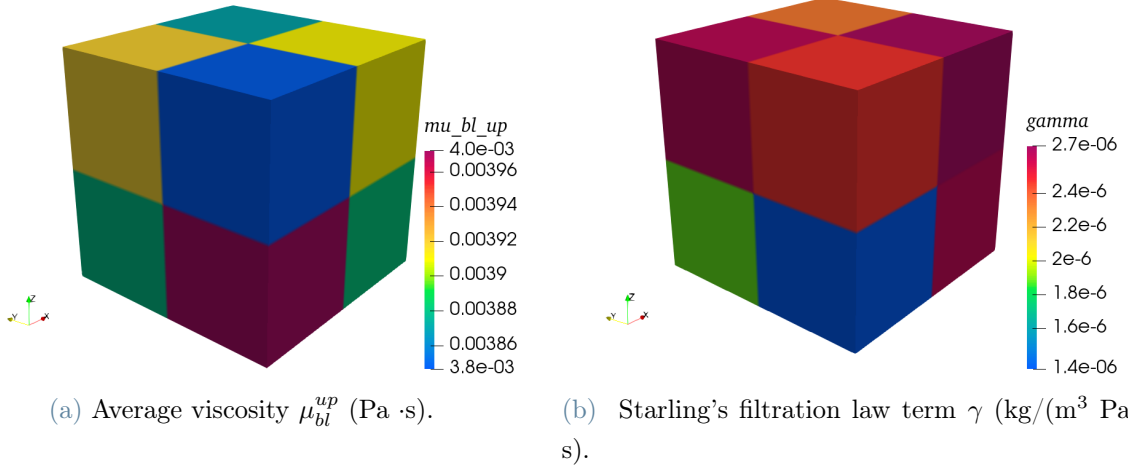


Figure 6.8: Values of  $\mu_{bl}^{up}$  and  $\gamma$  computed for each REV of the cubic synthetic domain.

#### 6.1.4. Primal Pressure Model

In this section, we expose the results of the full-pressure homogenized model, obtained by solving the linear system with the methodology described in 5.2.1. In particular, we approximate the behavior of the pressure in the homogenized capillary bed and in the tissue. For simulations, we define the values of the parameters as follows in Table 6.3.

Discharge hematocrit	$H$	0.45
Tissue permeability	$K_t$	$10^{-18} \text{ m}^2$
Interstitial fluid viscosity	$\mu_{int}$	$1.3 \cdot 10^{-3} \text{ Pa} \cdot \text{s}$
Plasma viscosity	$\mu_p$	$1.0 \cdot 10^{-3} \text{ Pa} \cdot \text{s}$
Blood viscosity	$\rho_{bl}$	$1030 \frac{\text{kg}}{\text{m}^3}$
Interstitial fluid density	$\rho_{int}$	$1000 \frac{\text{kg}}{\text{m}^3}$
Plasma oncotic pressure	$\pi_p$	3300 Pa
Interstitial oncotic pressure	$\pi_{int}$	666 Pa
Capillary wall hydraulic conductivity	$L_{cap}$	$10^{-12} \frac{\text{m}}{\text{Pa} \cdot \text{s}}$
Capillary radius for edge k	$R_k$	$5 - 12 \mu\text{m}$
Reference pressure	$p_0$	5000 Pa
Neuman parameter	$\beta$	0.001
Inlet Dirichlet value	$p_D^{in}$	7000 Pa
Outlet Dirichlet value	$p_D^{out}$	5000 Pa

Table 6.3: Values of the parameters of the Homogenized model

In this step, the computational domain is a cube of dimensions  $[-1, 1]^3$  mm<sup>3</sup>, which was discretized using a cubic mesh of points  $21 \times 21 \times 21$ , namely 9261 nodes and 48000 cells. Therefore, the nodes were labeled in order to identify the nodes belonging to the capillary model boundary and those of the tissue. Moreover, the domain was also marked to identify the REV division. We impose Dirichlet boundary conditions in the inlet and the outlet of the pressure model and Robin boundary conditions for the tissue. The mesh and the marked domain can be seen in Figure 6.9.

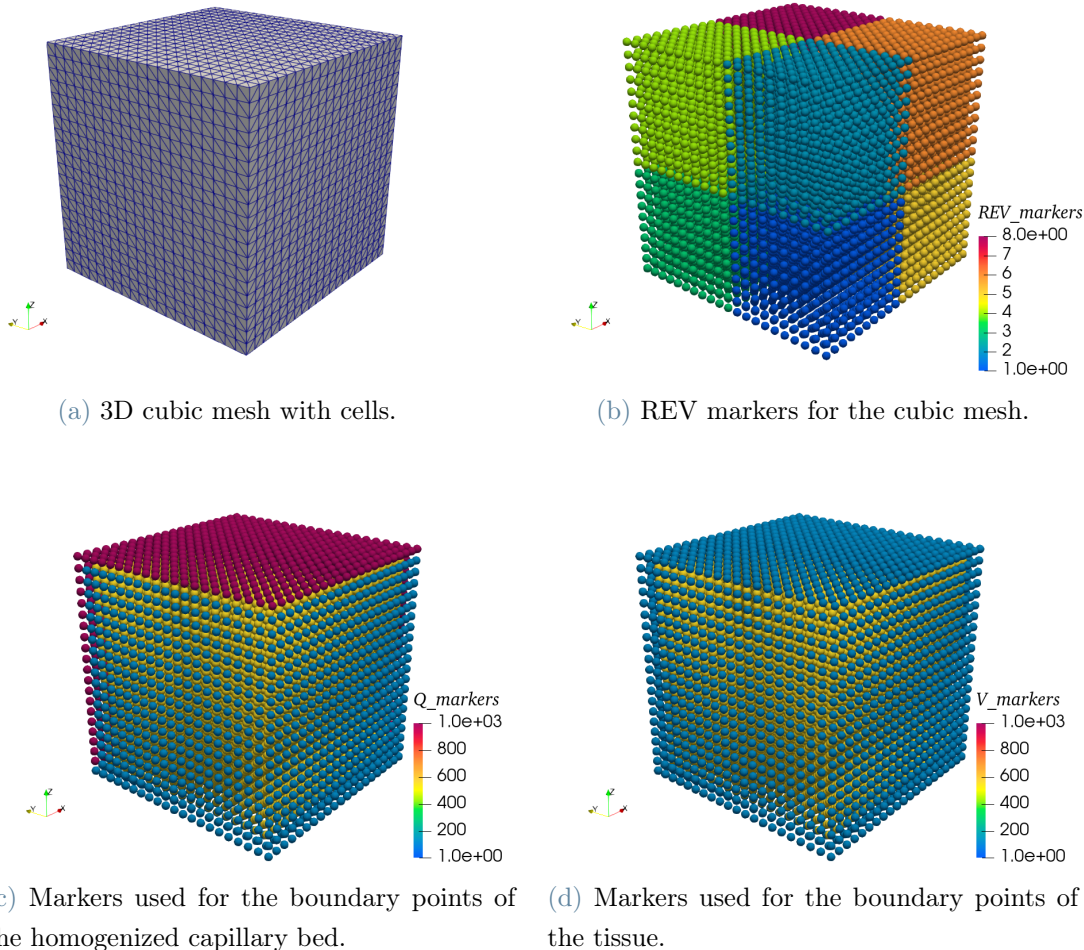
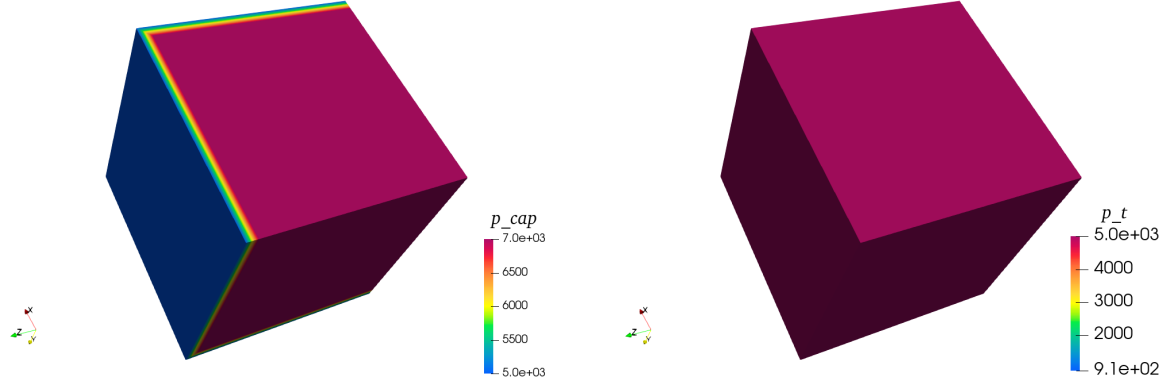


Figure 6.9: Plot of the mesh obtained from the cubic synthetic domain, with suitable markers used to label the boundary points and the REV points, necessary for the simulation of the pressure in the capillary and tissue of the homogenized model.

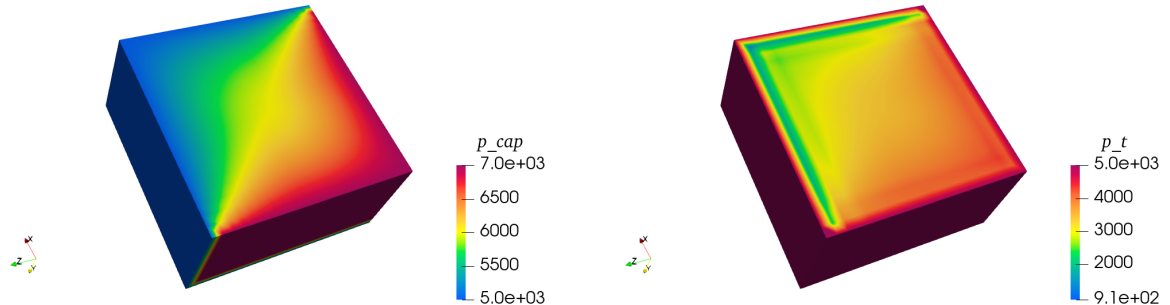
After that, we solve the problem using the GMRES method, using ILU preconditioner, imposing a tolerance of  $10^{-15}$  and 10000 as the maximum number of iterations. The method converged in 33 iterations, and the results of the pressure in the capillary bed

and in the tissue can be seen in Figure 6.10.



(a) Reconstruction of the capillary pressure (Pa) in a cubic domain, full view.

(b) Reconstruction of the tissue pressure (Pa) in a cubic domain, full view.



(c) Reconstruction of the capillary pressure (Pa) in a cubic domain, half view.

(d) Reconstruction of the tissue pressure (Pa) in a cubic domain, half view.

Figure 6.10: Results for the 3D-3D primal pressure coupled problem in a cubic synthetic domain.

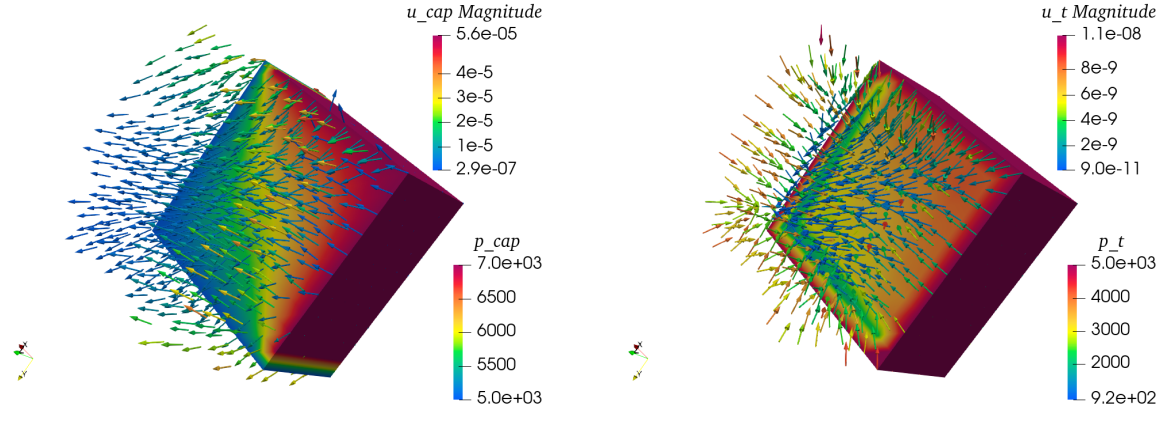
Regarding the pressure reconstruction in the capillary bed, one can observe that the pressure decreases almost linearly following the pressure drop imposed between the outlet and inlet faces. Moreover, it is highlighted that there is a rapid decrease in pressure in the intersection between the inlet and the outlet faces since the value on those faces is strongly imposed using Dirichlet boundary conditions, and the space to adapt is too small. A more refined mesh could solve this issue since the step between the two faces can be considered negligible. Furthermore, since the original vascular network was pretty homogeneous, the resulting permeability tensors are very similar between REVs, as we stated before. For this reason, the capillary pressure does not have critical changes from one REV to the other. Probably the use of a more complex and realistic network could

lead to more visible results.

Finally, we also obtained results for the pressure in the tissue. One can notice that there is also a feasible gradient that is influenced by the boundary conditions on the capillary bed. However, in this case, we used Robin on the tissue boundary, which is coherent since it models the variation of the pressure along the normal direction. In this case, we impose as a reference pressure  $p_0 = 5000$  Pa, to have coherence with the values of the capillary bed. Overall, the pressure value is lower than that of the capillaries, and this is feasible since the permeability of the homogenized capillary bed is higher, so there is less resistance in the blood flow. The tissue pressure has a significant drop in the correspondence of the outlet faces. This could be feasible thinking about the fact that in these faces the velocity of the blood flow is high since it is exiting the domain. Nevertheless, a further analysis regarding a more realistic case could highlight more significant results regarding this part. Moreover, a more refined mesh could also help in this case in understanding this critical behavior.

### 6.1.5. Mixed Model

In this section are detailed the results of the mixed formulation of the 3D-3D homogenized problem, presented in Section 3.4. In this case, it was possible to reconstruct the velocity and pressure for both the capillary bed and the tissue, using the strategy proposed in Section 5.2.2. The parameters used in the simulation are those presented in Table 6.3, to be consistent with the previous model. Nevertheless, we had to consider a more coarse mesh with respect to the one used before. In particular, we discretized a cubic domain cube of dimensions  $[-1, 1]^3$  mm<sup>3</sup> using a cubic mesh of points  $11 \times 11 \times 11$ , namely 1331 nodes and 6000 cells. This choice was made for computational cost reasons. Label division, both for REV and boundary points, and mesh structure are comparable to the one shown in Figure 6.9, but with the dimensions specified above. The problem is solved using GMRES, preconditioned with ILU, in 47 iterations, and the results can be seen in Figure 6.11. It is worth noticing, that the pressure results are coherent with the one reported in Figure 6.10, computed using the primal pressure problem, for both the capillary and the tissue. Moreover, the reconstructed velocities are feasible if compared to the reconstructed pressure. In fact, blood flow should follow the direction imposed by the negative pressure gradient, as it is modeled using Darcy's law. This behavior is observed both in capillaries and tissues, where blood flow occurs in the direction of the negative pressure gradient created between the inlet and outlet faces, even though the magnitude of the velocity is a little bit smaller than the one obtained in a real-case scenario. One thing to consider is that in this case, we made some approximations, for example in the



(a) Reconstruction of the capillary pressure (Pa) and velocity (m/s) in a cubic domain. (b) Reconstruction of the tissue pressure (Pa) and velocity (m/s) in a cubic domain.

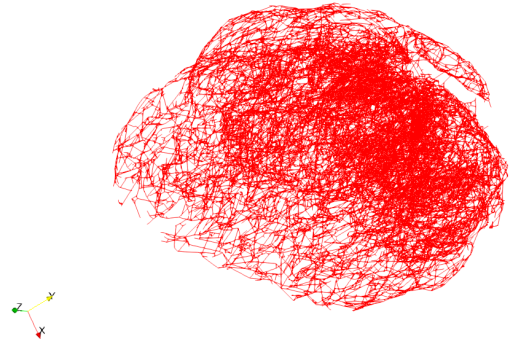
Figure 6.11: Results for the 3D-3D mixed coupled problem in a cubic synthetic domain, where the velocity and pressure of the blood flow have been reconstructed for the capillary bed and tissue.

generation and assignment of random radii to the edges, or in the computation of the upscaled parameter, that, when improved, could lead to more realistic results. Moreover, even in this case, further grid refinement could enhance the outcomes, particularly within the tissue.

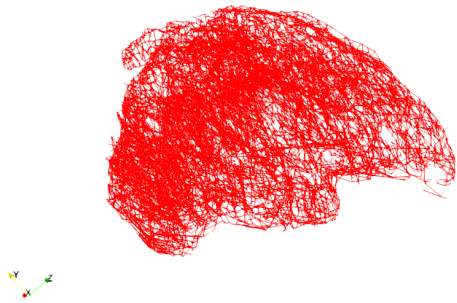
## 6.2. Mouse Tumor Vasculature in a Cube

### 6.2.1. Real-Case Cancer Geometry

In this section, we present the results obtained by applying our methodology to a more complex vascular network. In fact, we had at our disposal a mesh from the REANIMATE project that addresses the transport through tumors, blending mathematical models and high-resolution imaging data [6][27][13]. In particular, this geometry was obtained from imaging of a cancer grown in a mouse brain for 10-14 days. Then, by optical projection tomography, the data were imaged and then segmented to obtain a vascular network, with the same graph format discussed in 2.1. The obtained vascular network has 18093 nodes and 23949 edges and can be seen in Figure 6.12.



(a) Snapshots of the cancer mesh.



(b) Another point of view of the cancer mesh .

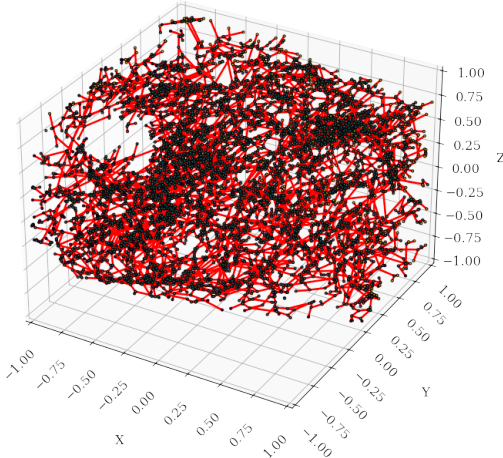
Figure 6.12: Different Snapshots of the mouse cancer geometry

### 6.2.2. REV Division

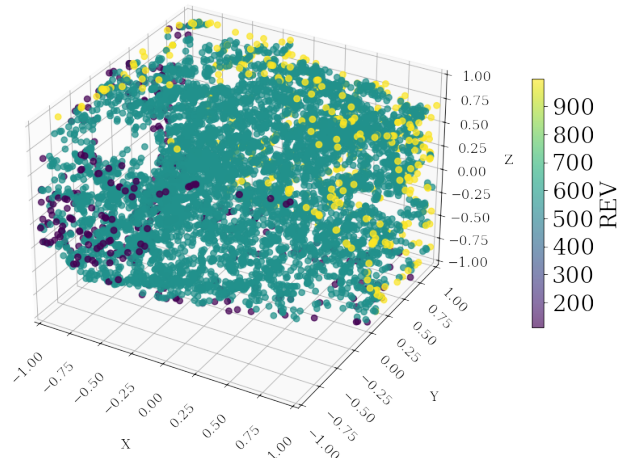
The first step is to try our approach on a smaller section of this net. After scaling the coordinates to fit a cube  $[-2,2]^3$ , we extract a cube of dimensions  $[-1,1]^3$ , approximately from the center of the cancer geometry. Moreover, we have at our disposal the physical radii for this geometry. However, they were associated with each bifurcation point instead of the edges. To recover the formulation coherent with our code we use an approximation, we identify the radii associated with the vertex of each edge, and we consider their average as the radius for that particular edge. The range of the final set of radii is between 15 and  $30 \mu\text{m}$ . As before, we set as boundary points the ones with a minor distance from the faces of the cube. In Figure 6.13 the final geometry for this cancer cube is shown, while in Table 6.4 the specifics of the vascular network are listed.

No. of nodes	6126
No. of edges	7407
No. of inlet points	342
No. of outlet points	481
No. of interior points	5303
Outlet points label	999
Inlet points label	111
Interior points label	555

Table 6.4: Mesh specifics of the cubic domain of the cancer vascular net



(a) Edges of the cancer cube vascular net.



(b) Labels of the nodes of the vascular net.

Figure 6.13: Visualization of the edges and labeled nodes of the cubic portion extracted for the cancer vascular network.

Regarding the REV division process for this type of mesh, we decided to use 8 as the REV number. This choice is consistent with the previous case, since the dimensions of the network are comparable. Moreover, computing the average ratio as before we had  $R_{avg} = 0.115$  for that cancer mesh and  $R_{avg} = 0.173$ , therefore, we consider  $nREV = 8$  a suitable choice. Figure 6.14 shows the result of the segmentation process, with respect to the nodes that belong to each REV.

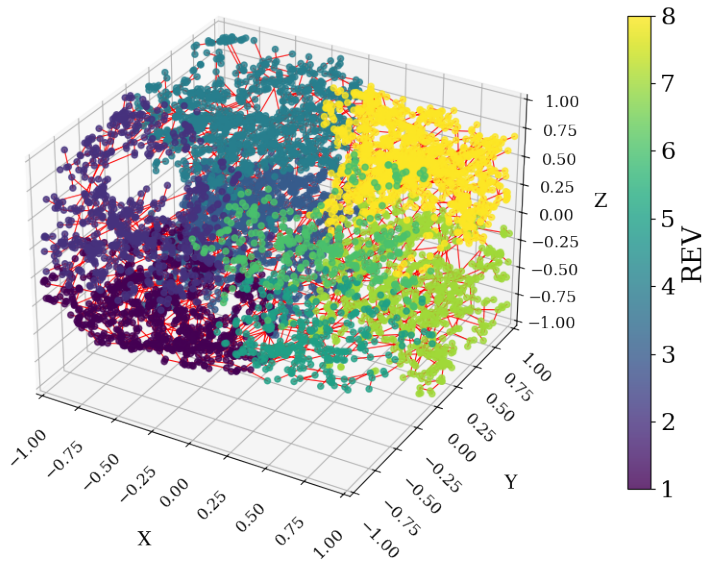
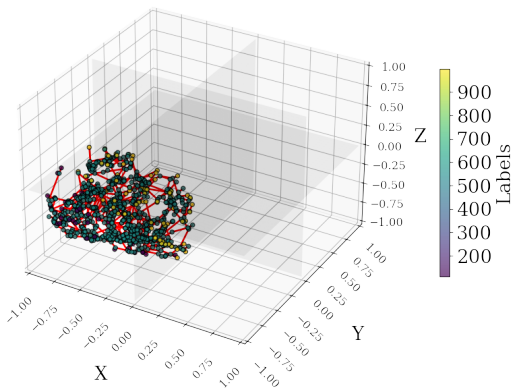


Figure 6.14: Segmentation of the cubic domain extracted from the cancer geometry in 8 REVs.

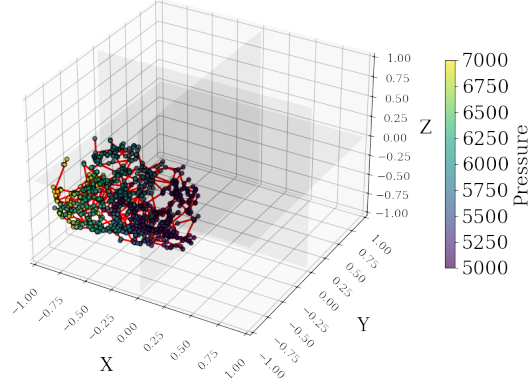
### 6.2.3. Upscaled Parameters

After the division process, the next step is the computation of the upscaled parameters, namely the permeability tensor  $K^{up}$ , the averaged blood viscosity  $\mu_{bl}^{up}$  and the parameter for the right and side of the model,  $\gamma$ . As before, the main aspect of this process is the approximation of the pressure blood flow in each direction in each REV, to obtain the parameters useful for the computation of the permeability tensor components. To obtain blood flow, a negative pressure drop was imposed on the input and outlet points for each direction, that is, we impose  $p_{inlet} = 7000$  Pa and  $p_{outlet} = 5000$  Pa for the selected faces, and no-flow boundary conditions for the remaining ones. In Figure 6.15, the results of

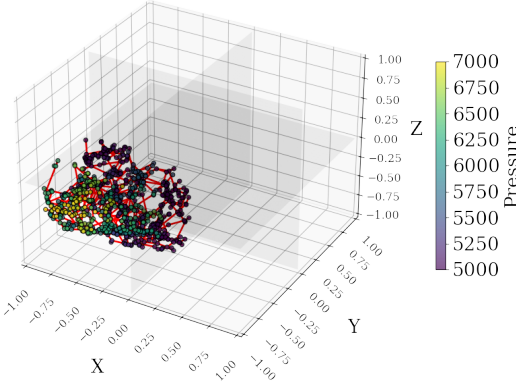
this approximation for REV 1 are shown.



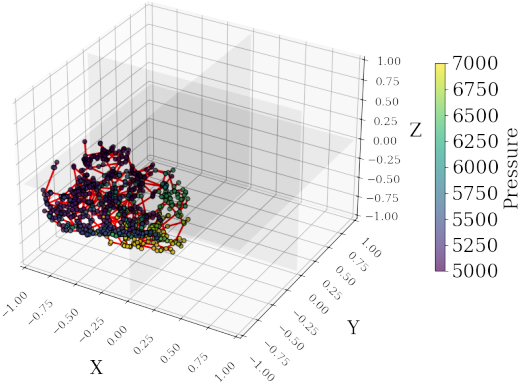
(a) Submesh for REV 1, with labels for boundary points.



(b) Pressure (Pa) behavior computed in REV 1 along the x-direction.



(c) Pressure (Pa) behavior computed in REV 1 along the y-direction.



(d) Pressure (Pa) behavior computed in REV 1 along the z-direction.

Figure 6.15: Submesh with labels and pressure approximation for directions  $[x, y, z]$ , of REV 1 of the cubic domain extracted from the cancer geometry.

Like for the previous case, the results are coherent with what we expected.

Finally, in Figure 6.16 we present the results of the components computed of the permeability tensor  $K^{up}$  for each REV. It is worth noticing that in this part we prefer a visualization using points instead of regions. This is motivated by the fact that, since the domain is not homogeneous as in the previous case and is very indented, the interpolation that was used before for the region visualization is not feasible for this case.

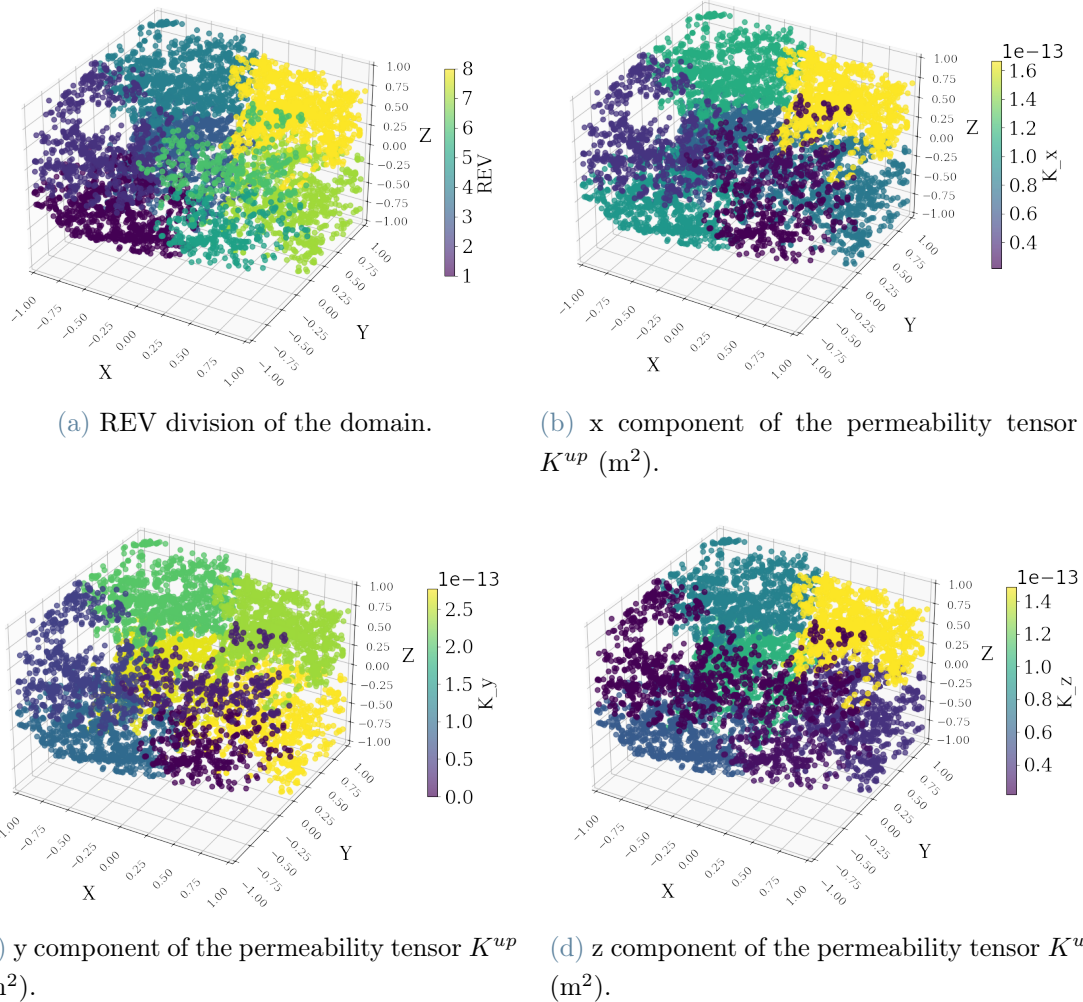


Figure 6.16: Components of the permeability tensor  $K^{up}$  for each REV of the cubic domain extracted from the cancer geometry.

Furthermore, as for the upscaled viscosity, one has to be careful of the fact that in the computation we used relations that are known nowadays for human vasculature. However, since updated formulas for the mouse vascular structure have not yet been formulated, we suppose that the behavior of the blood flow in this case can be approximated with the human one. In Figure 6.17 the results regarding the last two parameters.

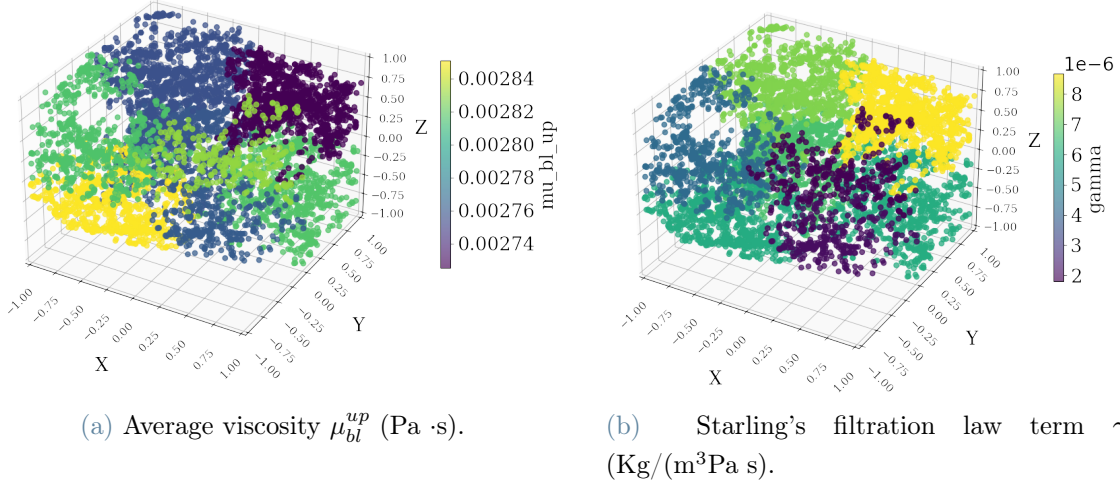


Figure 6.17: Values of  $\mu_{bl}^{up}$  and  $\gamma$  for each REV of the cubic domain extracted from the cancer geometry.

Even if the structure of the mesh is different than the one from the previous case, the overall values of the parameters are still very similar from one REV to the other. We can state that this has happened since the structure of the microvascular network is very similar and coherent for each REV. Moreover, the geometry is not sufficiently intricate to see proper changes.

#### 6.2.4. Primal Pressure Model

Finally, here we present the results obtained by solving the 3D-3D primal pressure model, using the cancer cube geometry. As in the previous case, we imposed the Dirichlet boundary conditions for the pressure in the capillaries and the Robin boundary conditions for the tissue pressure. Furthermore, the parameters used to solve this problem are similar to those in Table 6.3, with the difference in the radii that in this case were between 15-30  $\mu\text{m}$ .

As before, the advantage of using a homogenized approach is that the vascular networks can be considered as a 3D porous medium; therefore, for the computation the same mesh can be used for the approximation of both the capillary bed and the tissue models. For this test case, we cannot discretize the domain using the same strategy as before, since it is not a perfect cube, as it was the benchmark test. For this reason, we exploit the Delaunay triangulation that, from the given nodes of the vasculature, creates a mesh of tetrahedron element. The obtained mesh counted 6126 vertices and 38576 cells. Figure 6.18 shows the mesh and its relative marking for the different domains.

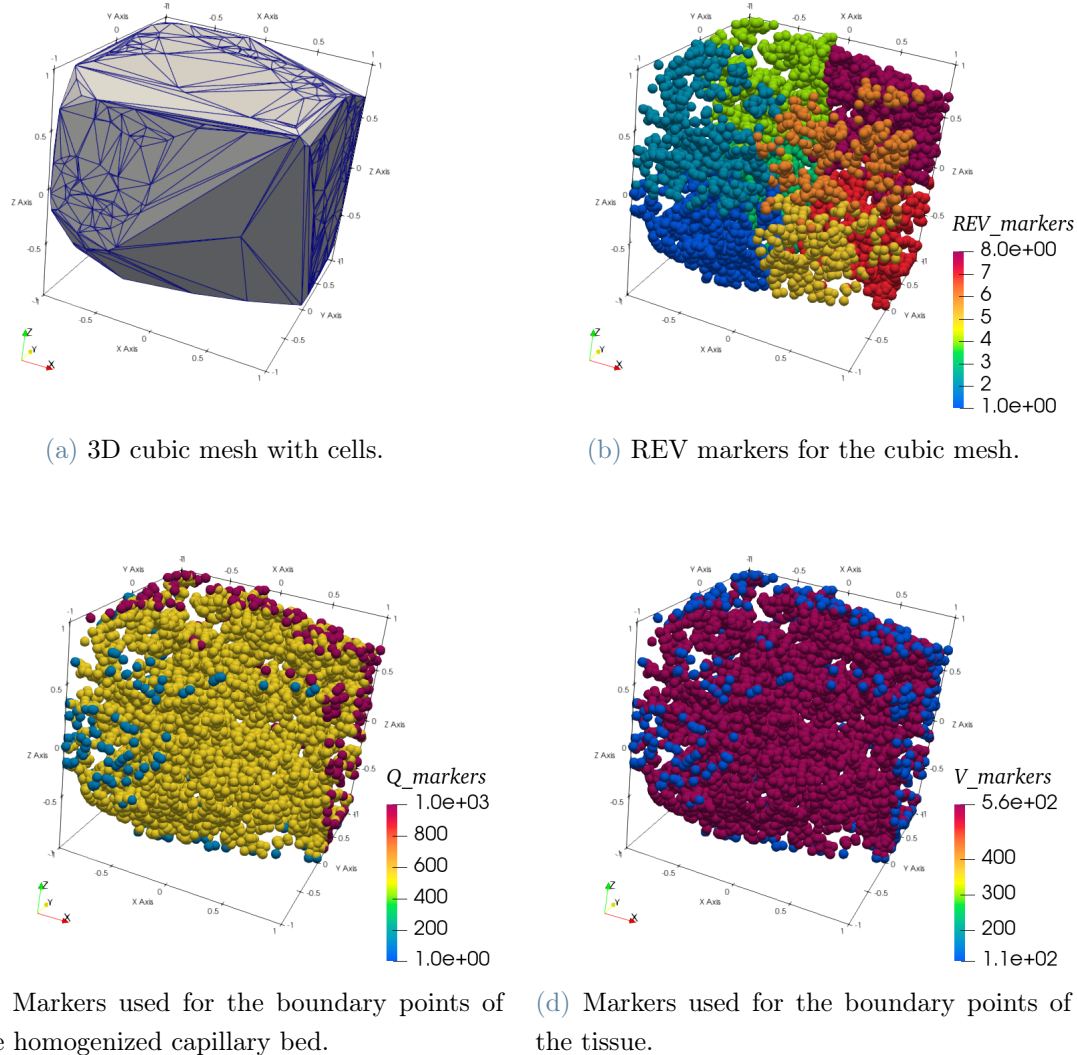


**Figure 6.18:** Plot of the mesh obtained from the cubic geometry extracted from the cancer domain, with suitable markers used to label the boundary points and the REV points, necessary for the simulation of the pressure in the capillary and tissue of the homogenized model.

Lastly, the problem is solved in the presented mesh, using the iterative method GMRES, with ILU as a preconditioner. As before the tolerance for the relative residual was set at  $10^{-15}$  and the maximum number of iterations at 10000. The method converged in 43 iterations, and the results can be seen in Figure 6.19.

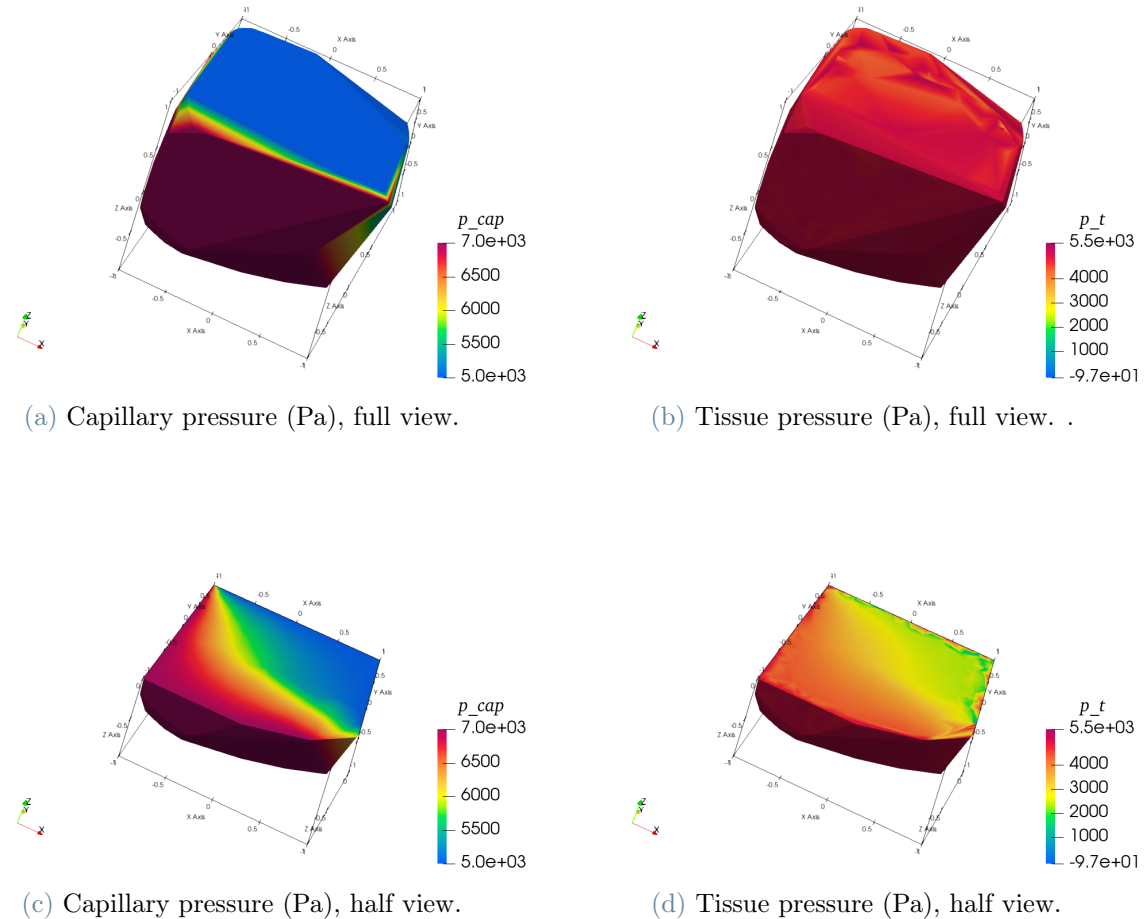


Figure 6.19: Results for the 3D-3D primal pressure coupled problem in a cubic domain extracted from the cancer geometry.

In this case, we had a portion of a realistic geometry but with dimensions comparable to the synthetic case. In this case, we can see that the pressure reconstruction in the capillary presents a coherent decrease going from the inlet to the outlet. Furthermore, the behavior obtained is more realistic than the previous case, since the network is more complex and the computed upscaled parameters presented slightly more differences than the synthetic case. Regarding the tissue, the behavior of the pressure is similar to the capillary one, with a lower magnitude because the permeability tensor associated with the tissue is smaller than the one for the capillary bed. Moreover, one can notice that there are some portions near the boundary where the pressure is negative. This may be due to a solver issue in correctly imposing the boundary conditions.

## 6.3. Entire Mouse Tumor Vasculature

### 6.3.1. Real-Case Cancer Geometry: Boundary Points

As the last test case of this project, we wanted to test our approach on the entire cancer mesh, described in 6.2.1. The aim was to reconstruct capillary and tissue pressure throughout the tumor domain. The principal challenge with regard to this problem was to obtain the boundary nodes. In fact, in the previous cases, we first consider a cubic geometry and then a cubic domain extracted from a complex geometry. For both of these cases the boundary points were found by geometric proximity to the planes that delimited the domains. In this case, we have a very complex geometry with indented sections and even cavities around the surface. To calculate the boundary points and the suitable boundary values, we followed the strategy described in [13]. Therefore, the hull was approximated using the Matlab function `alphashape`, which creates a bounding volume that envelopes a set of 3D points. The `alphaShape` object can be manipulated to tighten or loosen the fit around the points to create a nonconvex region by setting the alpha radius in a suitable way. Further details are listed in [16]. Moreover, after obtaining the `alphaShape` object, it is straightforward to address the boundary facets and identify the indexes of the boundary points. For what concerns our case, we had to find a balance between computing a complete convex hull, which unfortunately also finds some interior points due to the heterogeneity of the network, and a more flexible structure where we sacrifice some points but we create a feasible geometry. We met our expectations using `alpha_radius = 0.15`.

### 6.3.2. REV Division

The technique specified in the previous section was applied to the cancer geometry obtained by the REANIMATE project. After scaling the coordinates, to have a domain contained in the cubic region  $[-1, 1]^3$ . Moreover, as before, we had to post-processed the given radii in order to have a relation with the edges of the vascular network rather than with the bifurcation points. Figure 6.20 shows the final result of the boundary points procedure, and Table 6.5 lists the characteristics of the vascular network.

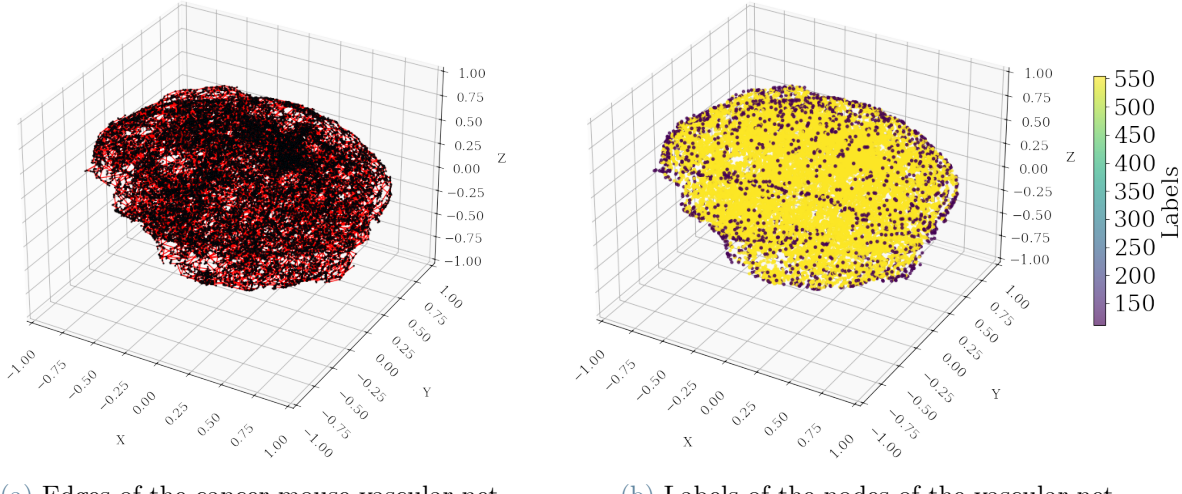


Figure 6.20: Visualization of the edges and labeled nodes of the comprehensive cancer vascular network.

No. of nodes	18093
No. of edges	23949
No. of boundary points	15897
No. of interior points	2196
Boundary points label	111
Interior points label	555

Table 6.5: Mesh specifics of the cancer vascular network

With respect to the REV division, this case requested further reasoning. In fact, the strategy to observe the average ratio described in Section 6.1.2, was no longer reliable for this case, due to the strong heterogeneity of the network and the different algorithms used for the search for the boundary points. Looking at the vascular network, it is evident that some parts are more dense and extensive than others, which seem to be thinner and smaller. For this reason, instead of partitioning the domain into equal parts, as we did for the previous cases, we chose "by hand" a suitable subdivision of the axis in order to have a coherent REV division of the domain. Therefore, we followed the following subdivisions:

- $X - axis$ : divided into 3 unequal parts namely we choose  $x = [-1, -0.4, 0.32, 1]$ ;
- $Y - axis$ : divided into 2 unequal parts namely we choose  $y = [-1, 0.2, 1]$ ;
- $Z - axis$ : divided into 3 unequal parts namely we choose  $z = [-1, -0.49, 0.23, 1]$ ;

The chosen number of REV is then 18, where each division has as sizes a combination of the aforementioned partitions. For example, REV 1 would be identified by  $x \in [-1, -0.4]$ ,  $y \in [-1, -0.2]$  and  $z \in [-1, -0.49]$ . The final REV division of the vascular net can be seen in 6.21

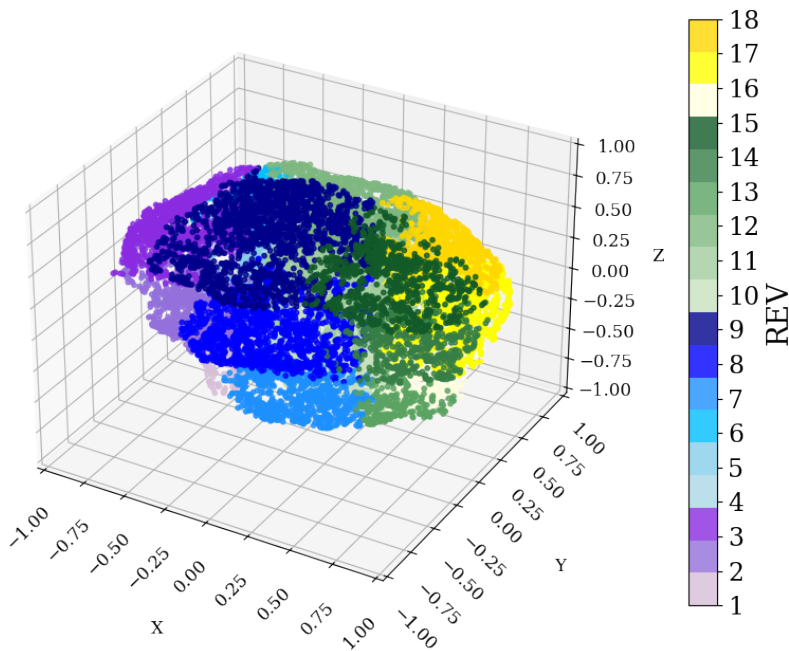
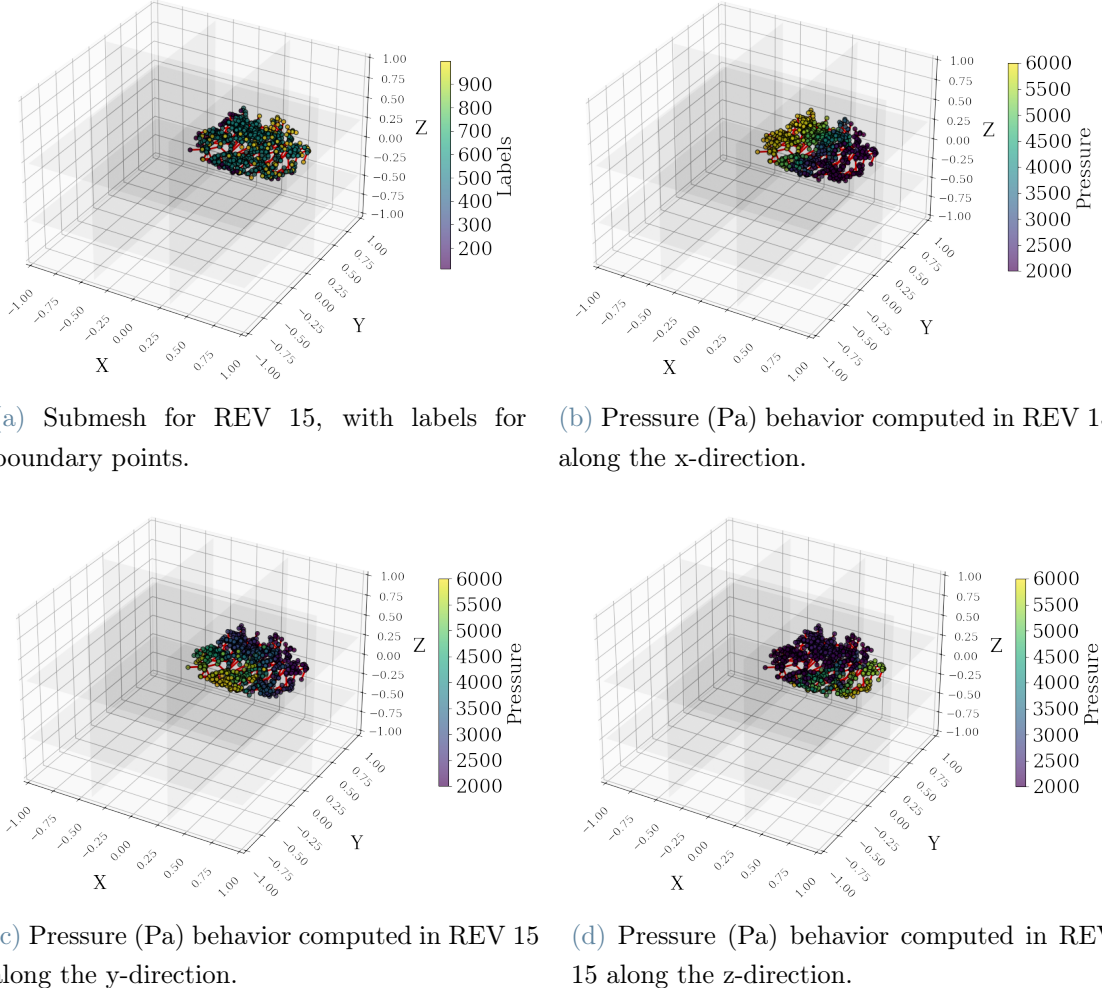


Figure 6.21: Segmentation of the tumor domain in 18 REVs.

### 6.3.3. Upscaled Parameters

Here we present the resulting parameters obtained from the upscaled approach. First, we present the pressure blood flow simulated in each REV in each direction. This is necessary for the computation of the component of the permeability tensor  $K^{up}$ . To have coherence with the parameters used in [13], we chose a negative larger drop than the previous cases, namely  $p_{inlet} = 6000$  Pa, and  $p_{outlet} = 2000$  Pa, for the selected faces for each direction. In Figure 6.22 the results for REV 15 are collected. As before, the behavior of the pressure is the one expected.



**Figure 6.22:** Submesh with labels and pressure approximation for directions  $[x, y, z]$  of REV 15 of the complete tumor geometry.

Finally, we present the computed values for the upscaled parameters, namely  $K^{up}$ ,  $\mu_{bl}^{up}$  and  $\gamma$ . Also in this case we propose a visualization by points instead of by region because of the strong heterogeneity of this domain. In Figure 6.23, the results are shown. Lastly, in Figure 6.24 the results for the average viscosity and the term of the Starling filtration law are shown.

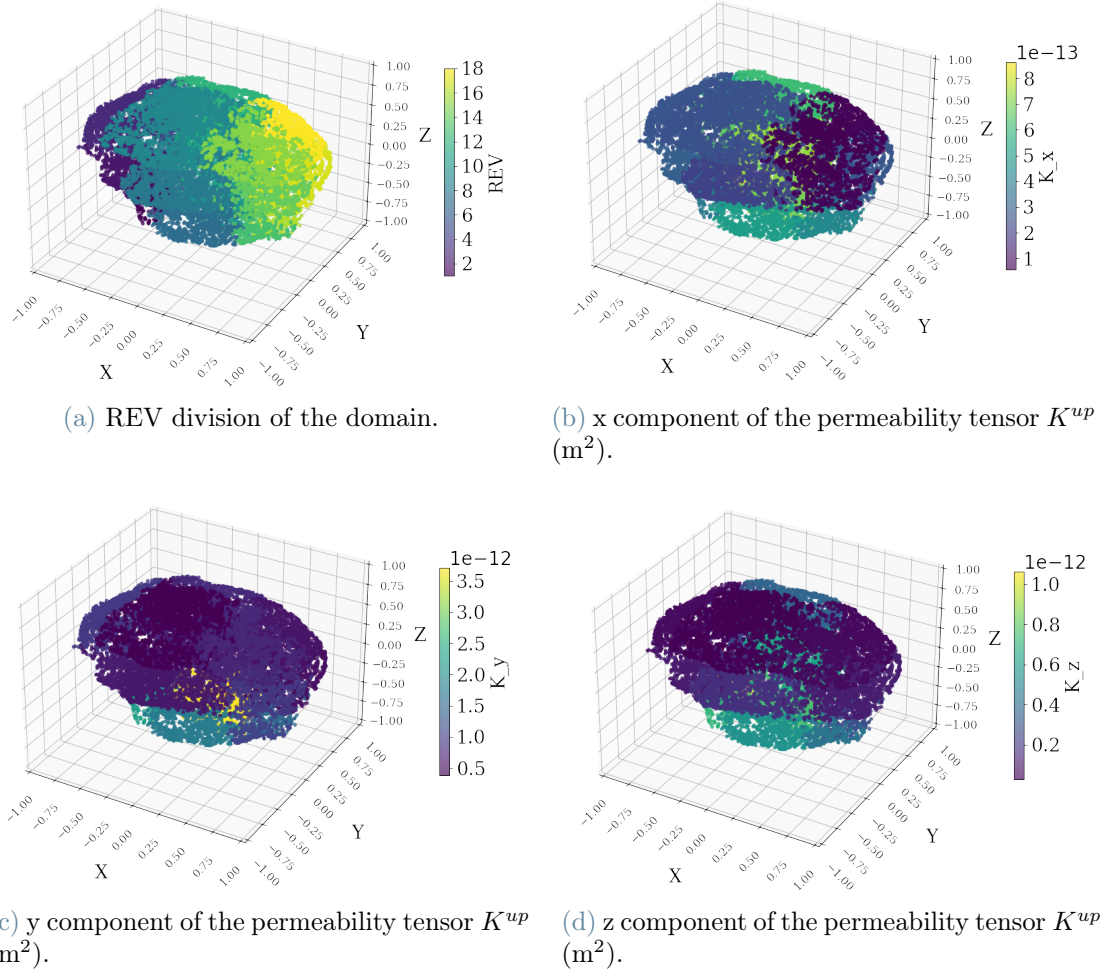


Figure 6.23: Components of the permeability tensor  $K^{up}$  calculated for each REV of the comprehensive tumor geometry.

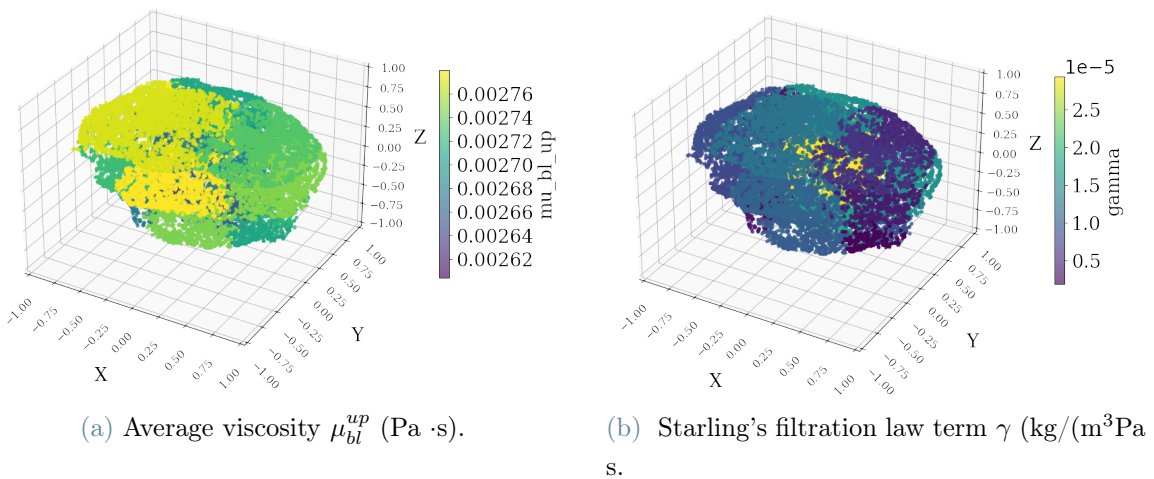


Figure 6.24: Values of  $\mu_b^{up}$  and  $\gamma$  for each REV of the comprehensive tumor geometry.

The orders of magnitude of these results are coherent with the ones of the test cases presented before. Moreover, we can notice more heterogeneity in this case since we divided the domain into more parts and the net is more complex than in the previous cases.

### 6.3.4. Primal Pressure Model

In this last section, we report the results obtained by testing our method with the cancer mouse mesh. Our approach can be useful for this type of problem since the tumor vasculature is usually very complex and is mostly made up of vessels with radii of the order of  $\mu$  m. Therefore, a homogenized approach can be used to reduce the computational cost and still obtain approximate but feasible results.

As in the previous case, the geometry is discretized using Delaunay triangulation, with *tetrahedron* element. The resulting mesh had 18093 nodes and 120078 cells, and is shown in Figure 6.25.

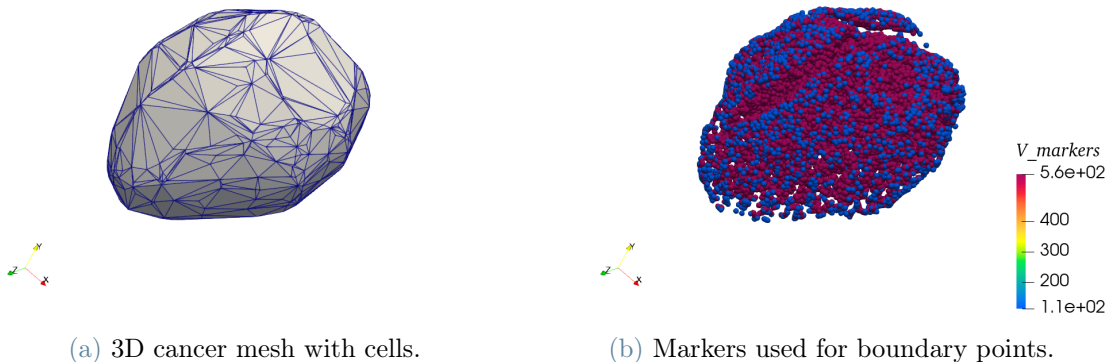


Figure 6.25: Plot of the mesh obtained from the comprehensive tumor geometry, with suitable markers to used to label the boundary points, necessary for the simulation of the pressure in the capillaries and the tissue of the homogenized model.

In this case, we had to consider a different type of boundary conditions. In fact, in this type of geometry, it is not possible to recognize specific faces for the inlet and outlet. To overcome this problem, we create an algorithm to assign feasible boundary conditions. At first, a desired number of inlet points is defined. Then we randomly extract one point from the list of boundary points and assign the Dirichlet boundary condition  $p_{inlet} = 6000$  Pa. After that, a sphere centered on the chosen point is defined, and the points belonging to the sphere and to the boundary points are identified. Finally, for point  $\mathbf{x}$ , the Dirichlet

boundary conditions are assigned with the following function:

$$P_{\text{IN}}(\mathbf{x}) = p_{\text{inlet}} \exp(-2\|\mathbf{x} - \mathbf{x}_C\|) \quad (6.2)$$

Here  $\mathbf{x}_C$  are the coordinates of the center. In this way, we obtain a spot with a radially decreasing pressure value, whose center is the maximum value. This process is repeated until the given number of inlet points is obtained.

In a similar way, the outlet points are found, and the Dirichlet boundary conditions and the Dirichlet boundary conditions for the outlet are imposed. In this case, the function used is increasing with distance, in order to have as the center of the sphere a minimum point. In fact, we used:

$$P_{\text{OUT}}(\mathbf{x}) = p_{\text{outlet}} \exp(2\|\mathbf{x} - \mathbf{x}_C\|) \quad (6.3)$$

where  $p_{\text{outlet}} = 2000$  Pa. The result of this process can be seen in Figure 6.26.

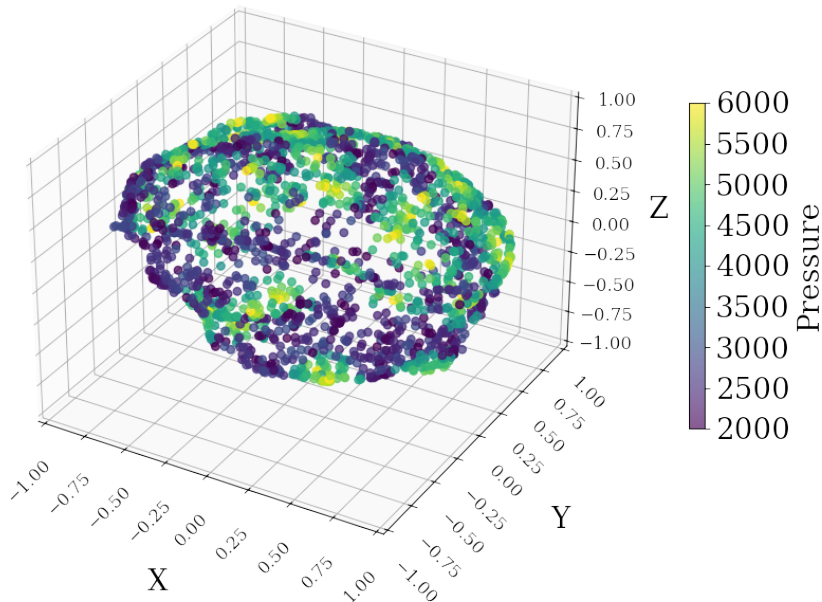


**Figure 6.26:** Pressure Boundary Conditions for the capillary model, specifically built for the comprehensive tumor geometry.

Lastly, we report the result obtained solving the 3D-3D primal pressure approach using the GMRES method with ILU preconditioning and this geometry. The parameters used in the simulations are reported in Table 6.3, with the values of the boundary conditions described as before. The method converged in 58 iterations. In Figure 6.27, the results

regarding the capillary pressure and tissue ones are shown.

We can notice that the boundary conditions imposed on the guarantees of the capillary model are assigned in such a way that the highest pressure points are not near the lowest, as shown in Figure 6.27a. In this way, the possibility of having an unfeasible flow is neglected. The reconstruction of the capillary pressure is coherent with what we expect, from the highest point on the boundary, the pressure is decreasing and diffusing on the inside of the domain, while from the lowest ones it is arising. Moreover, the behavior is no longer predictable or linear, as we can notice for the half view in 6.27c. In this case, the wider range of the upscaled parameters due to a very intricate vasculature allowed more regions to be more porous than others. In terms of tissue pressure, the overall values obtained are lower than those of the capillaries, consistent with the findings in other test cases. Moreover, the pressure behavior is consistent with that of the capillary bed. From the full and half view, Figure 6.27b,6.27d, can be seen that the high- and low-pressure spots can also be identified in the tissue, as a result of the coupling with the capillary model, since in this case, we used the robin boundary conditions instead of Dirichlet. However, some points with negative pressure can be identified, especially at the boundary. This is probably due to the fact that it was difficult to set a correct reference pressure for this case since it depends on several factors, for example, the surrounding cancer environment. For this reason, we set  $p_0 = 0$  Pa, taking into account the fact that negative pressure could arise in some spots. Despite that, the behavior is overall coherent even if a refinement of the value  $p_0$  could lead to more realistic results.

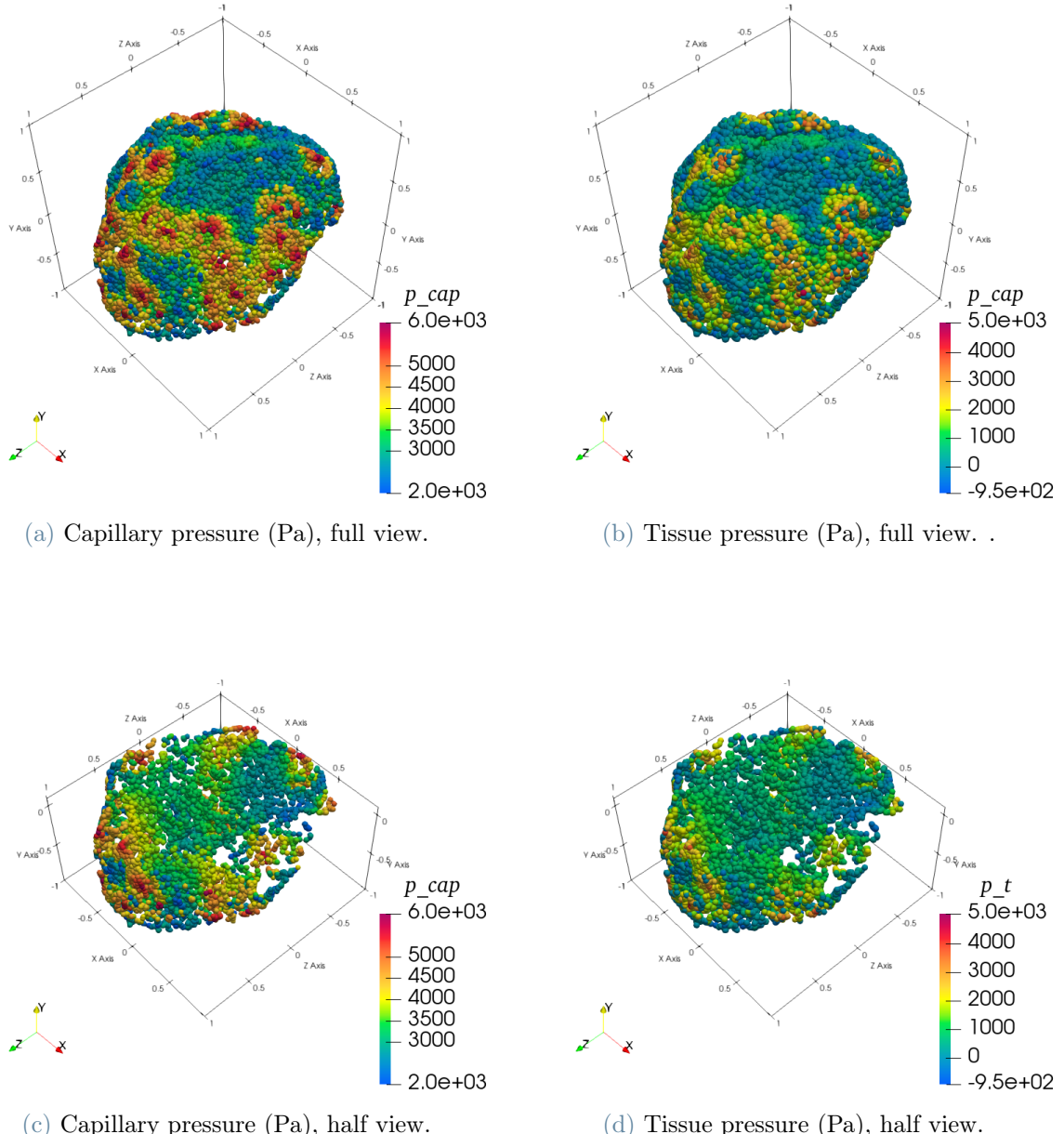


Figure 6.27: Results for the 3D-3D primal pressure coupled problem in the comprehensive tumor geometry.



# 7 | Conclusions

In the context of microvasculature, the study of new techniques to approximate blood flow in vessels with tiny diameters is widely spread, because of its applicability to various fields of medical research. For example, the study of how a specific drug behaves in cerebral tissue or the diffusion of oxygen in tumor vessels is just a few of the many areas of interest that involve the research of suitable microvasculature models.

The primary challenges stem from the complex and dense structure of the vascular networks, as well as their interaction with the tissue domain. In these cases, adopting a macroscale approach, namely considering the tissue as a 3D porous medium and a 3D vascular network, is not feasible, since an expensive 3D meshing of the vessels would be necessary. Some model reduction techniques are then necessary to simplify this problem.

To this end, the first step was to reduce the vascular problem from 3D to 1D, modeling the vessels using a graph representation using nodes and straight edges. Then, a homogenization approach is applied. A further simplification of the vascular network is obtained in this way by approximating the 1D representation using a 3D porous medium modeled with the Darcy law, with suitable parameters that synthesize the behavior of the vasculature, such as the permeability tensor, the average viscosity, and the coupling terms. To compute these parameters, an upscaling strategy is used, where the domain is divided into Representative Elementary Volume (REV), whose size has to be suitably chosen to have a coherent approximation of the vascular network. Then, in each REV, the upscaled parameters are computed to have a local representation of the vascular network. The result is a 3D-3D coupled model in both the full-pressure and the mixed formulation, where in the latter we recover the velocity from the Darcy law, embedded with suitable boundary conditions.

Then, to solve these problems, their numerical discretization is presented using the Finite Element Method (FEM), obtaining a 2x2 system of block matrices for the primal pressure model and a 4x4 for the mixed one. This choice is justified by the fact that we wanted

to develop a flexible and efficient tool to approximate the solution. For this reason, we implemented the code using `Python` language that had several packages that efficiently managed the assembly and block structure of the problem, like `fenics` and `cbc.block`, and the solution of a linear system, such as PETSC. The implementation involves a first part where a code is developed for the division of the domain in REV and the computation of the upscaled parameters and a second one where the block system is assembled and solved.

Finally, the developed solver is tested using three different configurations of microvasculature. The first test case involves a synthetic vascular mesh embedded in a cubic domain. The values of the upscaled parameters obtained are consistent with those presented in the literature. Moreover, reconstruction of the capillary and tissue pressure seems feasible for this type of domain considering the boundary conditions applied, even though further tests and refinements could enhance the tissue results. After that, we consider a more complex case where we tested our approach with the geometry of a mouse cancer, which is widely used in this field as a test case to have a better understanding of the applicability of these approximations in real-life scenarios. At first, it is considered a reduced geometry, extracting a cube from the given vascular structure. The results obtained in this case are in accordance with those of the previous test case, with a slightly more variability in the permeability tensor as a result of the intricate structure of the net. Moreover, the reconstruction of capillary and tissue pressure seems to represent a feasible behavior. Lastly, our approach is tested on the whole cancer geometry, where some homogenization techniques have already been tested. Nevertheless, we introduced anisotropic permeability tensors, that represent the perfusion property of the vascular network in a detailed way. Moreover, a deeper REV discretization was requested due to the wide heterogeneity of the capillary structure. Furthermore, specific realistic boundary conditions had to be thought of and developed. The results obtained regarding the pressure are promising and offer variable insides for future developments.

In summary, this study emphasizes the capability of the homogenization method to create a more straightforward model for simulating blood flow in microvasculature. This is achieved by utilizing an appropriate solver to partition the vascular network into representative elementary volumes (REVs) and solve the simplified system. In the future, there is significant potential for growth and improvement in this field. First of all, also introducing a hierarchy in the vascular architecture in this approach could be the key to obtaining more realistic results, as has been done in [28]. Thus, a distinct model could be created for the larger vasculature and integrated with the models for the tissue and capillaries. Furthermore, a deep study of the application of the mixed formulation to

more complex cases, such as mouse cancer geometry, can be conducted, which here it was not possible to perform due to the high computational cost of solving the linear system. Moreover, a further analysis on more suitable boundary conditions can be led, in order to obtain a realistic framework to represent real-life scenarios.



## Bibliography

- [1] G. Allaire. Homogenization and two-scale convergence. *Siam Journal on Mathematical Analysis*, 23:1482–1518, 1992. doi: 10.1137/0523084.
- [2] G. Allaire. A brief introduction to homogenization and miscellaneous applications\*. *ESAIM: Proceedings*, 37:1–49, 9 2012. URL <http://eudml.org/doc/251234>.
- [3] J. C. Arciero, P. Causin, and F. Malgaroli. Mathematical methods for modeling the microcirculation. *AIMS Biophysics*, 4(3):362–399, 2017. ISSN 2377-9098. doi: 10.3934/biophy.2017.3.362. URL <https://www.aimspress.com/article/doi/10.3934/biophy.2017.3.362>.
- [4] D. Boffi, F. Brezzi, and M. Fortin. *Mixed Finite Element Methods and Applications*. Springer Series in Computational Mathematics. Springer Berlin, Heidelberg, 1 edition, 2013. ISBN 978-3-642-36518-8. doi: 10.1007/978-3-642-36519-5. Copyright Information: Springer-Verlag Berlin Heidelberg 2013.
- [5] L. Cattaneo and P. Zunino. A computational model of drug delivery through microcirculation to compare different tumor treatments. *International Journal for Numerical Methods in Biomedical Engineering*, 30(11):1347–1371, Nov 2014. doi: 10.1002/cnm.2661.
- [6] A. d’Esposito, P. W. Sweeney, M. Ali, M. Saleh, R. Ramasawmy, T. A. Roberts, G. Agliardi, A. Desjardins, M. F. Lythgoe, R. B. Pedley, R. Shipley, and S. Walker-Samuel. Computational fluid dynamics with imaging of cleared tissue and of in vivo perfusion predicts drug uptake and treatment responses in tumours. *Nature Biomedical Engineering*, 2(10):773–787, 2018. ISSN 2157-846X. doi: 10.1038/s41551-018-0306-y. URL <https://doi.org/10.1038/s41551-018-0306-y>.
- [7] Y. Efendiev, T. Hou, and X. hui Wu. Convergence of a nonconforming multiscale finite element method. *SIAM J. Numer. Anal.*, 37:888–910, 2000. doi: 10.1137/S0036142997330329.
- [8] W. El-Bouri and S. Payne. Multi-scale homogenization of blood flow in 3-dimensional

- human cerebral microvascular networks. *J Theor Biol*, 380:40–47, Sep 7 2015. doi: 10.1016/j.jtbi.2015.05.011. URL <https://doi.org/10.1016/j.jtbi.2015.05.011>.
- [9] A. Ern and J.-L. Guermond. *Theory and Practice of Finite Elements*. Applied Mathematical Sciences. Springer New York, 2004. ISBN 978-0-387-20574-8. doi: 10.1007/978-1-4757-4355-5. URL <https://doi.org/10.1007/978-1-4757-4355-5>.
- [10] R. Fåhræus and T. Lindqvist. The viscosity of the blood in narrow capillary tubes. *American Journal of Physiology-Legacy Content*, 96(3):562–568, 1931. doi: 10.1152/ajplegacy.1931.96.3.562. URL <https://doi.org/10.1152/ajplegacy.1931.96.3.562>.
- [11] G. Hartung, C. Vesel, R. Morley, A. Alaraj, J. Sled, D. Kleinfeld, and A. Linniger. Simulations of blood as a suspension predicts a depth dependent hematocrit in the circulation throughout the cerebral cortex. *PLOS Computational Biology*, 14(11):1–25, 11 2018. doi: 10.1371/journal.pcbi.1006549. URL <https://doi.org/10.1371/journal.pcbi.1006549>.
- [12] U. Hornung, editor. *Homogenization and Porous Media*. Interdisciplinary Applied Mathematics. Springer New York, NY, 1 edition, 1997. ISBN 978-0-387-94786-0. doi: 10.1007/978-1-4612-1920-0. URL <https://doi.org/10.1007/978-1-4612-1920-0>. Copyright Springer Science+Business Media New York 1997.
- [13] J. Kremheller, S. Brandstaeter, B. A. Schrefler, and W. A. Wall. Validation and parameter optimization of a hybrid embedded/homogenized solid tumor perfusion model. *International Journal for Numerical Methods in Biomedical Engineering*, 37(11):e3508, 2021. doi: 10.1002/cnm.3508. URL <https://doi.org/10.1002/cnm.3508>. Citations: 1.
- [14] F. Laurino and P. Zunino. Derivation and analysis of coupled pdes on manifolds with high dimensionality gap arising from topological model reduction. *ESAIM: Mathematical Modelling and Numerical Analysis*, 53, 06 2019. doi: 10.1051/m2an/2019042.
- [15] A. Linniger, G. Hartung, S. Badr, and R. Morley. Mathematical synthesis of the cortical circulation for the whole mouse brain-part i. theory and image integration. *Computers in Biology and Medicine*, 110:265–275, Jul 2019. doi: 10.1016/j.combiomed.2019.05.004.
- [16] MathWorks. Documentation of MATLAB’s alphaShape function. Online documentation, Accessed 2024. URL <https://it.mathworks.com/help/matlab/ref/alphashape.html>.

- [17] C. Michel, T. Woodcock, and F. Curry. Understanding and extending the starling principle. *Acta Anaesthesiol Scand*, 64(8):1032–1037, Sep 2020. doi: 10.1111/aas.13603. URL <https://doi.org/10.1111/aas.13603>.
- [18] C. Michler, A. Cookson, R. Chabiniok, E. Hyde, J. Lee, M. Sinclair, T. Sochi, A. Goyal, G. Vigueras, D. Nordsletten, and N. Smith. A computationally efficient framework for the simulation of cardiac perfusion using a multi-compartment darcy porous-media flow model. *International Journal for Numerical Methods in Biomedical Engineering*, 29, 2013. doi: 10.1002/cnm.2520.
- [19] L. Possenti, A. Cicchetti, R. Rosati, D. Cerroni, M. Costantino, T. Rancati, and P. Zunino. A mesoscale computational model for microvascular oxygen transfer. *Ann Biomed Eng*, 49(12):3356–3373, Dec 2021. doi: 10.1007/s10439-021-02807-x. URL <https://doi.org/10.1007/s10439-021-02807-x>.
- [20] C. Pozrikidis. Numerical simulation of blood flow through microvascular capillary networks. *Bulletin of Mathematical Biology*, 71:1520–1541, 2009. doi: 10.1007/s11538-009-9412-z.
- [21] A. Pries and T. Secomb. *Blood Flow in Microvascular Networks*. 2011. doi: 10.1016/B978-0-12-374530-9.00001-2. URL [https://consensus.app/papers/blood-flow-microvascular-networks-pries/13c1135ddec75eaeaf6d55a28f7a7928/?utm\\_source=chatgpt](https://consensus.app/papers/blood-flow-microvascular-networks-pries/13c1135ddec75eaeaf6d55a28f7a7928/?utm_source=chatgpt).
- [22] A. R. Pries, T. W. Secomb, and P. Gaehtgens. Biophysical aspects of blood flow in the microvasculature. *Cardiovascular research*, 32(4):654–667, Oct 1996.
- [23] A. Quarteroni. *Numerical Models for Differential Problems*, volume 16 of *MS&A*. Third edition, 2017.
- [24] J. Reichold, M. Stampanoni, A. L. Keller, A. Buck, P. Jenny, and B. Weber. Vascular graph model to simulate the cerebral blood flow in realistic vascular networks. *Journal of Cerebral Blood Flow & Metabolism*, 29(8):1429–1443, 2009. doi: 10.1038/jcbfm.2009.58.
- [25] SciPy Developers. Documentation of SciPy’s Delaunay function. Online documentation, Accessed 2024. URL <https://docs.scipy.org/doc/scipy/reference/generated/scipy.spatial.Delaunay.html>.
- [26] T. Secomb, R. Hsu, M. Dewhirst, B. Klitzman, and J. Gross. Analysis of oxygen transport to tumor tissue by microvascular networks. *Int J Radiat Oncol Biol Phys*, 25(3):481–489, 1993. doi: 10.1016/0360-3016(93)90070-c.

- [27] P. W. Sweeney, A. d’Esposito, S. Walker-Samuel, and R. J. Shipley. Modelling the transport of fluid through heterogeneous, whole tumours in silico. *PLoS Comput Biol*, 15(6):e1006751, 2019. doi: 10.1371/journal.pcbi.1006751.
- [28] E. Vidotto, T. Koch, T. Köppl, R. Helmig, and B. Wohlmuth. Hybrid models for simulating blood flow in microvascular networks. *Multiscale Modeling & Simulation*, 17:1076–1102, 09 2019. doi: 10.1137/18M1228712.

# List of Figures

5.1	Example of a synthetic 1D vascular net. . . . .	36
5.2	Edges that connect vertices belonging to different REVs. . . . .	38
5.3	Shorter caption . . . . .	39
5.4	Example of a submesh of the original vascular network, obtained with the division process. . . . .	41
6.1	Example of a point cloud to give as input to the 3D Voronoi tessellations algorithm. . . . .	48
6.2	Examples of the creation process of a synthetic vascular network. . . . .	49
6.3	Final vascular net obtained after the application of Dijkstra algorithm. . . . .	50
6.4	Visualization of the edges and labeled nodes of the synthetic vascular network. . . . .	51
6.5	Segmentation of a cubic domain with an embedded synthetic vascular net in 8 REVs. . . . .	53
6.6	Submesh with labels and pressure approximation for directions $[x, y, z]$ , of REV 6 of the cubic synthetic domain. . . . .	54
6.7	Components of the permeability tensor $K^{up}$ for each REV of the cubic synthetic domain. . . . .	55
6.8	Values of $\mu_{bl}^{up}$ and $\gamma$ computed for each REV of the cubic synthetic domain. . . . .	56
6.9	Plot of the mesh obtained from the cubic synthetic domain, with suitable markers used to label the boundary points and the REV points, necessary for the simulation of the pressure in the capillary and tissue of the homogenized model. . . . .	57
6.10	Results for the 3D-3D primal pressure coupled problem in a cubic synthetic domain. . . . .	58
6.11	Results for the 3D-3D mixed coupled problem in a cubic synthetic domain, where the velocity and pressure of the blood flow have been reconstructed for the capillary bed and tissue. . . . .	60
6.12	Different Snapshots of the mouse cancer geometry . . . . .	61
6.13	Visualization of the edges and labeled nodes of the cubic portion extracted for the cancer vascular network. . . . .	62

6.14 Segmentation of the cubic domain extracted from the cancer geometry in 8 REVs. . . . .	63
6.15 Submesh with labels and pressure approximation for directions $[x, y, z]$ , of REV 1 of the cubic domain extracted from the cancer geometry. . . . .	64
6.16 Components of the permeability tensor $K^{up}$ for each REV of the cubic domain extracted from the cancer geometry. . . . .	65
6.17 Values of $\mu_{bl}^{up}$ and $\gamma$ for each REV of the cubic domain extracted from the cancer geometry. . . . .	66
6.18 Plot of the mesh obtained from the cubic geometry extracted from the cancer domain, with suitable markers used to label the boundary points and the REV points, necessary for the simulation of the pressure in the capillary and tissue of the homogenized model. . . . .	67
6.19 Results for the 3D-3D primal pressure coupled problem in a cubic domain extracted from the cancer geometry. . . . .	68
6.20 Visualization of the edges and labeled nodes of the comprehensive cancer vascular network. . . . .	70
6.21 Segmentation of the tumor domain in 18 REVs. . . . .	71
6.22 Submesh with labels and pressure approximation for directions $[x, y, z]$ of REV 15 of the complete tumor geometry. . . . .	72
6.23 Components of the permeability tensor $K^{up}$ calculated for each REV of the comprehensive tumor geometry. . . . .	73
6.24 Values of $\mu_{bl}^{up}$ and $\gamma$ for each REV of the comprehensive tumor geometry. .	73
6.25 Plot of the mesh obtained from the comprehensive tumor geometry, with suitable markers to used to label the boundary points, necessary for the simulation of the pressure in the capillaries and the tissue of the homogenized model. . . . .	74
6.26 Pressure Boundary Conditions for the capillary model, specifically built for the comprehensive tumor geometry. . . . .	75
6.27 Results for the 3D-3D primal pressure coupled problem in the comprehensive tumor geometry. . . . .	77

# List of Tables

3.1	Parameters of the Homogenized model . . . . .	14
6.1	Mesh specifics of synthetic vascular net . . . . .	50
6.2	Values of $R_{avg}$ computed with different number of REVs . . . . .	52
6.3	Values of the parameters of the Homogenized model . . . . .	56
6.4	Mesh specifics of the cubic domain of the cancer vascular net . . . . .	62
6.5	Mesh specifics of the cancer vascular network . . . . .	70

